Concrete Strength Required to Open to Traffic

Minnesota Department of Transportation

RESEARCH SERVICES & LIBRARY

Office of Transportation System Management

Lev Khazanovich, Principal Investigator
Department of Civil, Environmental, and Geo- Engineering
University of Minnesota

January 2016

Research Project
Final Report 2016-01

To request this document in an alternative format call 651-366-4718 or 1-800-657-3774 (Greater Minnesota) or email your request to ADArequest.dot@state.mn.us. Please request at least one week in advance.

Technical Report Documentation Page

1. Report No.	2.	3. Recipients Accession No.	
MN/RC 2016-01			
4. Title and Subtitle Concrete Strength Required to Open to Traffic		5. Report Date January 2016 6.	
7. Author(s) Katelyn Freeseman, Kyle Hoegh, Lev Khazanovich		8. Performing Organization Report No.	
9. Performing Organization Name and Address Department of Civil, Environmental, and Geo- Engineering University of Minnesota 500 Pillsbury Drive SE Minneapolis, MN 55455		10. Project/Task/Work Unit No. CTS # 2014014 11. Contract (C) or Grant (G) No. (c) 99008 (wo) 105	
12. Sponsoring Organization Name and Address Minnesota Department of Transportation Research Services & Library 395 John Ireland Boulevard, MS 330 St. Paul, Minnesota 55155-1899		13. Type of Report and Period Covered Final Report 14. Sponsoring Agency Code	
15. Supplementary Notes http://www.lrrb.org/pdf/201601.pdf			

16. Abstract (Limit: 250 words)

The current empirical methods for determining traffic-opening criteria can be overly conservative causing unnecessary construction delays and user costs. The research described here recommends innovative mechanistic-based procedures for monitoring concrete early age development and evaluating the effect of early traffic opening on long-term damage accumulation. The procedure utilizes recent developments in nondestructive testing to optimize traffic opening timing without jeopardizing pavement longevity. These tasks were achieved via extensive field and laboratory experiments allowing for the analysis of variables such as curing condition and loading type with respect to the effect of early loading of concrete. The results of these efforts culminated in the development of a program that analyzes the effect of design and opening time decisions on pavement damage. The deliverable can be utilized by transportation agencies to make more informed decisions.

17. Document Analysis/Descriptors	18. Availability Statement		
Pavement design, Concrete Pavements, Paving, Concrete strength requirement, Early age concrete, Road opening timing	No restrictions. Document available from: National Technical Information Services, Alexandria, Virginia 22312		
19. Security Class (this report) Unclassified	20. Security Class (this page) Unclassified	21. No. of Pages 95	22. Price

Concrete Strength Required to Open to Traffic

Final Report

Prepared by:

Katelyn Freeseman
Kyle Hoegh
Lev Khazanovich
Department of Civil, Environmental, and Geo- Engineering
University of Minnesota

January 2016

Published by:

Minnesota Department of Transportation
Research Services & Library
395 John Ireland Boulevard, MS 330
St. Paul, Minnesota 55155-1899

Acknowledgments

The authors appreciate the participation of the members of the project technical advisory panel:

- Tom Burnham, MnDOT Road Research
- Maria Masten, MnDOT Concrete office
- Gordon Bruhn, MnDOT Concrete office
- Robert Golish, MnDOT Concrete office
- Matt Zeller, Concrete Pavement Association of Minnesota and
- Dan Warzala, MnDOT Research Services

In particular, the authors thank the project technical liaison, Bernard Izevbekhai of the MnDOT Office of Materials and Road Research, for his support, insight, and contributions to the project research through its many stages of development.

Table of Contents

Chapter 1: Introduction 1

Chapter 2: Literature Review 3

2.1 Structural Modeling 3

2.2 Field and Laboratory Testing 10

2.2.1 Maturity Method 10

2.3 Active Nondestructive Testing Methods 16

2.3.1 Ground Penetrating Radar (GPR) 16

2.3.2 Electromechanical Impedance 18

2.3.3 Conventional impact echo (IE) 18

2.3.4 Spectral Analysis of Surface Waves (SASW) 20

2.3.5 Ultrasonic Pulse Velocity 21

2.3.6 Ultrasonic Wave Reflection 23

2.3.7 Ultrasonic Linear Array 25

Chapter 3: Laboratory Testing 30

3.1 General Lab Procedures 30

3.1.1 Lab Processes 30

3.2 Round 1 Testing- Air Cured Samples 31

3.2.1 Results 32

3.3 Round 2 Testing – Water Cured Samples 37

3.3.1 Testing Outline 37

3.3.2 Results 38

3.4 Round 3 Testing – Water Cured Samples (Repeated) 41

3.4.1 Testing Outline 41

3.4.2 Results 42

3.5 Round 4 Testing – Curing Compound Samples 45

3.5.1 Testing Outline 45

3.5.2 Results 45

3.6 Conclusions 49

Chapter 4: Field testing 51

4.1 October 2013 Testing 51

4.1.1 October 10, 2013 51

4.1.2 October 17, 2013 52

4.2 July 2014 Testing 55

4.2.1 July 18, 2014 55

4.3 Conclusions 57

Chapter 5: Recommendations for Traffic Opening 58

5.1 Early Age Fatigue Damage Analysis Procedure 58

5.1.1 Overview of the MEPDG Fatigue Analysis 58

5.1.2 Early PCC Age Fatigue Analysis 62

5.2 Early Traffic Opening Analysis Procedure 67

5.3 Rudimentary Software 67

5.4 Summary 72

Chapter 6: Conclusions 73

References 74

Appendix A: Development of Improved Velocity Calibration Technique

List of Figures

Figure 1: ISLAB2000 model for critical load position for the left critical dowel. 3
Figure 2: Modeling of PCC-dowel interaction. 4
Figure 3: 2D finite element mesh of dowel/PCC interaction – fragment around dowel. 4
Figure 4: Typical contours of vertical displacements of concrete around a dowel bar (deformation scale factor is equal to 1,000,000. 5
Figure 5: Exposed dowel test specimen. 6
Figure 6: Two samples of the same concrete mix cured at different temperatures will reach the same strength level at the same maturity level (from Nelson 2003). 11
Figure 7: Curve of temperature versus time in the cement hydration cycle (from CP Tech Center 2007). 11
Figure 8: Relation between maturity, time, and temperature (from Olek et al 2003). 12
Figure 9: Sample maturity curve (from Nelson 2003). 13
Figure 10: Flexural strength vs. maturity (Rohne and Izevbekhai 2009). 14
Figure 11: Compressive strength vs. maturity (Rohne and Izevbekhai 2009). 15
Figure 12: Flexural strength vs. maturity (Wilde 2013). 15
Figure 13: Ground coupled GPR and example output at a transverse joint. Downward hoop signals indicate dowel bars or reinforcement. 17
Figure 14: Air coupled step-frequency GPR mounted on a van for high speed measurements. .. 17
Figure 15: Schematic illustration of the IE test (Scott et al 2003). 18
Figure 16: Impact echo setup with a steel ball mounted on a steel spring rod (Carino, 2001). 20
Figure 17: Schematic of the SASW (Gucunski, Soil Dynamics, 1992). 20
Figure 18: Various sending and receiving positions for UPV testing (Adapted from International Atomic Energy Agency, 2002). 21
Figure 19: Surface transmission pulse velocity (Graveen 2001). 22
Figure 20: UK1401 ultrasonic pulse velocity device (Khazanovich et al., 2005). 22
Figure 21: Reflection coefficient versus time (Chung et al 2010). 25
Figure 22: Transducer array technology for biomedical use adapted from (a) VonRamm et al., 1976, and (b) Minalga et al., 2012. 26
Figure 23: A1220 ultrasonic pulse-echo device 26
Figure 24: MIRA ultrasonic linear array device with a handle designed at the University of Minnesota for more productive measurements on pavement systems 27
Figure 25: Example impulse time history from a transducer pair, Ψ_4, 9 (t) from emitting channel 4 to receiving channel 9 (200 mm spacing) 28
Figure 26: Schematic of direct and reflection arrivals. 28
Figure 27: Ultrasonic Array measured shear wave velocities for concrete beams vs. slabs at various concrete ages. 29
Figure 28: Flexural Strength versus first day of load application. 33
Figure 29: Percent decrease in flexural strength versus first day of loading. 33
Figure 30: Percentage decrease in strength versus maturity. 34
Figure 31: Percentage decrease in strength versus velocity 34
Figure 32: Velocity variation from beam to beam at various ages. 35
Figure 33: Maturity versus time. 36
Figure 34: Velocity versus maturity. 36
Figure 35: Maturity versus velocity at days 1, 2, 3, 7, and 28 from the first round of testing. 37

Figure 36: Flexural Strength versus first day of load application. 39
Figure 37: Shear wave velocity versus Flexural Strength. 39
Figure 38: Shear wave velocity and flexural break strength over time. 40
Figure 39: Velocity variation from beam to beam at various ages. 41
Figure 40: Break strength at day of first loading. 43
Figure 41: Shear wave velocity versus Flexural Strength. 43
Figure 42: Shear wave velocity and flexural break strength over time. 44
Figure 43: Velocity variation from beam to beam at various ages. 44
Figure 44: Flexural Strength versus day of first loading. 46
Figure 45: Velocity variation for all beams at various ages. 46
Figure 46 Normalized shear wave velocity over time for control and loaded beams. 47
Figure 47: Shear wave velocity versus ultimate flexural strength. 48
Figure 48: P-wave velocity variation for various ages. 49
Figure 49: Ultimate strength vs. day of first loading for all four rounds of testing. 50
Figure 50: Shear Wave Velocity versus stationing for various days after paving and locations within the same project. 53
Figure 51: Velocity versus days after paving. 53
Figure 52: Direct velocity versus calibration velocity. 54
Figure 53: Velocities versus stationing using the new velocity method. 55
Figure 54: Velocity gain versus days after paving 56
Figure 55: Example of day 2 and 3 velocities versus the day 6 average values. 57
Figure 56: Components of the stress causing thermal gradient 61
Figure 57: Critical load and stress locations for bottom-up cracking (at left) and top-down cracking (at right) (from NCHRP 2003) 62
Figure 58: Normalized concrete elastic modulus at early age vs. time in days. 64
Figure 59: Normalized concrete flexural strength at early age vs. time in days. 65
Figure 60: Opening screen of program. 68
Figure 61: Program appearance after hitting the “Edit PCC Properties” button 69
Figure 62: Program screen for daily traffic in year 1 inputs. 70
Figure 63: Program screen for daily traffic in month 1 inputs. 70
Figure 64: Program results for trial analysis. 71
Figure 65: Program results for varied input analysis. 72

List of Tables

Table 1: Opening strengths and other data for fast-track paving projects (Roesler et al., 2000). 7
Table 2: Recommended flexural strength (psi) for opening (Roesler et al., 2000). 8
Table 3: State highway agency specifications for 6 to 8 hour opening (Van Dam et al., 2005). 9
Table 4: State highway agency specifications for 20 to 24 hour opening (Van Dam et al., 2005). 10
Table 5: Parameters of relevant relationships (Voigt et al 2003). 24
Table 6: Summary of laboratory trials. 30
Table 7: Concrete Mix Design 31
Table 8: Round 1 loading summary. 32
Table 9: Round 2 loading summary. 38

Table 10: Round 3 loading summary. 42
Table 11: Round 4 loading summary. 45
Table 12: October Field Testing Mix Design 51
Table 13: Pavement Stationing and Age Information 52
Table 14: July Field Testing Pavement Information 55
Table 15: July Field Testing Mix Design 56

Executive Summary

Current methods to estimate when to open pavements to traffic are often overly conservative, which causes unnecessary construction delays and user costs. The primary issue with the current methods is that they are generally experience-based and inflexible:

- They do not account for specific site conditions such as unique traffic timing and capacity related needs.
- Wait periods after concrete placement are required in terms of a) time after placement or b) the achievement of certain levels of compressive and/or flexural strength. Required values in either case are not typically supported with data.
- The effect of early traffic-related loads on long-term pavement behavior is not quantified.

Because the current opening criteria do not provide the agency any flexibility to develop alternative traffic opening solutions, traffic opening is ignored by the agency when investigating the cost savings and performance of a project over its life cycle.

In this study, the effect of early opening on pavement damage was reexamined through a laboratory study and through analytical modeling of pavement behavior at early ages (28 days after placement or less). This resulted in a mechanistic procedure for evaluating the effect of early traffic opening on the long-term performance of the pavement. The developed procedure accounts for critical factors such as climate, traffic level, and pavement design characteristics. The procedure to estimate performance, when considered alongside the laboratory work, has a number of advantages over the conventional, experience-based methods:

- The procedure is implemented in a user-friendly computer program that aids in estimating optimal timing of traffic opening given basic pavement information (including as-built properties from non-destructive testing measurements).
- The laboratory trials provided extensive early-age concrete strength data that led to the formulation of multiple concrete strength curves that were incorporated into the developed program. Thus, experienced-based “guess work” has been replaced by repeatable, reproducible observations from the lab.
- The output of the program allows the road owner to do a cost/benefit analysis of the opening timing based on the specific site and traffic characteristics.

The method developed in this research provides an alternative to the rigidity of conventional methods for time-to-opening. The report provides example analyses to demonstrate the usefulness of the program. Overall, the program provides the agency with the ability to adapt to changing environmental conditions and implement innovative traffic-opening strategies. As a result, transportation agencies can make important opening to traffic decisions based on anticipated site conditions rather than invariable, experience-based rules.

Chapter 1: Introduction

The current criteria for minimum concrete strength before opening to traffic are based on purely empirical methods. These criteria require wait periods after concrete placement or achievement of certain levels of compressive and/or flexural strength after the time of placement. Although the strength-based criteria are the more objective of the two current procedures, the current requirement of 3,000 psi compressive strength may be overly conservative in certain cases. This project deals with the development of a process of determining the optimal strength of concrete pavement opening to traffic based on nondestructive testing and rational acceptance criteria. The proposed method will incorporate maturity monitoring procedures discussed by Izevbekhai and Rohne (2009). In addition, highly accurate measurements of shear wave velocity that can be conducted on both beams and in-situ pavements will be evaluated. Using the above-described methods in laboratory and field settings, the research will result in a procedure, which can be implemented by MnDOT and local transportation agencies for optimal timing of traffic opening.

To achieve these research goals, the following tasks are presented:

Task 1: Literature Review

A comprehensive literature review of the current mechanistic models for opening to traffic and assessment of damage from early opening was conducted. A literature of nondestructive evaluation of concrete properties and their applications for concrete pavement assessments, such as maturity measurements, chain dragging, ground penetrating radar, ultrasound tomography, etc., is also included.

Task 2: Laboratory Testing

Several rounds of laboratory testing were completed utilizing MTS testing equipment at the University of Minnesota to perform 4 point bending flexural strength tests. Originally, compressive strength and flexural strength were considered, but the final three rounds of testing only incorporated flexural strength due to the inconclusive compressive results that were seen in the first round. Flexural strength, maturity measurements, and ultrasound tomography shear wave velocity measurements were conducted throughout the curing and testing process. This enabled correlation between concrete strength developments with maturity as well as concrete elastic properties computed from the shear wave velocity measurements. The ultrasound tomography also monitored the progression of damage due to fatigue loading. This provided the opportunity to quantify damage from simulated axle loading applied at various concrete early age and strength development levels.

Task 3: Field Testing

Several test slabs with the same mix design were identified in new construction projects. Ultrasound tomography shear wave velocity measurements were conducted throughout the curing process at early concrete ages. This provided side by side comparison of shear wave velocity results in the laboratory and the field.

Task 4: Recommendations for Traffic Opening Timing

The results of the laboratory and field tests were used to develop a procedure for determining an appropriate timing of subjecting the pavement to wheel loading without causing significant damage. The deliverable for this task is a software program developed to be used by MnDOT research staff. Different criteria is applied for different loading types and roadway design type. This procedure is based upon the maturity and/or shear wave velocity measurements in conjunction with concrete strength and elastic modulus curves, representing in-situ real-time pavement properties.

Chapter 2: Literature Review

In Task 1, a comprehensive literature review of the current mechanistic models and structural considerations for assessment of damage from early opening of concrete pavements to traffic was synthesized. Additional literature review was conducted on traditional and state-of-the-art nondestructive tools that can be used for evaluation of concrete properties and their applications for early age concrete pavement assessments.

2.1 Structural Modeling

McCullough and Rasmussen conducted research in the mid-90's regarding fast track paving and early opening to traffic. The focus of their research was on the development of a software package, which was eventually named High Performance Paving (HIPERPAV) and High Performance Bonded Concrete Overlays (HIPERBOND). This software is applicable to JPCP and bonded overlays, and aims to predict pavement strength as a function of heat development during the hydration process. The need for this software arose from previous models lacking early age effects of heat on concrete hydration, convection, irradiation, and solar radiation absorption. While the models were developed to improve on past model deficiencies, there were shortcomings. Pavement moisture modeling was not included, nor was the ability to characterize curing methods. Verification of the thermal coefficient and creep relaxation models used would also improve HIPERPAV and HIPERBOND (McCullough and Rasmussen 1999).

Crovetti and Khazanovich (2005) used ISLAB2000 and ABAQUS to analyze the effect of concrete slab properties at early age on stresses in concrete pavements. ISLAB2000 was used to model global pavement behavior due to heavy axle loading (see Figure 1).

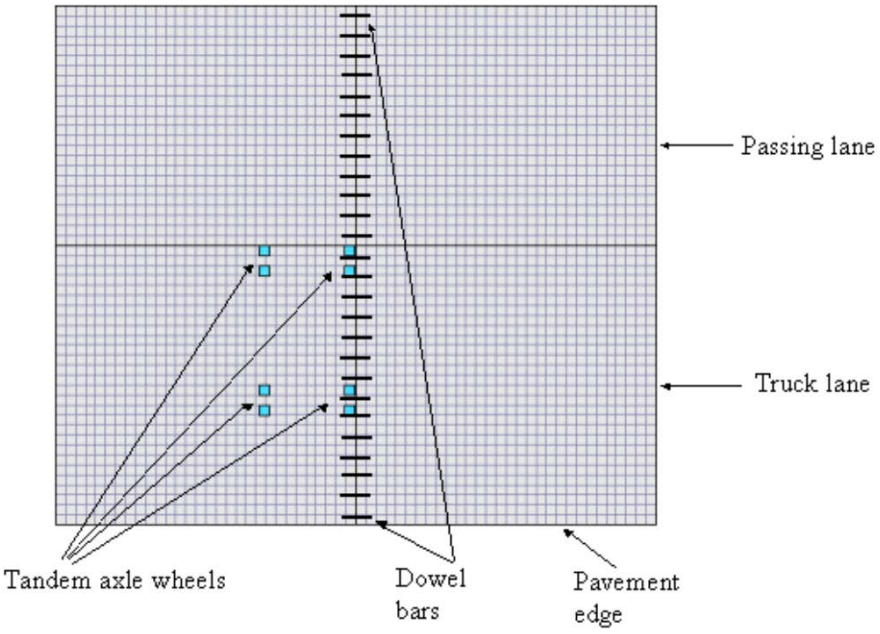

Figure 1: ISLAB2000 model for critical load position for the left critical dowel.

The general purpose finite element program, ABAQUS, was used for detailed modeling of local stress distribution around dowels for various early age concrete characteristics. The general layout of the model is shown in
Figure 2. It can be observed that the critical cross section of the dowel was used for analysis. The mesh used for evaluation of the stress distribution around dowels is shown in Figure 3, while the typical displacement contours are given in Figure 4.

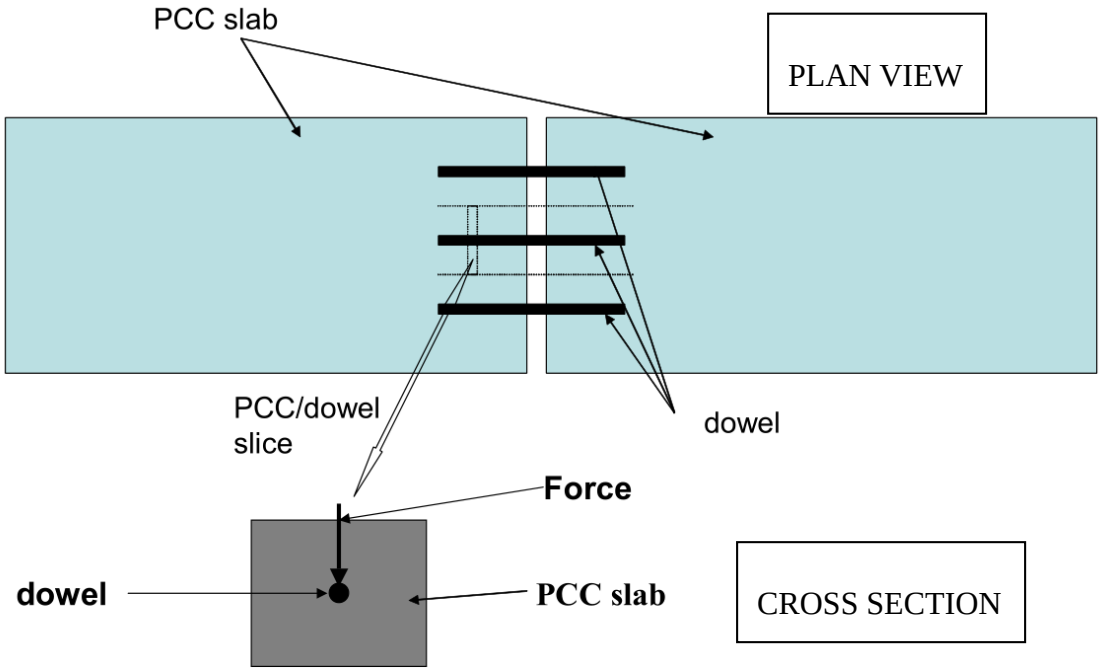

Figure 2: Modeling of PCC-dowel interaction.

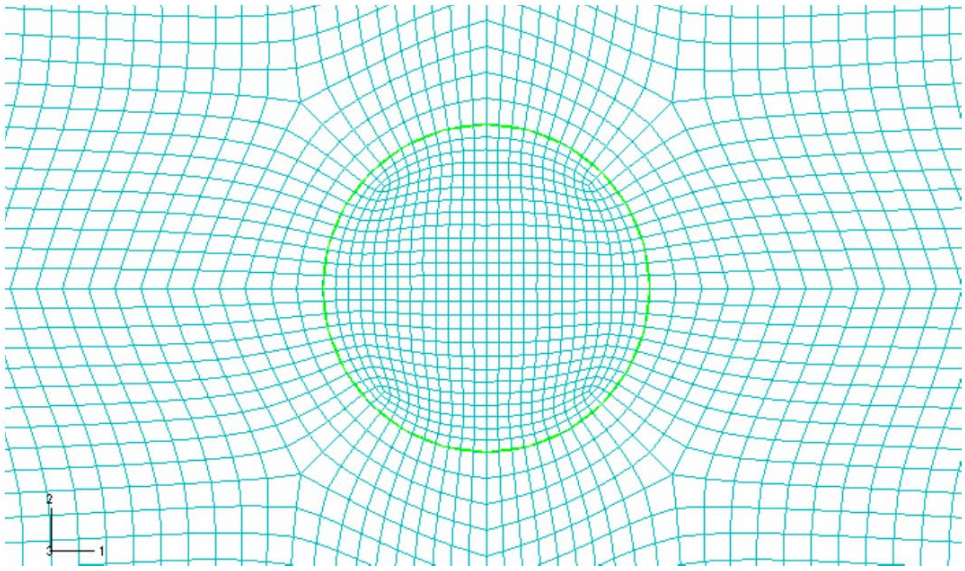

Figure 3: 2D finite element mesh of dowel/PCC interaction – fragment around dowel.

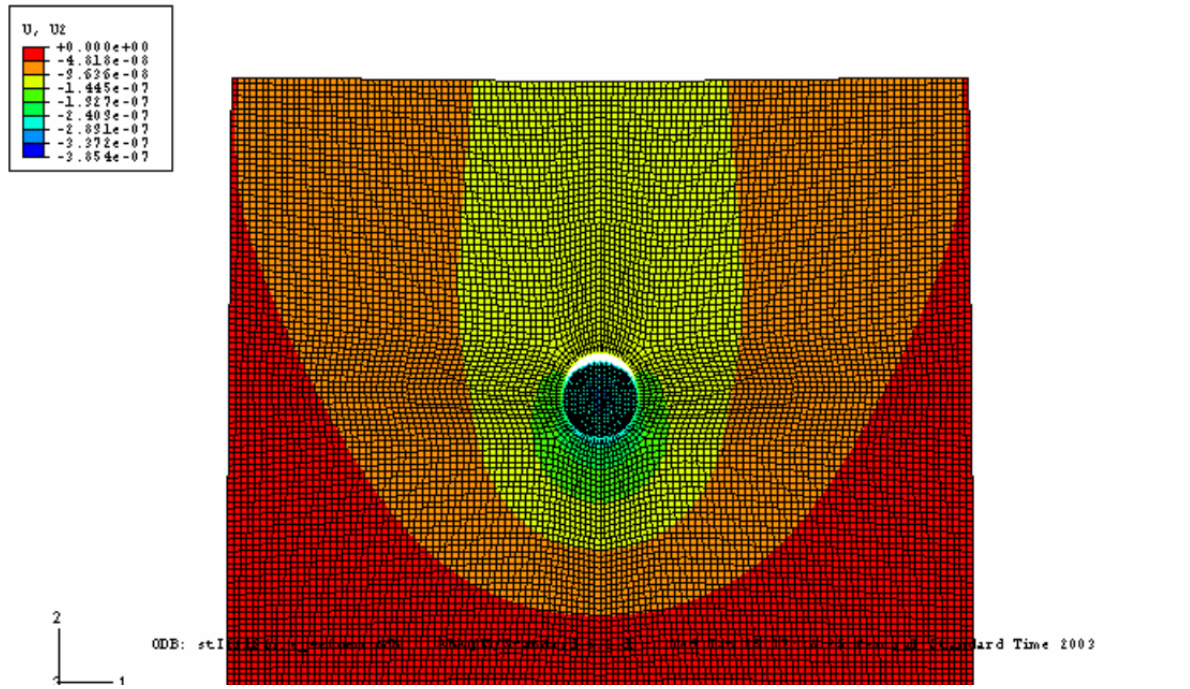

Figure 4: Typical contours of vertical displacements of concrete around a dowel bar (deformation scale factor is equal to 1,000,000.

The tests on doweled pavement joints were conducted in order to look critically at the compressive strength requirements for opening to traffic (see Figure 5). They found that critical stresses on the interface of the dowel and PCC can be predicted and used with allowable bearing stresses to predict strength requirements needed for opening to traffic. It was also found that field-cured cylinders protected by a clear plastic bag serve as a good representation of cylinders cored from the actual pavement due to the terrarium effect, which helps to prevent moisture loss. These cylinders can then be used to predict maturity and early-age compressive strength.

Figure 5: Exposed dowel test specimen.

Equations were then developed to show the correlation between compressive strength of the cylinders and beam flexural strength tests to estimate flexural strength in the concrete. This correlation was found to be:

$f'_r = 2.248\ f'^{2/3}_c$ $R^2 = 0.8365$ (Crovetti and Khazanovich 2005)

In addition, they concluded that doweled PCC pavements using 1.25-inch dowels should require a minimum opening compressive strength of 3,000 psi in order to prevent excessive bearing stresses. For doweled pavements utilizing 1.50-inch dowels, the required opening compressive strength may be reduced based upon pavement design characteristics. This results in a compressive strength ranging from 2,300 to 2,750 psi for a 10-inch slab on a 6-inch aggregate base.

Roesler et al. also looked at the structural factors of opening time to traffic (Roesler et al., 2000). As part of this study a compilation of opening strengths and strength data for fast-track projects were provided as can be observed in Table 1. Acknowledging that flexural fatigue cracking is the main concern with early opening to traffic, the study also listed the recommended opening flexural strengths for a variety of pavement features (see Table 2), concluding that a minimum flexural strength for all pavements was 300 psi.

Table 1: Opening strengths and other data for fast-track paving projects (Roesler et al., 2000).

Location and Description	Year	Cement Type	Cement Content kg/m^3 (lb/yd^3)	Water/Cement Ratio	Fly Ash kg/m^3 (lb/yd^3)	Curing/ Insulation	Opening Strength Specified MPa (psi)	Time to Meet Specified Strength, Hours
US-71 Bonded Overlay Storm Lake, IA	1986	III	380 (640)	0.45	42 (70) Type C	Wax-Based Compound/R=0.5 Blankets	Flexural 2.4 (350)	7.5
Runway Keel Reconstruction Barksdale AFB (LA)	1992	Special Blended	418 (705)	0.27	None	Wax Based Compound/None	4 Hr. Flex. 3.1 (450)	4
Highway 100 Intersection Replacements Cedar Rapids, IA [1]	1988	III	440 (742)	0.380	47 (80) Type C	Wax-Based Compound/R=0.5 Blankets	12 Hr. Flex. 2.8 (400)	7.5
SR-81 Arterial Reconstruction Manhattan, KS	1990	III	427 (719)	0.44	None	Wax-Based Compound/R=0.5 Blankets	Flexural 3.1 (40)	24
Lane Addition to I-496 Lansing, MI	1989	III	(418 (705)	0.45	None	Wax-Based Compound/R=0.5 Blankets	24 Hr. Flex. 3.8 (550)	19
I-25 to I-70 Interchange Ramp Reconstruction Denver, CO	1992	I	446 (752)	0.32	None	Wax-Based Compound & Plastic Sheets/None	12 Hr. Comp. 17.2 (2500)	8 [3]
Single-Route Access Road Reconstruction Dallas County, IA	1987	III	380 (640)	0.425	42 (70) Type C	Wax Based Compound/None	Flexural [2] 2.4 (350)	9
Interstate 80 Widening Rawlins, WY	1992	III	(390 (658)	0.47	None	Wax Based Compound/None	24 Hr. Comp. 20.7 (3000)	20 [3]
SR 832 and I-90 Interchange Reconstruction Erie County, PA	1991	I	446 (751)	0.37	None	Monomolecular Compound & Plastic Sheets/R=2.5 Blankets	24 Hr. Comp. 20.7 (3000)	13
I-70 Bonded Overlay Copper County, MO	1991	III	421 (710)	0.40	None	Polyethylene Sheets/None	18 Hr. Comp. 24.1 (3500)	10
Runway 18/36 Extension Reconstruction Dane County, WI	1992	III	392 (660)	0.455	None	Wax Based Compound/None	12 Hr. Comp. 24.1 (3500)	11 [3]
SR 13 Bonded Overlay North Hampton, VA	1990	II	445 (750)	0.420	None	Wax-Based Compound.R-0.5 Blankets	24 Hr. Comp. 20.7 (3000)	18
US-81 Reconstruction Menominee, NE	1992	III	363 (611)	0.423	None	Wax Based Compound/None	24 Hr. Comp. 24.1 (3500)	36
US-70A Inlay of Asphalt Intersection Approaches Smithfield, NC	1990	I	424 (715)	0.35	None	None/R=0.5 Blankets	48 Hr. Flex. 3.1 (450)	18

1) Contractor had two fast track mix choices on the project depending on the desired set speed – details are for faster set mix and intersection work.
2) Centerpoint flexural strength (flexural strength for all other projects in table are third point).
3) Interpreted from available data.

Table 2: Recommended flexural strength (psi) for opening (Roesler et al., 2000).

Slab Thickness in. (cm)	Foundation Support psi/in. (kPa/cm)	Modulus of Rupture for Opening (psi), to Support Estimated ESALs Repetitions to Specified Strength				
		100	500	1000	2000	5000
8 (20.3)	100 (271)	370	410	430	450	470
	200 (543)	310	340	350	370	390
	500 (1357)	300	300	300	300	310
8.5 (21.6)	100 (271)	340	370	380	400	430
	200 (543)	300	300	320	330	350
	500 (1357)	300	300	300	300	300
9 (22.9)	100 (271)	300	300	320	360	390
	200 (543)	300	300	300	300	320
	500 (1357)	300	300	300	300	300
9.5 (24.1)	100 (271)	300	300	300	330	350
	200 (543)	300	300	300	300	300
	500 (1357)	300	300	300	300	300
10 (25.4)	100 (271)	300	300	300	300	320
	200 (543)	300	300	300	300	300
	500 (1357)	300	300	300	300	300
10.5 (26.7)	100 (271)	300	300	300	300	300
	200 (543)	300	300	300	300	300
	500 (1357)	300	300	300	300	300

Van Dam et al. also looked at the structural considerations for guidelines with respect to durability, material, proportioning, testing, and construction for early opening to traffic rehabilitation (Van Dam et al. 2005). As part of this study, the state highway agency specifications for early opening materials were evaluated and organized in groups of 6-8 hour opening (see Table 3) and 20-24 hour opening (see Table 4). It can be observed that there is not only a large variation from state to state in terms of mix proportioning, but also in metrics (time and/or strength) and cut-off specification values used as the criteria for opening.

Table 3: State highway agency specifications for 6 to 8 hour opening (Van Dam et al., 2005).

State	Mixture Designation	Opening Criterion	Cement Type	Cement Factor	*w/c* Ratio	Coarse Aggregate	Fine Aggregate	Accelerator	Air Content	Mineral Admixture	Water Reducer
AR	Accelerated Strength	>14 MPa (2,000 psi) completed @ 6 hours	Type III	NS	NS	No. 57	NS	CC or other	NS	NS	NS
CA	Type FSHCC	>2.8 MPa (400 psi) flexural @ 8 hours	CSA	NS	NS	37.5 or 25 mm (1.5 or 1.0 in.) maximum	NS	Retarder and Type C used	NS	NS	NS
FL	Patching	>21 MPa (3,000 psi) completed @ 24 hours 6-hour opening	NS	>446 kg/m^3 (750 lb/yd^3)	< 0.45	57 Stone	NS	1% CC or Type C	2 to 6%	NS	Type F allowed
IL	Class PP(2)	8-hour opening	Type I	440 kg/m^3 (740 lb/yd^3)	< 0.38	1,020 kg/m^3 (1,720 lb/yd^3)	665 kg/m^3 (1,120 lb/yd^3)	Type E or Type C	4 to 6%	NS	Type F
IA	Class M	5-hour opening	Type I or Type II	~470 kg/m^3 (790 lb/yd^3)	~0.33	Volume specified	Volume specified	CC	5% w/ CC 6.5% w/o	No	NS
	Class FF	5-hour opening	Type III	~490 kg/m^3 (825 lb/yd^3)	~0.43			Not Allowed	6.0%		Yes
KS	Accelerated Cure	4- to 6-hour opening	Type III	>390 kg/m^3 (658 lb/yd^3)	NS	NS	NS	1 to 2% CC	NS	NS	NS
MD	6 hours or 7 hours	> 17 MPa (2,500 psi) completed @ 12 hours	Type I	>445 kg/m^3 (750 lb/yd^3)	< 0.42	No. 57	NS	CC or NC Type C	5.5%	NS	Type F, Melamine
MN	3A32HE	12-hour opening time	Type I	30% extra	NS	NS	NS	Type E	6.5%	NS	Type E
MI	Type SLP	> 2.0 MPa (290 psi) flexural @ 8 hours	Type I	502 kg/m^3 (846 lb/yd^3)	NS	MDOT 6A	NS	CC	5.5%	NS	NS
MO	4 hours	> 24 MPa (3,500 psi) completed	Type I or III	475 kg/m^3 (800 lb/yd^3) for Type I	NS	NS	NS	CC or other	NS	NS	NS
NJ	VHES	> 2.4 MPa (350 psi) flexural @ 6.5 hours	Type I w/ accelerator or Type III	>390 kg/m^3 (658 lb/yd^3)	0.37	No. 57	NS	NC required	6.5%	NS	Type F
NY	Patch	Surface temperature of 65°C (150°F)	Type III	490 kg/m^3 (825 lb/yd^3)	0.39	NYDOT CA2	NS	2% CC	6.0%	NS	NS
OH	Class FS	2.8 MPa (400 psi) flexural @ 4 hours	Type I	534 kg/m^3 (900 lb/yd^3)	< 0.40	No. 57, No. 6, No. 67, or No. 8	NS	1.5% CC or other	6.0%	NS	Type D
PA	Accelerated	8.3 MPa (1,200 psi) completed @ opening 10 MPa (1,450 psi) completed @ 7 hours	NS	NS	NS	No. 57	Type A	NC allowed	6.0%	NS	NS
TX	Class K	2.9 MPa (420 psi) flexural @ 24 hours, Open @ 1.8 MPa (260 psi) flexural	Type III	390 kg/m^3 (658 lb/yd^3)	< 0.49	Grade 2 or 3	Grade 1 FM 2.6 to 2.8	Type C	NS	NS	Type A
WI	Special HES	21 MPa (3,000 psi) completed @ 8 hours	NS	>502 kg/m^3	NS	NS	NS	CC or other	NS	NS	NS

CC: calcium chloride.
CSA: Calcium sulfoaluminate cement.
NC: non-chloride.
NS: not specified.
VHES: very high early strength.

Table 4: State highway agency specifications for 20 to 24 hour opening (Van Dam et al., 2005).

State	Mixture Designation	Opening Criterion	Cement Type	Cement Factor	*w/c* Ratio	Coarse Aggregate	Fine Aggregate	Accelerator	Air Content	Mineral Admixture	Water Reducer
AR	HES	>21 MPa (3,000 psi) completed @ 24 hours	Type I Type III	25% extra NS	NS	NS	NS	NS	NS	NS	NS
GA	24-Hour Accelerated	>17 MPa (2,500 psi) completed @ 24 hours	Type I or Type III	420 kg/m^3 (700 lb/yd^3)	< 0.45	NS	NS	CC Or Type E	3 to 6%	NS	NS
IL	Class PP(1)	> 22 MPa (3,100 psi) completed > 4.2 MPa (600 psi) flexural @ 48 hours	Type III or Type I	NS	NS	NS	NS	Accelerator required	NS	NS	NS
IN	High Early	3.8 MPa (550 psi) flexural @ 48 hours	Type I or Type III	>335 kg/m^3 (564 lb/yd^3)	<0.42 <0.45	NS	NS	NS	6.5%	10% flyash 15% GGBFS	Type A
KS	Normal Cure	24-hour opening	Type I or II	>445 kg/m^3 (750 lb/yd^3)	NS	NS	NS	No	NS	NS	NS
MD	24 hours	> 17 MPa (2,500 psi) completed @ 12 hours	Type I	>475 kg/m^3 (800 lb/yd^3)	NS	NS	NS	NS	NS	NS	Type F
MN	3A32HE	24-hour opening time	Type I	30% increase	NS	NS	NS	NS	6.5%	NS	Type A
MI	Type P-MS	> 3.5 MPa (500 psi) flexural @ 24 hours	Type I	502 kg/m^3 (846 lb/yd^3)	NS	NS	NS	CC below 18°C (65°F)	5.5%	NS	NS
MO	24 hours	>24 MPa (3,500 psi) completed	Type I	475 kg/m^3 (800 lb/yd^3) for Type I	NS	NS	NS	NS	NS	NS	NS
OH	Class MS	2.8 MPa (400 psi) flexural @ 24 hours	Type I	475 kg/m^3 (800 lb/yd^3)	< 0.43	No. 57, No. 6, No. 67, or No. 8	NS	NS	6.0%	NS	Type D
TX	Class K "Modified"	2.1 MPa (300 psi) flexural @ 24 hours	Type I or Type III	390 kg/m^3 (658 lb/yd^3) 335 kg/m^3 (564 lb/yd^3)	< 0.53	Grade 2 or 3	Grade 1 FM 2.3 to 3.1	Type C allowed	NS	NS	Type A or D

CC: calcium chloride.
GGBFS: ground granulated blast furnace slag.
HES: high early strength.
NC: non-chloride.
NS: not specified.

The study concluded that designing and constructing both durable 6 to 8 hour and 20-24 hour early opening concrete pavement was feasible. However, the proportioning and construction of such pavements were deemed to be particularly challenging. Since that study did not look at testing methods that could be applied in both the laboratory and field, there were no conclusions with regard to whether or not this challenge was met to allow for the benefits of early opening to traffic. This highlights the need for methods capable of nondestructively monitoring the consistency and construction of early opening strength pavements, which is the subject of the next section.

2.2 Field and Laboratory Testing

2.2.1 Maturity Method

Maturity is a measure of how far the hydration reaction has proceeded and can indicate how much strength the concrete has gained. A strong correlation has been found between maturity and flexural strength development (Olek et al 2003). Both time and temperature affect the maturity of the concrete. The example, shown in Figure 6, shows that if one specimen of a given concrete mix is cured at a lower temperature and another is cured at a higher temperature, they should both have equal strength once they have reached the same level of maturity (Nelson 2003).

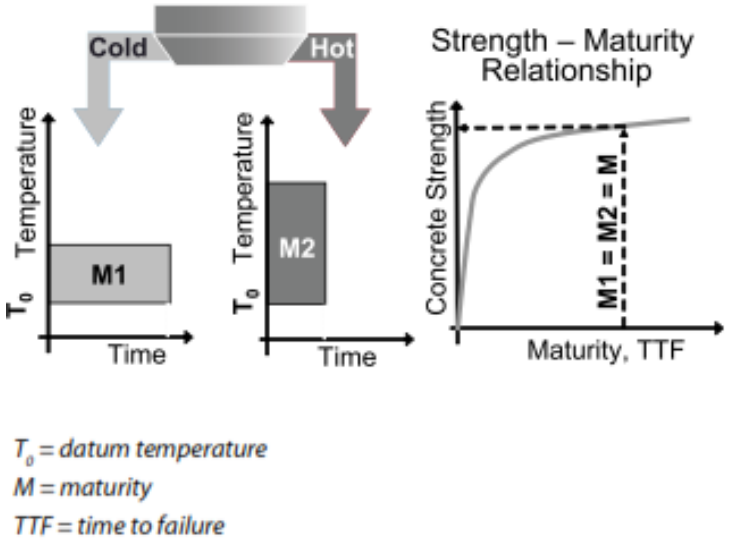

Figure 6: Two samples of the same concrete mix cured at different temperatures will reach the same strength level at the same maturity level (from Nelson 2003).

As mentioned above, maturity can be quantified based on time if the hydration properties of the mix are known. Maturity can also be quantified based on temperature because the hydration reaction has a distinct temperature versus time curve, see Figure 7. However, in recognition that maturity is a function of both temperature and time (Smith 2005), maturity is typically quantified in degree-days or degree-hours (see Figure 7 and Figure 8).

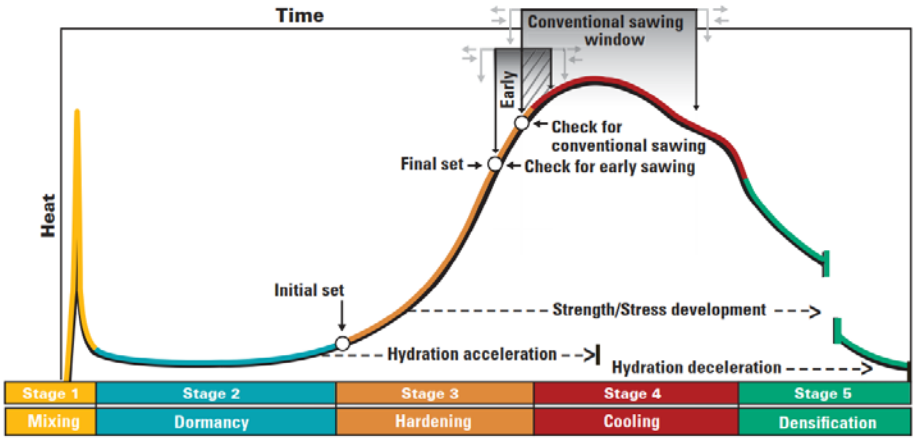

Figure 7: Curve of temperature versus time in the cement hydration cycle (from CP Tech Center 2007).

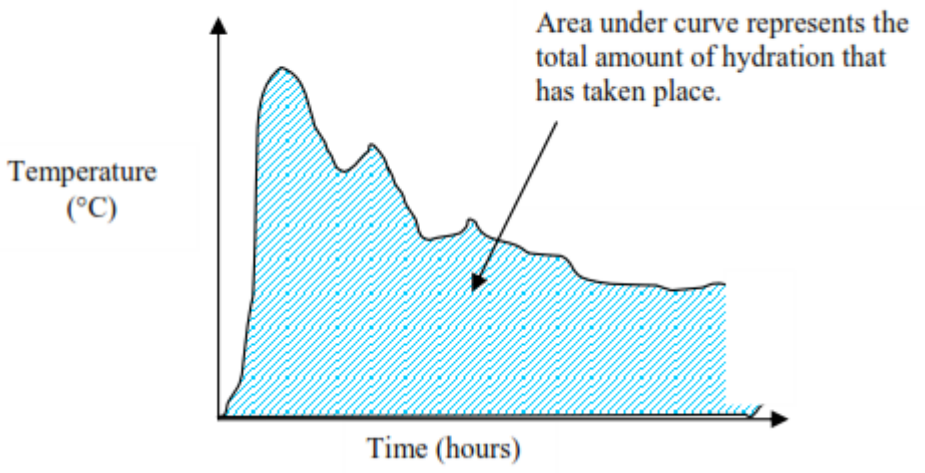

Figure 8: Relation between maturity, time, and temperature (from Olek et al 2003).

The Nurse-Saul maturity relationship is the generally accepted method for calculating maturity based on both time and temperature. This relationship takes the form of (Crawford 1997, ACPA 2002):

$$M = \sum (T_a - T_0)\Delta t$$

Where:

M = maturity (time-temperature factor) at age t

T_a = average concrete temperature during time interval Δt

T_0 = temperature datum, typically taken as -10°C (Carino 2004)

Δt = time interval

While the Nurse-Saul equation is quite simple, it does have a few disadvantages. It is not as adept at predicting maturity as other methods when a wide range of curing temperatures is considered. Additionally, the Nurse-Saul equation assumes that strength gain of concrete is a linear function, which may not be the case (Carino 2004). However, the simplicity of this equation has made it quite popular despite its disadvantages and it is an accepted function in the maturity testing specification ASTM C1074 (ASTM 2005).

Another means of computing maturity is through use of the Arrhenius method, which estimates maturity in terms of an equivalent age, or equivalent duration of curing at a reference temperature required to produce the same level of maturity as curing at the actual temperature. The Arrhenius equation is given by:

$$t_e = \sum \exp\left[-\frac{E}{R}\left(\frac{1}{273 + T_a} - \frac{1}{273 + T_r}\right)\right]\Delta t$$

Where:

t_e = equivalent age at reference curing temperature

E = activation energy in J/mol

= 33500 for T ≥ 20°C

= 33500 + 1472(20 - T) for T < 20°C

R = university gas constant = 8.3144 J/(mol K)

T_a = average concrete temperature during time interval Δt, in °C

T_r = reference temperature, in °C

Δt = time interval

Though this method is decidedly more complicated than the Nurse-Saul equation, it also produces better results (Carino 2004). It is also an acceptable means of computing maturity under ASTM C1074 (ASTM 2005). To use the maturity method, a strength-maturity relationship (also called a maturity calibration curve) must be developed for each mix. This involves casting 12-15 beams or cylinders for each mix to be used and outfitting some of them with temperature probes. Once the specimens have been cured, the ones without the probes are tested at various times to determine their flexural or compressive strength and the temperature of the probed specimens is recorded at that time. From these measurements, the maturity is computed and a maturity curve is constructed, see Figure 9 (Smith, 2005).

The maturity of the specimen can be computed from the maturity curve using Simpson's 3/8th rule (Olek et al. 2003):

$$Maturity = \Sigma TTF = \sum \left(\frac{temp_i + temp_{i+1}}{2} + 10 \right) * (age_i - age_{i+1})$$

Where:

ΣTTF = cumulative maturity at a particular age

$temp_i$ = initial temperature in time interval i

$temp_{i+1}$ = final temperature in time interval i

age_i = initial age of the specimen at the beginning of interval i

age_{i+1} = final age of specimen at the end of interval i

If any changes are made to the concrete mix during the project (such as a change in material suppliers, different batching, etc.), new testing must be conducted to construct new maturity curves.

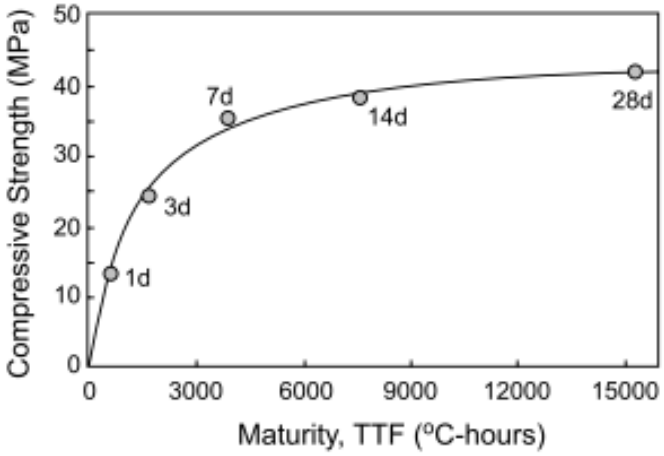

Figure 9: Sample maturity curve (from Nelson 2003).

The effect of concrete mix design parameters on maturity measurements was investigated by Rohne and Izevbekhai in 2009. The results from their testing can be seen in Figure 10 and Figure 11 below. Figure 10 shows the maturity flexural strength curves, while Figure 11 shows maturity compressive strength curves for varying concrete mixes. The concrete mixes utilized

two different cements and two fly ashes with the same w/c ratio for all mixes. As can be seen from the figures, there are only slight variations in the maturity curves.

Concrete pavements often experience flexural failure, thus the flexural strength which develops within the concrete during the early hours of setting is crucial. Using the maturity method to determine this flexural strength is advantageous in that it gives a good representation of the strength compared to the subjected stresses. Although most research available focuses on maturity curves using compressive strength tests, comprehensive flexural strength and maturity correlations curves were also developed by Wilde. Several of these relationships are given in Figure 12 (Wilde 2013).

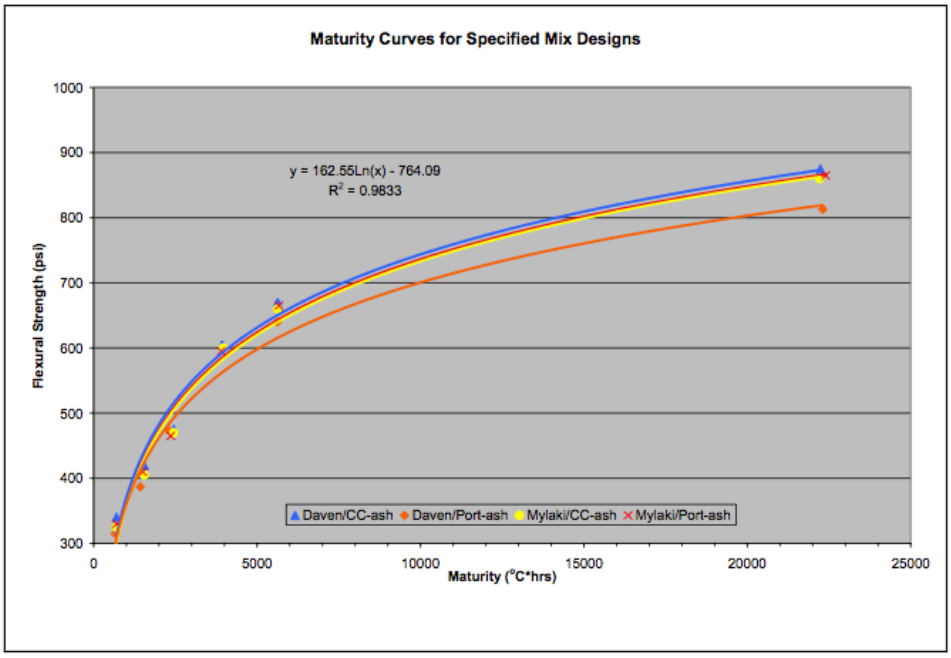

Figure 10: Flexural strength vs. maturity (Rohne and Izevbekhai 2009).

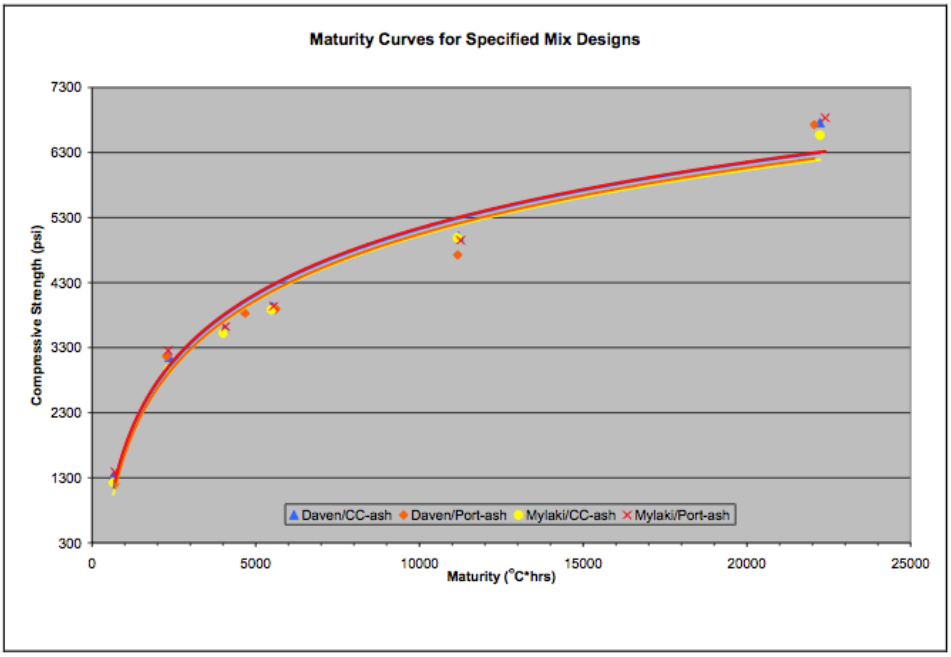

Figure 11: Compressive strength vs. maturity (Rohne and Izevbekhai 2009).

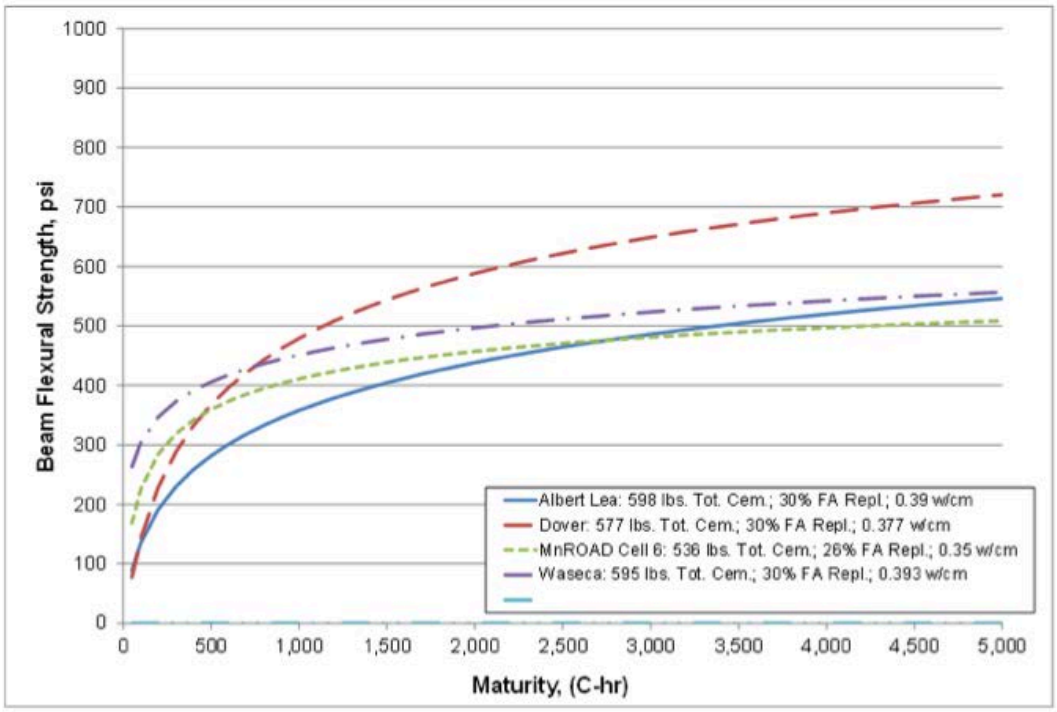

Figure 12: Flexural strength vs. maturity (Wilde 2013).

While maturity is a powerful tool, there are some complications with this type of testing. Having to construct a maturity curve for each mix considered is one drawback to maturity testing. Other

disadvantages include occasional problems with matching laboratory cured specimen curing conditions, assumed datum temperatures, and activation energies with the particular concrete mixture placed in the field. Additionally, if temperatures are high at early ages, predictions of long-term strength gain can be incorrect. Maturity testing also cannot show if errors have been made in the placement, consolidation or curing of the concrete (NRMCA 2006).

2.3 Active Nondestructive Testing Methods

To address some of the complications with passive methods such as maturity, active nondestructive testing methods should be conducted to provide supplemental information. These active methods are capable of testing large areas of in-situ pavement without damaging the structure through the use of non-intrusive signals. Common nondestructive evaluation techniques that have the potential to provide this complementary information include ground penetrating radar (GPR), electromechanical impedance methods, sounding methods such as chain dragging, impact echo, spectral analysis of surface waves, ultrasonic pulse velocity (UPV), ultrasonic pulse-echo, ultrasonic wave reflection, and ultrasonic tomography. Discussion of the state-of-the-art and limitations of each of these methods is given in this section.

2.3.1 Ground Penetrating Radar (GPR)

Ground penetrating radar (GPR) transmits electromagnetic waves into the test medium and the reflection of those waves at interfaces of different dielectric properties gives information about changes in the test medium. The wave speed is dependent on the dielectric properties of the material, and can be used with various signal interpretation methods to determine the target depth (Cao et al. 2008; Cao et al.; 2011; Cao 2011; Abdallah,2009; Clemena 1991; Economou et al. 2012; Louliza et al., 2001; Maierhofer, 2003; Plati et al., 2012; Scott et al., 2000). GPR has been applied in the past for detection of reinforcement corrosion (Arndt, 2011; Clemena et al., 1992), inspection of bridge deck pavement (Belli et al 2008), structural assessment (Benedetto et al., 2012; Catapano et al., 2012), highway pavement structure characterization (Maser, 1996; Maser, 2000; 1996; Maser, 2008; Maser et al. 1990; Morey, 1998; Scullion et al., 1995), airport pavement assessment, (Moropoulou et al., 2002), concrete thickness (Davis et al., 2005, Cao et al., 2011; SAARENKETO et al., 2000), and identification of delamination in concrete pavements (Li et al., 2008).

GPR was considered for use since MnDOT owns several equipment and the material properties are theoretically related to the dielectric constant of the early age concrete that can be measured using GPR. However, since water content has a much larger effect on the composite PCC properties (Arndt, 2011) than strength, the information provided by GPR would need to be normalized for proper use. Figure 13 shows a MnDOT owned and operated 2.6 GHz ground-coupled antenna and example output as well as an example output of GPR where parabolic reflections can be observed due to the presence of dowel bars (Cao et al., 2011). The surface of the concrete in the GPR outputs appears flat because the antenna is in continuous contact with the surface while being dragged.

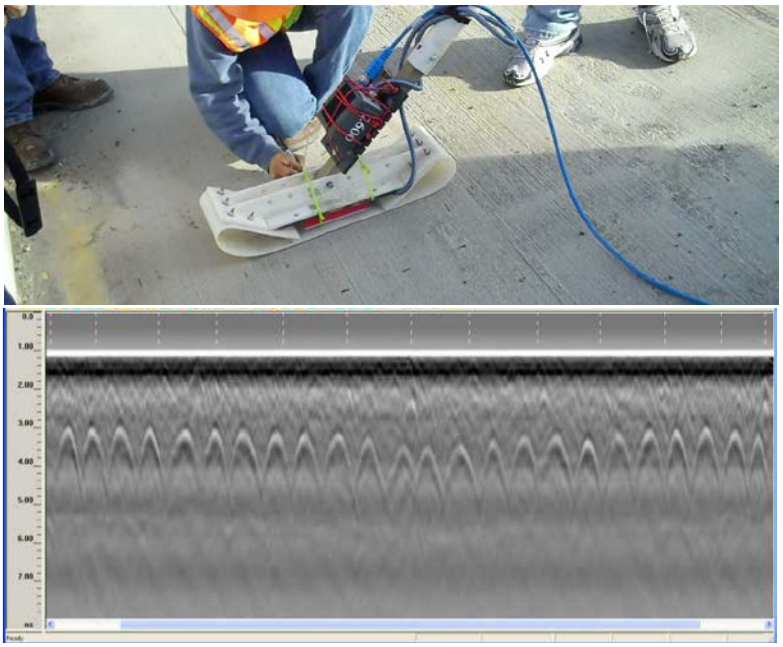

Figure 13: Ground coupled GPR and example output at a transverse joint. Downward hoop signals indicate dowel bars or reinforcement.

GPR can also be operated using air coupled antennas such as the one shown in Figure 14. Past studies show that GPR is capable of achieving high speed measurements of pavements although the accuracy reduces with higher speeds and detecting non-uniform cracks is difficult (Griffiths et al., 1999). GPR is highly sensitive to environmental conditions since water has a high dielectric constant, therefore moisture conditions have a large effect on GPR signals (Scott et al 2003; Griffiths et al., 1999).

Figure 14: Air coupled step-frequency GPR mounted on a van for high speed measurements.

2.3.2 Electromechanical Impedance

Providakis, Liarakos and Kampianakis (2013) focused on nondestructive monitoring of strength gain using an electromechanical impedance sensing system. Small PZT patches were used to act as actuators to monitor the changes in electrical impedance of the structure being tested. A chip used to measure impedance was placed inside a Teflon enclosure in order to facilitate signal processing. The findings from these tests were centered on a metric called the Root Mean Square Deviation (RMSD), which can be computed using the equation below:

$$RMSD(\%) = \sqrt{\frac{\sum_{n=1}^{F}[Re\{Z(\omega_n)\} - Re\{Z_0(\omega_n)\}]^2}{\sum_{n=1}^{F}[Re\{Z_0(\omega_n)\}]^2}} \times 100$$

In this equation, F is the number of sample points in the impedance spectra, where $Z(\omega_n)$ is the real part of impedance of the nth frequency of a specific day and $Z_0(\omega_n)$ is the resistance of the nth frequency of the 3rd hour of the concrete curing process.

It was found that the rate of change of the RMSD, divided by the elapsed time, peaks somewhere in the 9-12 hour range. This peak is then followed by a sudden decrease and then a constant value is reached up to the 28th day (Providakis et al 2013). These trends allow for a possible method of predicting setting time of concrete in a nondestructive way.

2.3.3 Conventional impact echo (IE)

Conventional impact echo (IE) is one commonly used elastic wave based method (see Figure 16) involving generation of compression, shear, and Rayleigh waves using a mechanical impact at the surface (Schubert et al., 2001). The waves, reflected from internal changes in acoustic impedance or external boundaries and recorded on the surface where the impact was generated, give information about the structure using signal interpretation techniques normally based on spectral analysis (Scott et al., 2003).

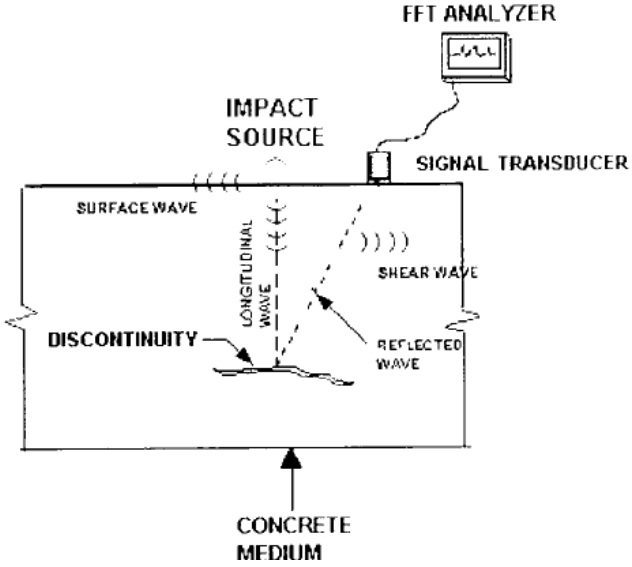

Figure 15: Schematic illustration of the IE test (Scott et al 2003).

If the propagation velocity is assumed, the frequency spectrum can be used to determine the depth of the discontinuity or thickness of the material using the relationship given below (Scott et al 2003, Schubert et al., 2008):

$$D = \frac{C_p}{n*f}$$

Where D is the depth of the discontinuity, f is the resonant frequency between the impact and the discontinuity, C_p is the pressure wave (p-wave) velocity, and n is assumed to be 2 according to the full travel path to the reflecting interface and back. An n=2 factor is generally valid for most cases that impact echo is used for such interfaces with very large impedance mismatch between the two materials like concrete/air interface (Schubert et al., 2008; Schubert, 2001). Figure 16 shows a typical conventional impact echo setup with a round metal ball used to create the impact (Carino, 2001; Sansalone, 1997). IE is capable of detecting planar layer interfaces, which can be used for thickness determination or the detection of other plate-like inclusions. Testing with this method can be time consuming and only allows for one signal pair to be sent and received per scan. With only one mechanical impact signal and analysis methods that require multiple reflections at the same boundary using frequency domain analysis, there are difficulties in evaluating the complex geometries required for irregular flaw detection (Carino, 2001; Schubert, 2008; Schubert, 2003). Novel evaluation techniques and hardware such as air coupled impact echo, have been developed to allow for more productive measurements and multiple measurement pairs (Borwick, 1990; Buckley, 1999; Popovics, 2012; Zhu et al., 2002; Zhu et al., 2007). While this method has typically been used to detect structural discontinuities or flaws in PCC using an assumed or core determined PCC velocity, it can be observed from the equation that velocity (and thus potentially strength gain) can be determined using this method if the structure thickness is assumed to be constant. While this method is attractive since it incorporates material properties throughout the depth, this method would require a low variability in the thickness to produce accurate results. In the case of concrete pavements, the typically achieved variability can cause errors in the velocity calculation when using this method.

Figure 16: Impact echo setup with a steel ball mounted on a steel spring rod (Carino, 2001).

2.3.4 Spectral Analysis of Surface Waves (SASW)

Spectral analysis of surface waves (SASW) is another acoustic based method. The dispersion of Rayleigh waves gives information about the material in which it propagates. This method has been used for applications such as estimating concrete pavement stiffness and other properties (Krstoluvic-Opara et al. 1996; Cho, 2003; Gucunski et al., 1992). The surface displacements recorded by displacement transducers from various wave frequencies from mechanical impacts are analyzed using the setup shown in Figure 17. Complex geometries or non-planar defects can be difficult to analyze using this method (Park et al., 1999; Stokoe et al., 1994).

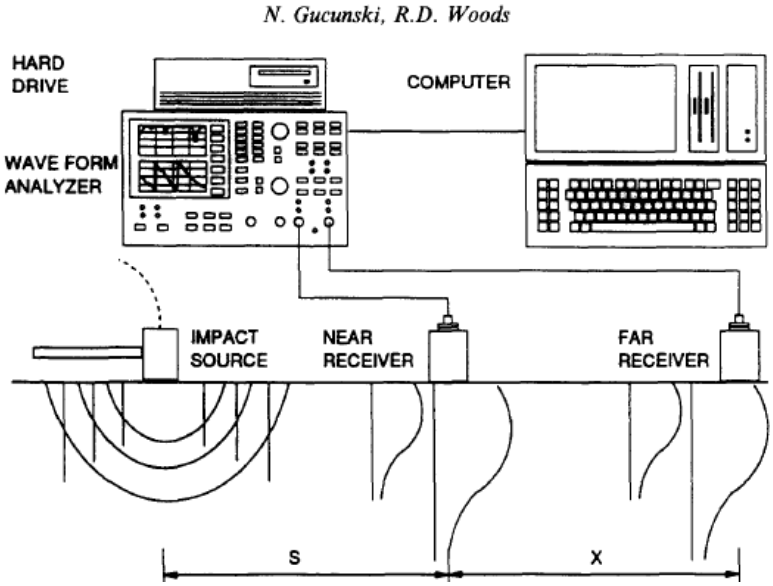

Figure 17: Schematic of the SASW (Gucunski, Soil Dynamics, 1992).

2.3.5 Ultrasonic Pulse Velocity

Ultrasonic pulse velocity (UPV) is an elastic wave based method where the impulse is emitted and received directly by an ultrasonic transducer (Popovics et al., 1992). Figure 18 shows various transducer pair setups used for UPV testing, where the direct arrival is received (a) on the opposite side, (b) at an angle, or (c) along the surface. For concrete pavement applications with only one-sided access such as field testing for early opening in this project, the setup shown in Figure 18 (c) is often the only applicable measurement type.

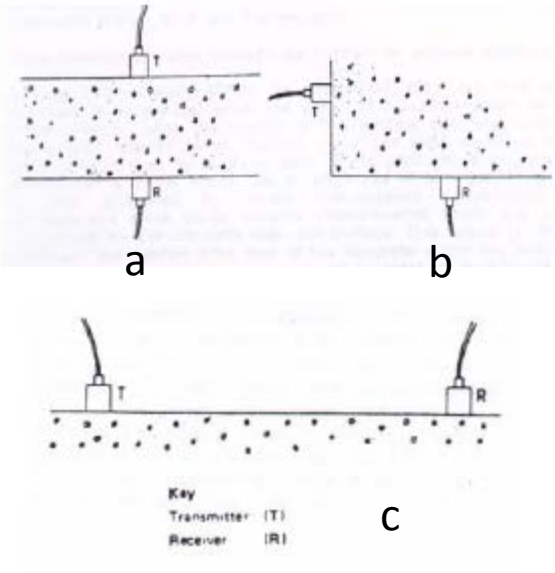

Figure 18: Various sending and receiving positions for UPV testing (Adapted from International Atomic Energy Agency, 2002).

The direct arrival of the elastic wave of interest (P-wave in this example) is used to determine the wave velocity by simply taking the distance traveled divided by time of propagation:

$$C_p = \frac{L}{T}$$

Where L is the path length, and T is the time taken by the pulse to traverse that length. Conventionally, the pulse is transmitted into and received from the concrete using a liquid coupling material such as grease or cellulose paste to transfer the vibration to the concrete and back. This process can be time consuming and often confines UPV testing to laboratory and/or testing of samples rather than on-site concrete pavement testing.

Graveen proposed measurement of P-wave velocity as a supplement to increase the overall confidence of the maturity-based estimate of concrete strength (Graveen 2001). Figure 19 shows the testing setup used at that time required for calculation of the compression wave velocity. It can be observed that the measurement required time-consuming application of fluid couplant to allow for transmission and reception of the wave. In this method, the measurement set-up had to be repeated at 2.36, 4.72, 7.09, 14.2, and 16.5 in. to obtain consistent results. Despite the problems with speed and coverage with the method, the study showed that "the correlation of the P-wave velocity to concrete strength is supported by the similarity between the strength-age

relationship and the P-wave velocity-age relationship" for field tests, and reducing error in the P-wave velocity measurements would increase the confidence in the reported P-wave velocity.

Figure 19: Surface transmission pulse velocity (Graveen 2001).

The relatively recent technological advances in dry point contact (DPC) transducers provide a lower frequency, higher power impact without the need for liquid coupling. DPC transducers, manufactured by Acoustic Control Systems, are capable of transmitting low frequency elastic waves (30 kHz to 150 kHz) allowing for ultrasonic methods that can penetrate greater distances in pavement applications (Nesvijski, 1997; Liang et al., 2009; Moheimani, 2003; Nesvijski, 1997; Vladisauskas et al., 2011; Vladisauskas et al., 2010; Dutoit, 2005). The "touch and go" measurements with fixed transducer locations speed up the data collection process and eliminate many of the issues with conventional ultrasonic testing as applied to concrete structures. Figure 20 shows an ultrasonic pulse velocity (UPV) device that was one of the first applications of these types of transducers for pavement applications (Khazanovich et al., 2005).

Figure 20: UK1401 ultrasonic pulse velocity device (Khazanovich et al., 2005).

2.3.6 Ultrasonic Wave Reflection

The ultrasonic wave reflection method involves measuring the reflection coefficient of shear waves between a steel plate and the concrete pavement. The reflection coefficient is a ratio dependent upon density and wave velocity of the two materials; essentially representative of the change in amplitude between the two reflections. The reflection coefficient is equal to one when the PCC is in a liquid state because shear waves cannot be transmitted through liquids. The reflection coefficient decreases as the PCC hardens and eventually stabilizes at a final value. This coefficient is governed by the dynamic shear modulus- a value that is based upon the level of hydration present.

Curing temperature differences have been seen as a weakness of the maturity method, but the wave reflection method was not affected by these changes. As a result of their testing, a power law function was found to model the relationship between reflection loss and compressive strength. This function can be seen below. This function was found to be valid from 9 hours to 3.5 days after casting. Here, S is equal to the compressive strength and R_L is the measured reflection loss.

$S = 4.224 \times {R_L}^{1.9158}$ (Voigt et al 2006)

Because compressive strength is also dependent upon hydration, it is thought that the compressive strength and reflection coefficient can be compared due to this common dependence. Tests by Voigt, Akkaya, and Shah proved that wave reflection measurements are repeatable and predictable for final value of reflection loss for mortar. However, these measurements are not able to be predicted for concrete because of the presence of aggregates at the local level (Voigt, 2003 and 2005). A relationship between strength and reflection loss was determined as follows:

$$S(t) = m \times \Delta A(t)$$
$$\Delta A(t) = [A(t) - A(t_s)]$$

Where S(t) is the predicted strength at time t, m is the slope of the strength to change in reflection loss relationship, and $t > t_s$. After this relationship is determined, prediction of compressive strength gain can be highly accurate. However, in order for this relationship to be properly predicted, results from compression tests performed within the first 24 hours must be performed and utilized. The results from the testing done by Voigt, Akkaya, and Shah can be seen below in Table 5 (Voigt et al 2003).

Table 5: Parameters of relevant relationships (Voigt et al 2003).

Batch (1)	m (2)	s of m (%) (3)	r^2 (4)
(a) Mortar			
M-1	19.064		0.988
M-2	19.454	3.10%	0.991
M-3	18.065		0.995
(b) Concrete			
C-1	14.652		0.981
C-2	20.414	13.39%	0.987
C-3	18.369		0.996

Further research on reflection loss was done by Voigt and Shah, along with Sun and Reinhardt. While most other research has been done solely on S-waves, this project included the use of P waves to determine if the wave transmissions could be used to monitor the concrete hardening process. In addition to the ultrasonic measurements, penetration resistance and chemical shrinkage were measured. P wave velocity was seen to increase although no change in setting behavior occurred. However, the point of inflection in the curve of P-wave velocity versus age coincided with the time of increase of penetration resistance. So while p-wave velocity changes do not necessarily signal changes in strength, the overall trend of rate of p-wave velocity can be useful in prediction of concrete strength. Increase in reflection loss was also seen to coincide with an increase in temperature, but it should be noted that p-wave velocity was seen to be less dependent on the time of temperature increase. Based on these observations, it was concluded that p-waves are affected by the formation of hydration products. However, this has no influence on early stiffening of concrete. It was also seen that the maximum temperature is reached when the reflection loss curve reaches its maximum rate of increase. In comparison to the shear wave test results that have been discussed, p-wave velocity was found to be related to Young's modulus and not to the shear modulus (Voigt et al 2005).

Voigt and Shah did further research focusing on the effect of water-cement ratios on the reflection loss method. They utilized three ratios ranging from 0.35-0.6, again seeing a bilinear relationship between reflection loss and compressive strength with high R^2 of 0.97 and above. In all cases, the early stage of setting showed a lower slope than the later portion. Regarding the effect of w/c ratios, the transition time between the two linear functions was earlier for the lower ratios. A linear relationship was also found between degree of hydration and reflection loss. For this relationship, higher slopes were seen when the w/c ratios were lowest (Voigt and Shah 2013). The early hydration period has also been the focus of some research, requiring the presence of a high impact resistance polystyrene (HIPS) as a buffer. This buffer has very similar acoustic impedance to cement paste, providing more reliable setting measurements of early age paste. Various chemicals solutions were tested in order to take a closer look at the stability of the buffer using ultrasonic wave reflection. Figure 21 shows the effect of buffer type on ultrasonic wave reflection measurements (Chung et al 2010). It can be observed that HIPS experiences a

greater dip in reflection coefficient than stainless steel and that these differences are most dramatic during the early hours of settlement. The results of this research showed that using a HIPS buffer results in the ability to determine P and S-wave reflection response at very early ages.

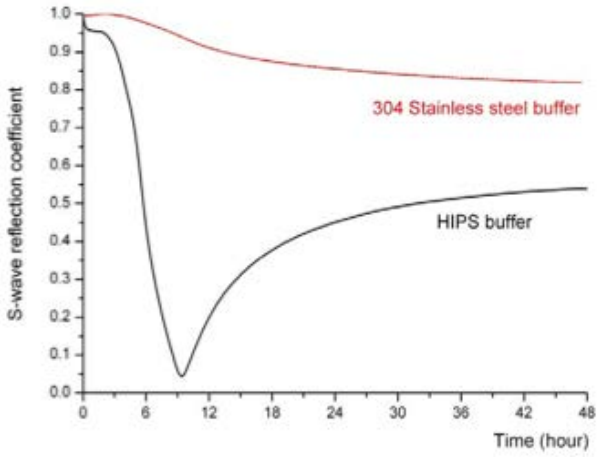

Figure 21: Reflection coefficient versus time (Chung et al 2010).

2.3.7 Ultrasonic Linear Array

While the traditional ultrasonic pulse velocity measurements and ultrasonic wave reflections provide useful information as described above, the ultrasonic array technology provides an opportunity to mitigate the issues with limited transducer pairs, signal variability, and sensor positional shift instability, using a self-contained arrangement of sending and receiving transducer pairs at set spacing. Ultrasonic testing is typically conducted between 750 kHz to 100 MHz, with a wide range of applications in both biomedical and industrial fields (VonRamm, O. T., 1976; Blouin et al., 1998; Minalga et al. 2012; Guzina et al., 2004; Liu, 2008; Lue, 2008; Rupitsh, 2006; Song, 2002; Spies et al., 2002). These types of systems use an array of elements within a single relatively large transducer to provide spatial diversity. Figure 22 shows an example ultrasonic phased array setup from (a) 1976 and (b) 2012, with elements phased within a linear array to focus the emitted wave (VonRamm, O. T., 1976; Minalga, 2012).

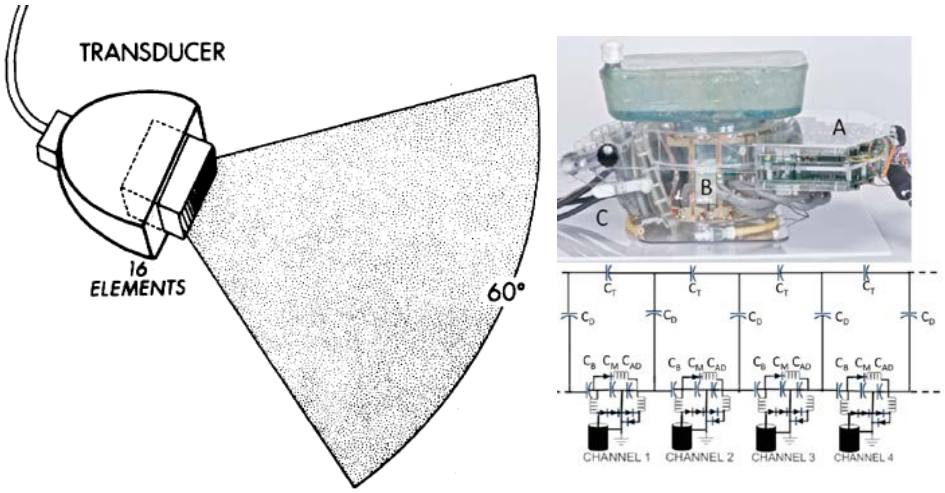

(a) VonRamm et al., 1976 (b) Minalga et al., 2013

Figure 22: Transducer array technology for biomedical use adapted from (a) VonRamm et al., 1976, and (b) Minalga et al., 2012.

To allow for testing of heterogeneous materials such as PCC in the field, DPC transducers, similar to the UPV device shown in Figure 20, are used which eliminates the need for a manual mechanical impact. This allows for transducer arrays with multiple angles of transmission and reception that can be used to also address some of the reliability issues dealing with conventional impact echo or UPV discussed previously (Shubert et al., 2008). This arrangement allows the transducer spacing to be reduced for higher precision measurements. Two versions of DPC ultrasonic array technology are shown in figures 23 and 24. The A1220, shown in figure 23, consists of sets of 12 emitting transducers and 12 receiving transducers. MIRA, shown in figure 24, consists of a linear array of 40 sending and receiving transducers arranged in 10 channels of 4 transducers.

Figure 23: A1220 ultrasonic pulse-echo device.

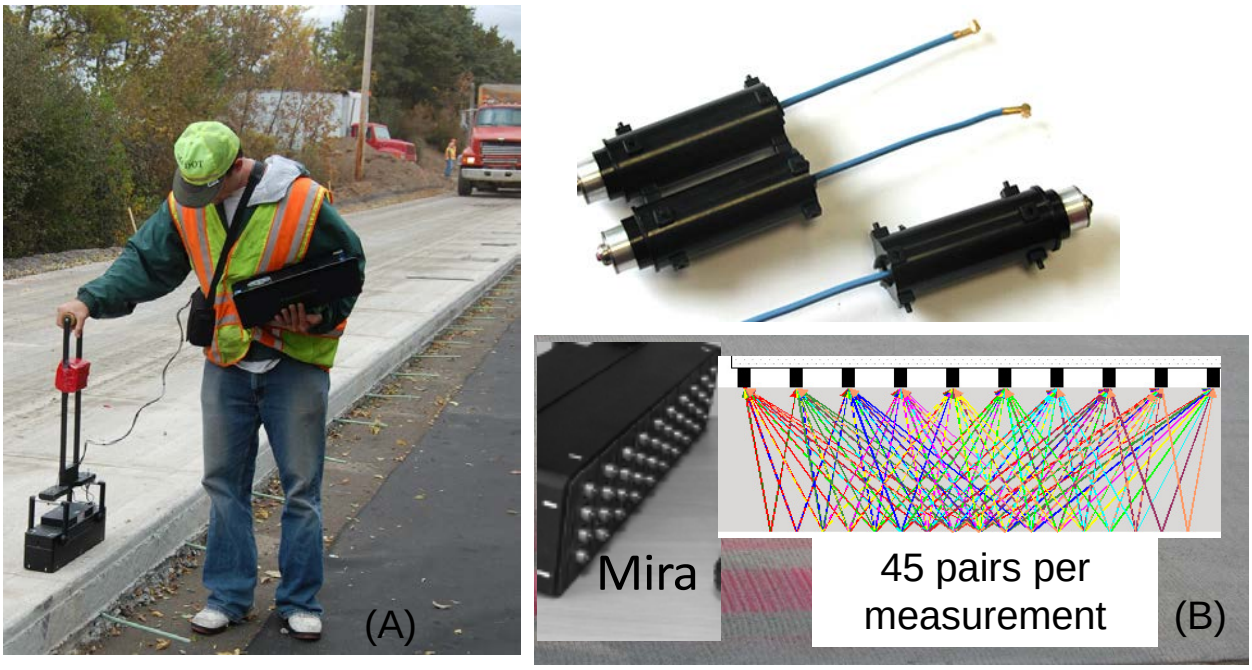

Figure 24: MIRA ultrasonic linear array device with a handle designed at the University of Minnesota for more productive measurements on pavement systems.

As observed in Figure 24, shear waves are emitted and received by multiple transducer pairs allowing for multiple incident angles and consistent analysis of elastically heterogeneous material such as concrete. MIRA incorporates 10 channels, each composed of four transmitting and receiving DPC transducers in a linear array. This linear array operates in a multi-static nature, allowing for 45 transmitting and receiving impulse time-history measurements.

The spacing between adjacent transducer channels is 40 mm (1.6 in.). Thus, horizontally spaced measurement pairs in each MIRA scan include nine pairs at 40 mm (1.6 in.) spacing, eight pairs at 80 mm (3.1 in.) spacing, seven pairs at 120 mm (4.7 in.) spacing, six pairs at 160 mm (6.3 in.) spacing, five pairs at 200 mm (7.9 in.) spacing, four pairs at 240 mm (9.4 in.) spacing, three pairs at 280 mm (11.0 in.) spacing, two pairs at 320 mm (12.6 in.) spacing and one pair at 360 mm (14.2 in.) spacing. Each of the probes can act as either receiver or transmitter with a typical operation ultrasonic frequency of the 50 kHz. The device records shear-wave impulse time-histories from 45 transmitting and receiving transducer pairs in each measurement. Figure 25 shows one of the 45 impulse time-history pairs from an example measurement. Figure 26 shows a schematic that would cause this type of impulse response. Various versions of this ultrasonic linear array technology have a default calibration mode as well as reconstruction tools (Botolina et al., 2012; Shi et al., 2009; Bishko, 2008; Mayer et al., 2008; Nesvijski, 2000; Nesvijski, 2003; Sokolov, 2003). However, analysis methods presented in this study use the raw 45 sending and receiving impulse time histories, $\Psi_{e,r}(t)$.

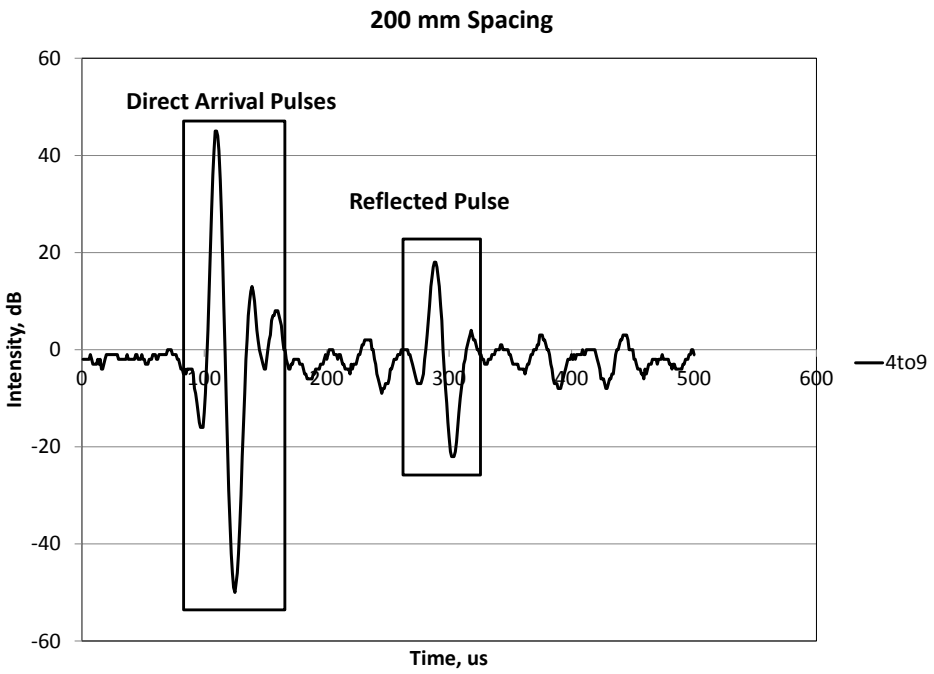

Figure 25: Example impulse time history from a transducer pair, Ψ_4, 9 (t) from emitting channel 4 to receiving channel 9 (200 mm spacing).

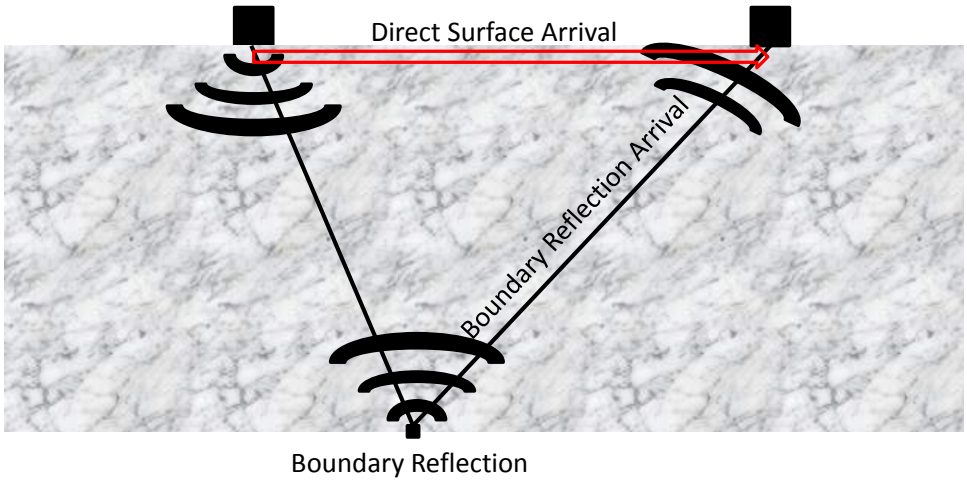

Figure 26: Schematic of direct and reflection arrivals.

This device can be used for various nondestructive subsurface diagnostic applications including dowel and tie bar misalignment (Hoegh et al., 2011), poor consolidation and non-uniformity (Hoegh et al., 2012a), de-bonding between layers (Hoegh et al., 2012c), horizontal delamination (Hoegh et al. 2012b; Hoegh et al., 2013), pavement thickness (Vancura et al., 2013), and joint deterioration and spalling or poor consolidation around dowels (Hoegh et al. 2012c; Hoegh et al., 2013). In addition to providing ultrasonic reflection information, the direct arrival of the multiple channels provides the UPV information as well. Figure 27 shows the results of beam and slab measured velocities at various concrete ages for the same concrete mix. It can be

observed that there is a very good agreement between the beam and slab velocities at various early ages. The monotonic relationship is positively correlated with concrete age. This along with maturity measurements should provide extremely accurate, while practical, estimate of concrete properties.

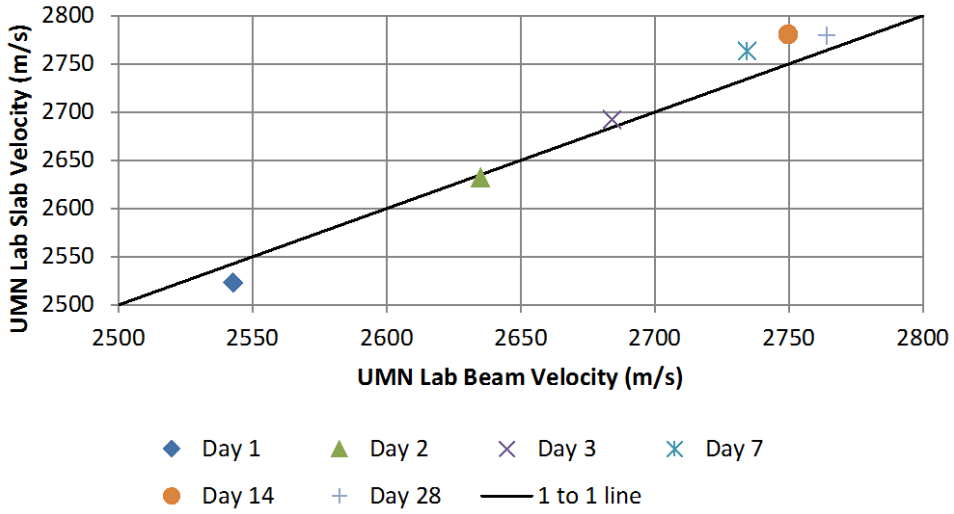

Figure 27: Ultrasonic Array measured shear wave velocities for concrete beams vs. slabs at various concrete ages.

Chapter 3: Laboratory Testing

Four total rounds of laboratory tests were performed. The first was performed in April of 2014 involving air curing of the beams and loading to 80% of day 1 strength. The second round of testing was performed in July of 2014 and was identical to the first round with the exception of curing conditions. The beams for the second round of testing were wet cured in a curing tank. The third round of testing was performed in August of 2014. This round of testing involved the same wet curing method used for round two but the beams were loaded to 80% of the strength reached on the day of loading rather than 80% of day 1 strength. The round three loading protocol accounted for the strength gain. The fourth round of testing was conducted in March of 2015 and involved the use of cyclic loading to 65-80% of the strength of that particular day. A curing compound was utilized rather than air or wet curing. MIRA readings were taken for all four rounds, maturity sensors were used for the first two rounds, and P-wave velocity measurements were obtained for the fourth round of testing. Table 6 summarizes the four rounds of testing.

Table 6: Summary of laboratory trials.

Round	Date	Number of Specimens	Curing Condition	Loading Protocol
1	4/1/14	20 beams, 30 cylinders*	Air Curing	Beams were loaded to 80% of the average Day 1 strength- 3400 lbs
2	7/14/14	22 beams, 1 cylinder**	Water Curing	Beams were loaded to 80% of the average Day 1 strength- 2700 lbs
3	8/25/14	25 beams	Water Curing	Beams were loaded to 80% of the strength on loading day- loading value increased each day
4	3/2/15	12 beams	Curing Compound	Beams were loaded to 65-80% of the strength on loading day via cyclic loading- loading value increased each day

* Cylinder results were inconclusive, focus was on beams for the remainder of the project
** One cylinder was poured in order to embed the maturity sensor, no testing was done on this specimen

3.1 General Lab Procedures

3.1.1 Lab Processes

3.1.1.1 MIRA Reading Process

Two calibration readings were taken on the top surface of each beam. In scan mode, the top surface of each beam was again scanned and this was repeated a second time. The beams were then rotated so the left side was facing up, and the process was repeated. This was repeated again for the right and bottom side facing up.

3.1.1.2 Beam Testing Process

Support locations were marked on the beams 6” between each top support and 18” between the bottom supports. The beam was positioned in the machine so that the numbered end of the beam was facing towards the front of the machine. The two sides that come into contact with the loading supports were clean sides of the beam, not the finished side. A loading rate of 30-50 lb/s was used for the load control rounds (Rounds 1-3) while a rate of 0.01 microns/second was utilized for the last round of testing which utilized a displacement controlled machine. This displacement rate yielded a load rate of approximately 30-50 lbs/sec. A displacement-controlled

testing device was used for the last round because of the need to utilize cyclic loads for long durations. This loading scenario was not possible with the original testing machine and therefore a different machine needed to be used which was able to run overnight with a computer controlling the load continuously.

3.2 Round 1 Testing- Air Cured Samples

On April 1st, 2014, 30 cylinders and 20 beams were poured beginning at 10AM using concrete provided by a ready-mix company in the MSP metro area in accordance with the mix design outlined in Table 7. A slump test following ASTM C143 was performed, as well as air content measurements according to ASTM C231. The cylinders and beams were both poured in accordance with ASTM standard C192. After the pour was completed, the specimens were covered with plastic and left to air cure. Table 8 below summarizes the loading protocol that was followed. The cylinders followed a similar loading plan, but the results were inconclusive. As a result, future rounds of testing only involved the loading of beams.

Table 7: Concrete Mix Design

Mix	Quantity
Cement (Type I)	450 lbs/cubic yard
Fly Ash (Class C)	80 lbs/cubic yard
Water	244 lbs/cubic yard
Air	5.5%
Fine Aggregate (pit run sand)	1200 lbs/cubic yard
Coarse Aggregate 25-50mm (crushed limestone)	1140 lbs/cubic yard
Coarse Aggregate 6mm-25mm (crushed limestone)	756 lbs/cubic yard

Table 8: Round 1 loading summary.

Beam	Day 1	Day 2	Day 3	Day 7	Day 28
101*	Load to 80% of 119 Strength				
102		Load to 80% of 119	Load to 80% of 119	Load to 80% of 119	**Break**
103*					
104		Load to 80% of 119 Strength	Load to 80% of 119 Strength	Load to 80% of 119 Strength	**Break to Determine 28 Day Strength**
105					
106					
107					
108					
109					
110					
111					
112					
113					
114					
115					
116	Extra Beam				
117	Extra Beam				
118	Load to 80% of 119	Load to 80% of 119	Load to 80% of 119	Load to 80% of 119	**Break**
119	**Break to Determine Day 1 Strength**				
120	Extra Beam with Maturity Sensor				

* Beams 101 and 103 broke due to machine error. Beam 118 was the replacement

3.2.1 Results

Figure 28 shows the break strength of beams which were loaded for the first time on varying days. The results showed a reduction in break strength in beams which were previously loaded before Day 28.

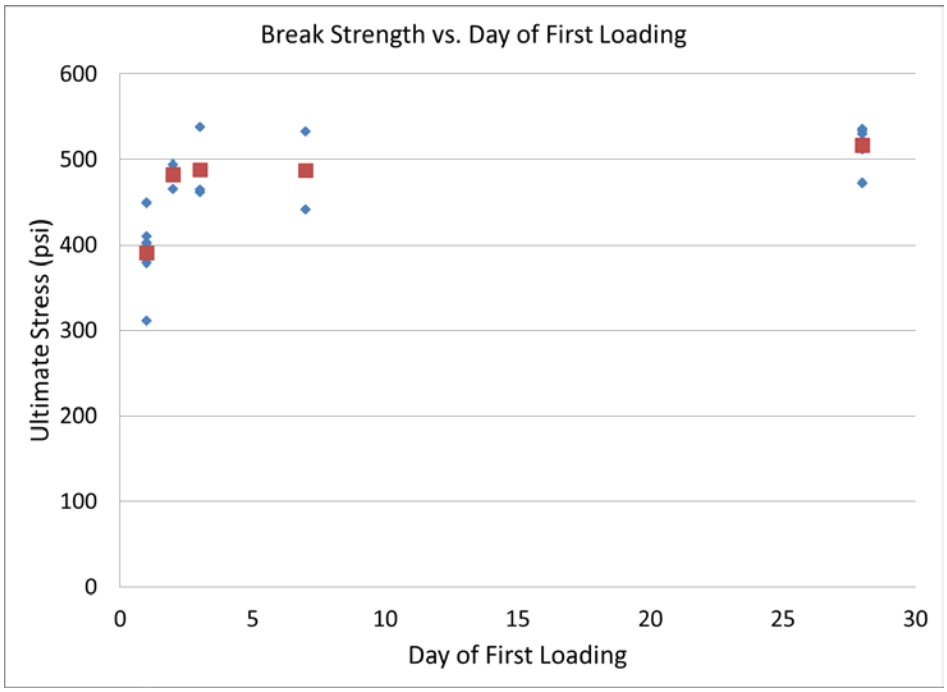

Figure 28: Flexural Strength versus first day of load application.

Figure 29 shows the decrease in ultimate strength vs. the day of first loading. It can be observed that the beams loaded on day 1 exhibited the largest drop in strength, and those loaded at 2, 3, and 7 days showed a slight drop in strength versus the 28 day strength. Those loaded at 2, 3, and 7 days all exhibited about a 5% reduction in strength which appears to indicate that after day 2 there was no further drastic reduction in strength.

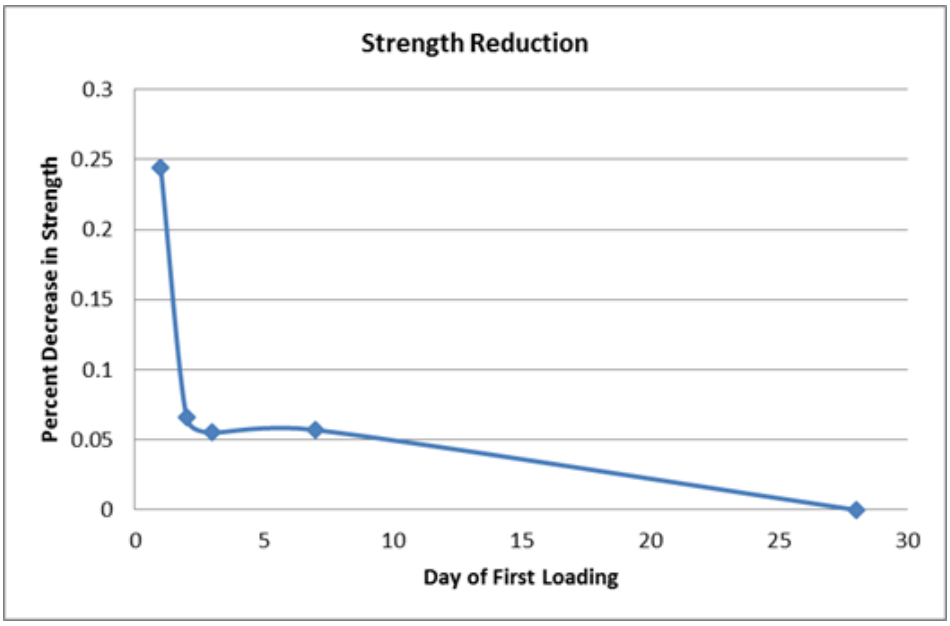

Figure 29: Percent decrease in flexural strength versus first day of loading.

The strength reduction at the time of first loading versus maturity and velocity can be observed in Figures 30 and 31, respectively. Figure 30 also shows the strength gain with respect to maturity. It can be observed that the strength reduction trends corresponded to the maturity and velocity trends.

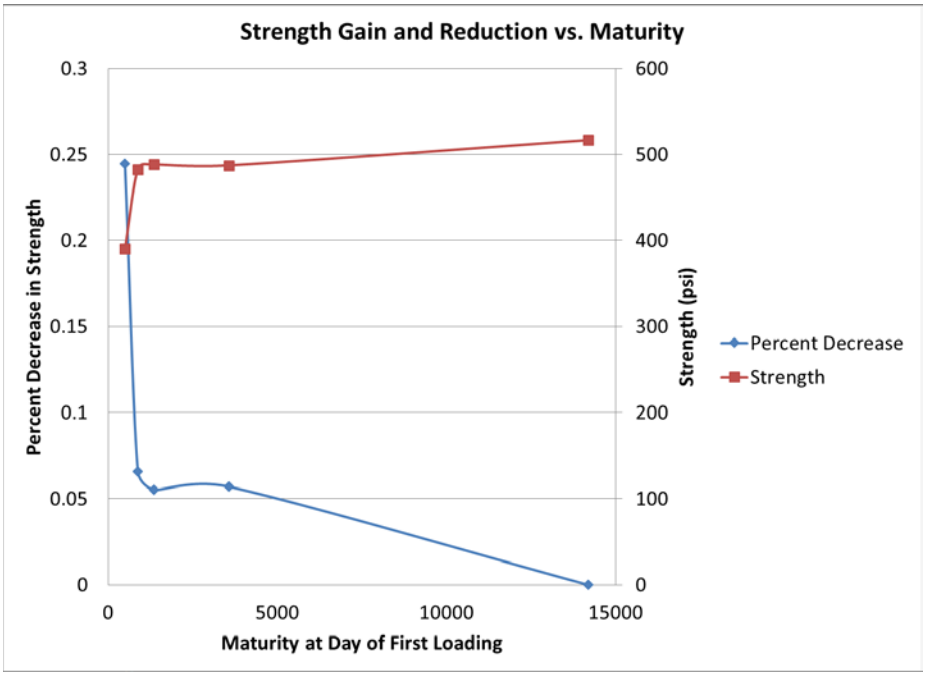

Figure 30: Percentage decrease in strength versus maturity.

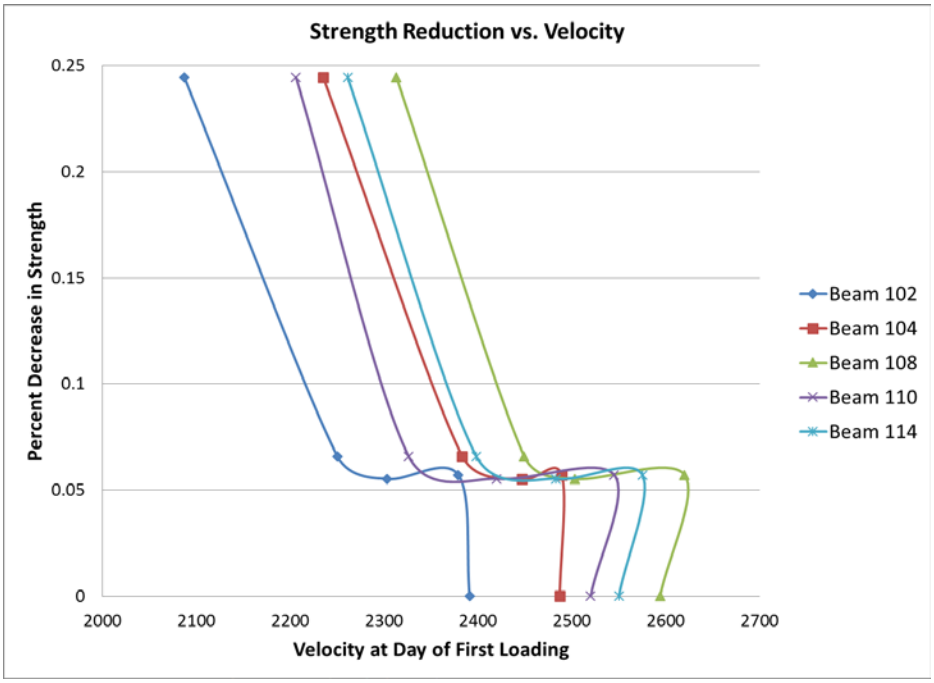

Figure 31: Percentage decrease in strength versus velocity.

Figure 32 shows preliminary shear wave velocities observed on the bottom surface of the beams, acquired via the use of MIRA. It can be observed that there is velocity variation from beam to beam. Analysis of the beam to beam changes at various days of testing show that these trends seem to be a function of the initial conditions (e.g. a larger velocity at day 1 corresponds to a larger velocity in subsequent days and vice versa). Four important conclusions can be drawn from this trend:

1. Workmanship of the beam preparation affects beam quality
2. The initial curing conditions within the first 24 hours are critical
3. Use of velocity soon after construction has a potential to detect relative adverse curing conditions early in a project
4. It is important to evaluate changes in velocity versus the initial measurement rather than making absolute comparisons to isolate the effect of loading or other factors occurring after 24 hours.

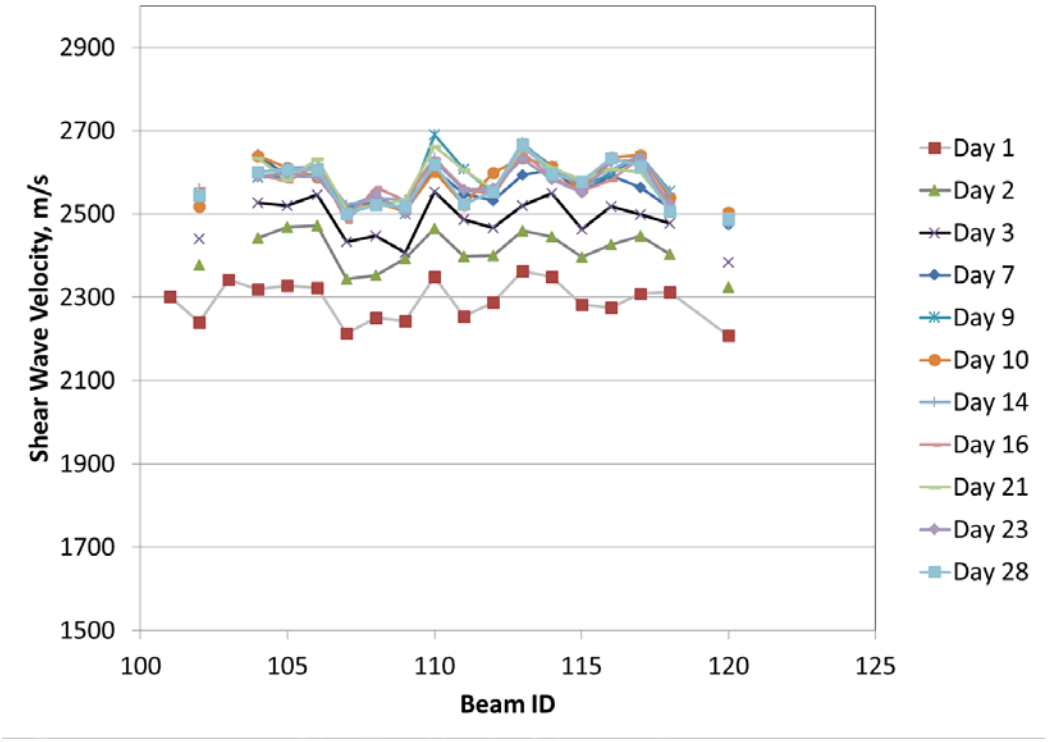

Figure 32: Velocity variation from beam to beam at various ages.

Figure 33 shows the maturity versus time plot for the four specimens with embedded sensors. As can be seen, the results from the four sensors were very similar in both trend and magnitude.

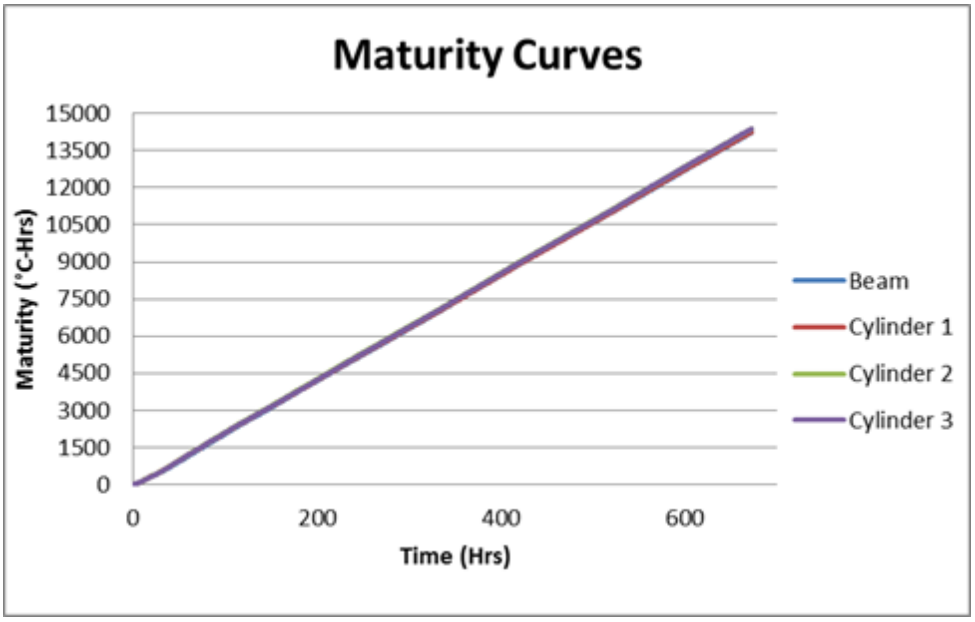

Figure 33: Maturity versus time.

Maturity and shear wave velocity trends have also been analyzed. Figure 34 shows the correlation between maturity and shear wave velocity for a representative sample of beams.

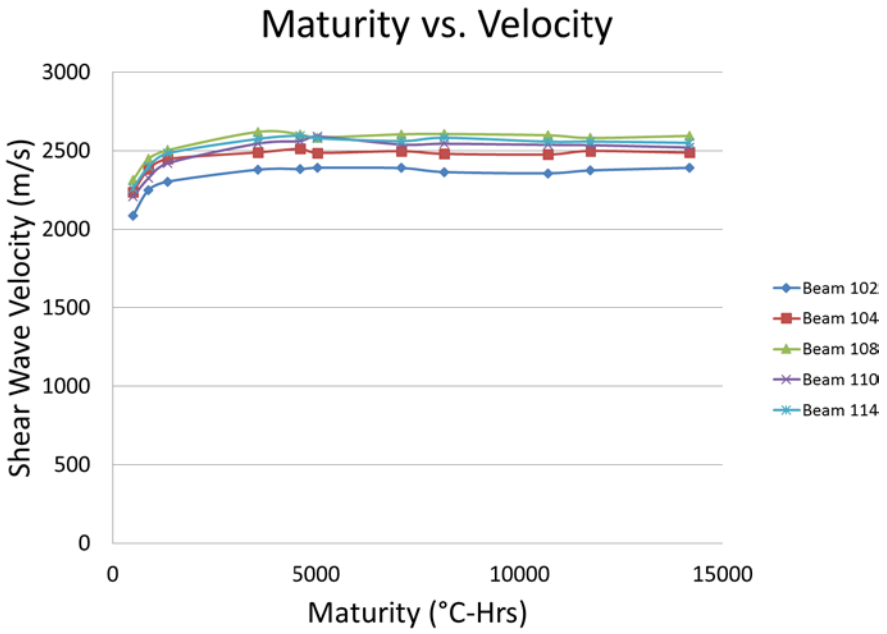

Figure 34: Velocity versus maturity.

Figure 35 shows the maturity versus velocity at days 1, 2, 3, 7, and 28. It can be observed that the velocity was more sensitive to the early changes in hydration.

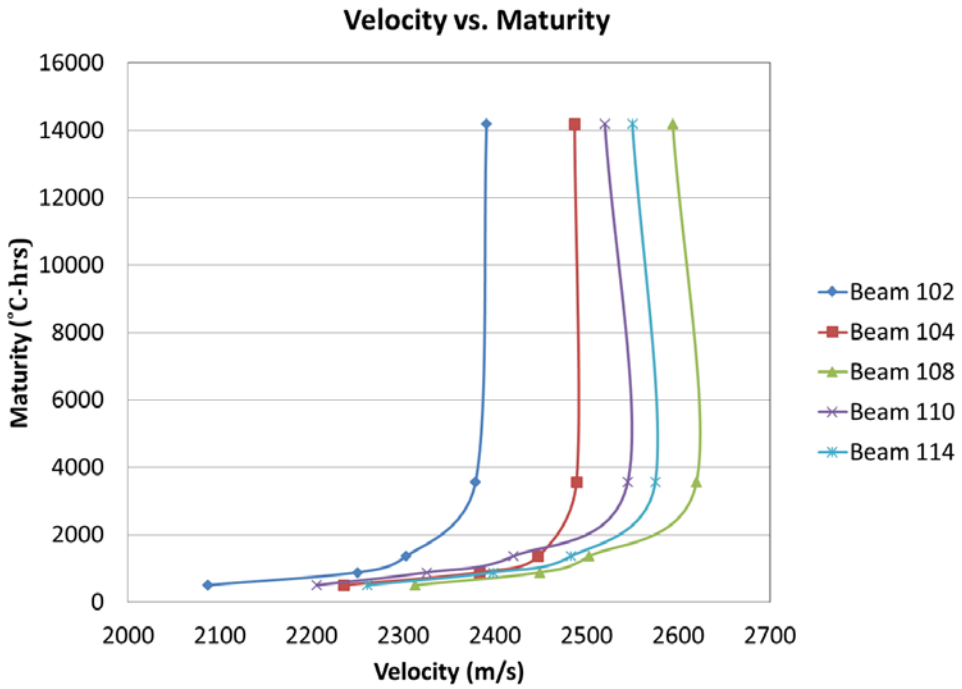

Figure 35: Maturity versus velocity at days 1, 2, 3, 7, and 28 from the first round of testing.

3.3 Round 2 Testing – Water Cured Samples

3.3.1 Testing Outline

On July 14th, 2014, 22 beams and 1 cylinder were poured beginning at 10AM using concrete provided by a ready-mix company in the MSP metro area. A slump test following ASTM C143 was performed, as well as air content measurements according to ASTM C231. The cylinders and beams were both poured in accordance with ASTM standard C192. After the pour was completed, the specimens were covered with plastic and left on-site for the night. At 8AM on July 15th, the beams were all removed from their molds and taken to the lab. Table 9 below summarizes the loading protocol that was followed. The beams were placed in a curing tank once the loading and MIRA measurements for Day 1 were completed. For all subsequent days of testing, the beams were removed from the tank one hour prior to testing and re-submerged after testing was complete.

Table 9: Round 2 loading summary.

Beam	Day 1	Day 2	Day 3	Day 7	Day 28
201	Load to 80% of 220-222 Avg. Strength	Load to 80% of 220-222 Average Strength	Load to 80% of 220-222 Average Strength	Load to 80% of 220-222 Average Strength	Break for 28 Day Strength
202					
203					
204					
205					
206					
207					
208					
209					
210					
211					
212					
213					
214					
215					
216				Break to Determine Day 7 Strength	
217					
218		Break to Determine Day 2 Strength			
219					
220	Break to Determine Day 1 Strength				
221					
222					

3.3.2 Results

Figure 36 shows the break strength of beams which were loaded for the first time on varying days. The flexural strength did not show any significant change due to early loading as can be observed by the figure. This suggests that the reduction in strength from early loading observed in the first round is not always observed, and is presumably a function of the conditions during placement and the curing process.

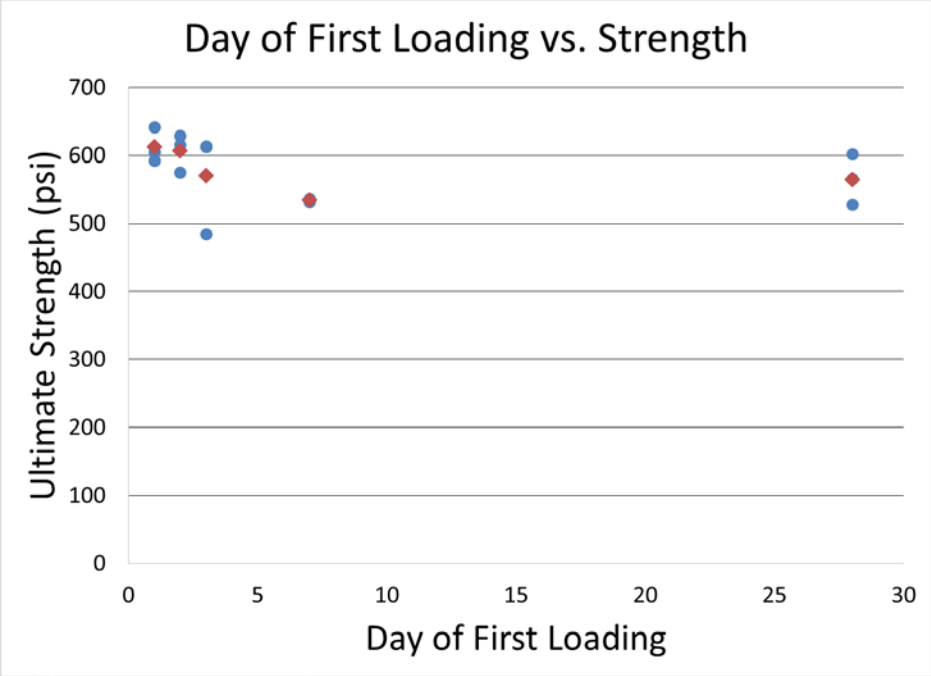

Figure 36: Flexural Strength versus first day of load application.

Figure 37 shows the trend between shear wave velocity and strength. A best fit line shows that there is a positive correlation between shear wave velocity measured with MIRA and strength, as was previously thought to be the case. This shows that shear wave velocity is a good indicator of current strength conditions of concrete.

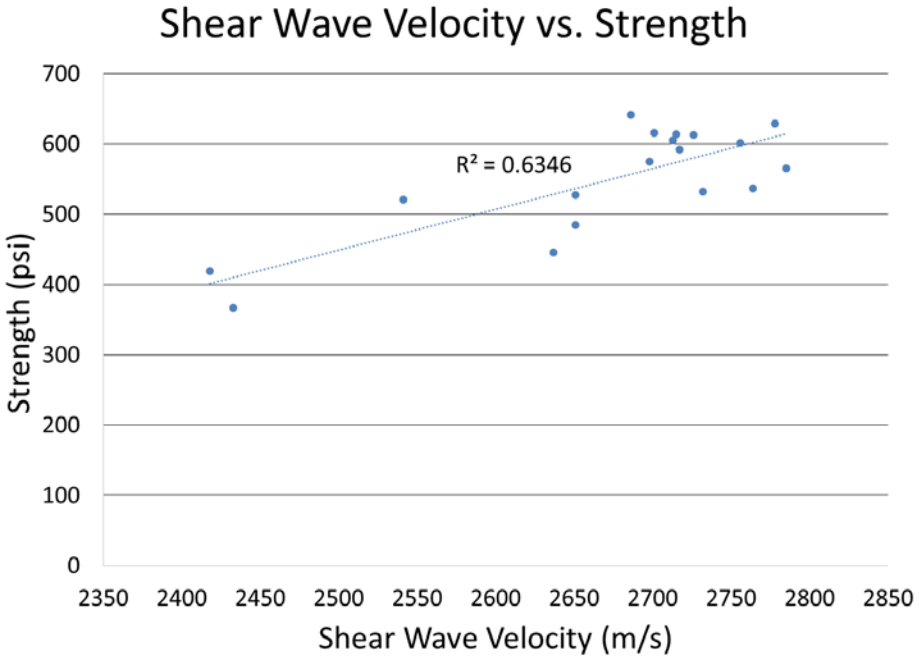

Figure 37: Shear wave velocity versus Flexural Strength.

Figure 38 shows the resulting curves for shear wave velocity and ultimate strength development over the course of 28 days. As can be seen, the two curves have a similar shape and trend and strengthen the theory that shear wave velocity is a good indirect indicator of strength. Figure 39 shows the shear wave velocity measurements for each beam throughout the first 21 days. Similar trends from Round 1 of testing can be seen in that the shear wave velocity seems to level off at about day 7.

This round of testing did not confirm trends seen in Round 1 when air curing was utilized. One possible explanation for this behavior is due to the strength gain that results from water curing. Because water cured samples have a higher strength as time goes on, the beam loading protocol that was utilized in Round 2 may not have been sufficient to create appropriate damage levels. A subsequent round of testing was deemed necessary in order to answer these questions.

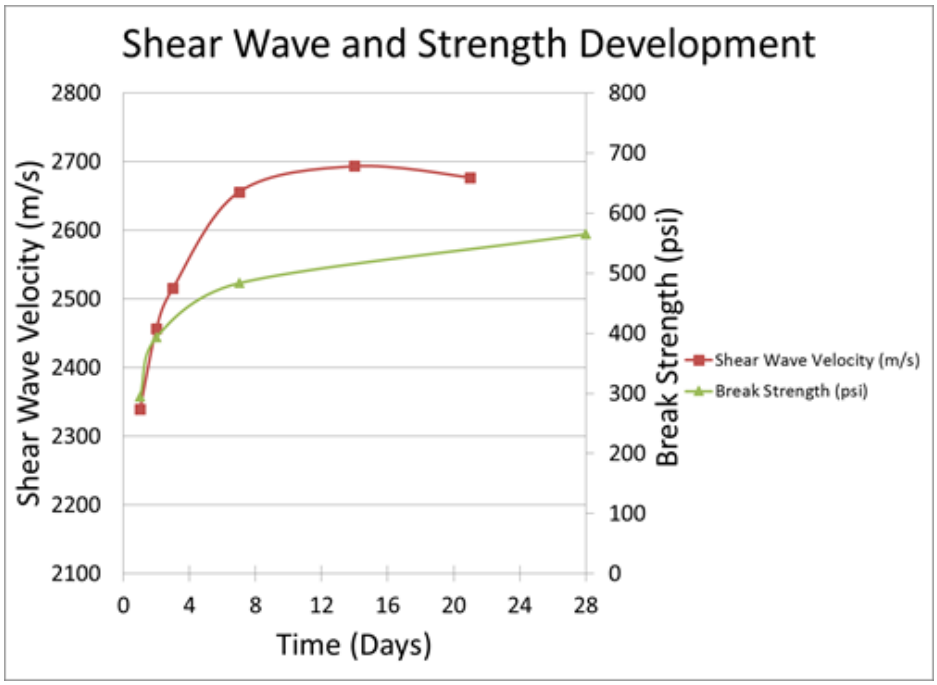

Figure 38: Shear wave velocity and flexural break strength over time.

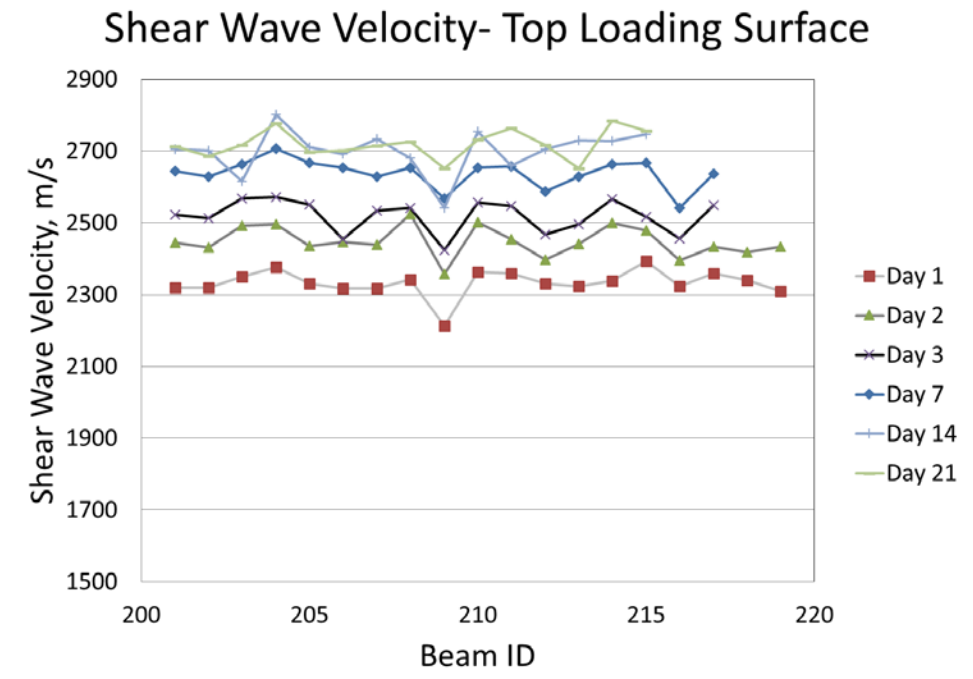

Figure 39: Velocity variation from beam to beam at various ages.

3.4 Round 3 Testing – Water Cured Samples (Repeated)

3.4.1 Testing Outline

On August 25th, 25 beams were poured beginning at 10AM using concrete provided by the same MSP metro area company and poured on-site. A slump test following ASTM C143 was performed, as well as air content measurements according to ASTM C231. The cylinders and beams were both poured in accordance with ASTM standard C192. After the pour was completed, the specimens were covered with plastic and left on-site for the night. At 8AM on August 26th, the beams were all removed from their molds and taken to the lab. The beams were placed in a curing tank once the loading and MIRA measurements for Day 1 were completed. For all subsequent days of testing, the beams were removed from the tank one hour prior to testing and re-submerged after testing was complete. The main difference in variables for this round of testing is the increase in load before 28 days. In the first two rounds of testing, the beams were loaded to 80% of the Day 1 strength. For this round, the beams are loaded to 80% of that day's strength. The loading scheme that was followed for this round of testing can be found in Table 10 below.

Table 10: Round 3 loading summary.

Beam	Day 1	Day 2	Day 3	Day 7	Day 28
301	Load to 80% of 323-325 Avg. Strength	Load to 80% of 320-322 Avg. Strength	Load to 80% of 318-319 Avg. Strength	Load to 80% of 316-317 Avg. Strength	**Break for 28 Day Strength**
302					
303					
304					
305					
306					
307					
308					
309					
310					
311					
312					
313					
314					
315					
316				Break to Determine Day 7 Strength	
317					
318			Break to Determine Day 3 Strength		
319					
320		Break to Determine Day 2 Strength			
321					
322					
323	Break to Determine Day 1 Strength				
324					
325					

3.4.2 Results

Figure 40 shows the break strengths of the beams with respect to the day that they were first loaded. There does not appear to be a strong trend with this data, indicating that the early loading did not seem to have an effect on the ultimate strength of the beams.

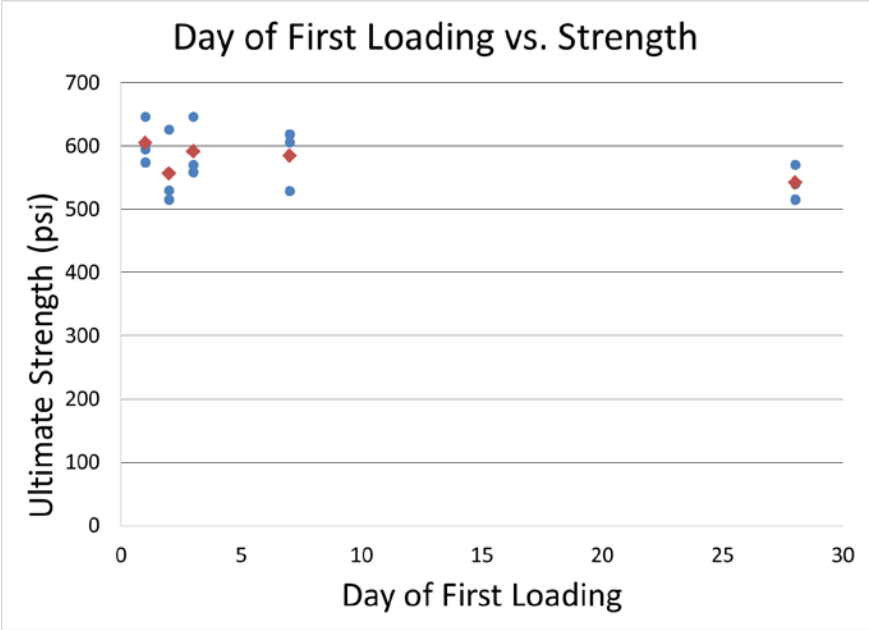

Figure 40: Break strength at day of first loading.

Figure 41 shows the strength of each beam with respect to the shear wave velocity on the day of the break. This round shows an even stronger correlation between these characteristics. Figure 42 shows the relationship between shear wave velocity and strength gain over time. This round of testing again showed a stronger similarity in shape and trend to the previous round. These two figures show that there is a relationship between shear wave velocity and strength gain, be it an indirect correlation.

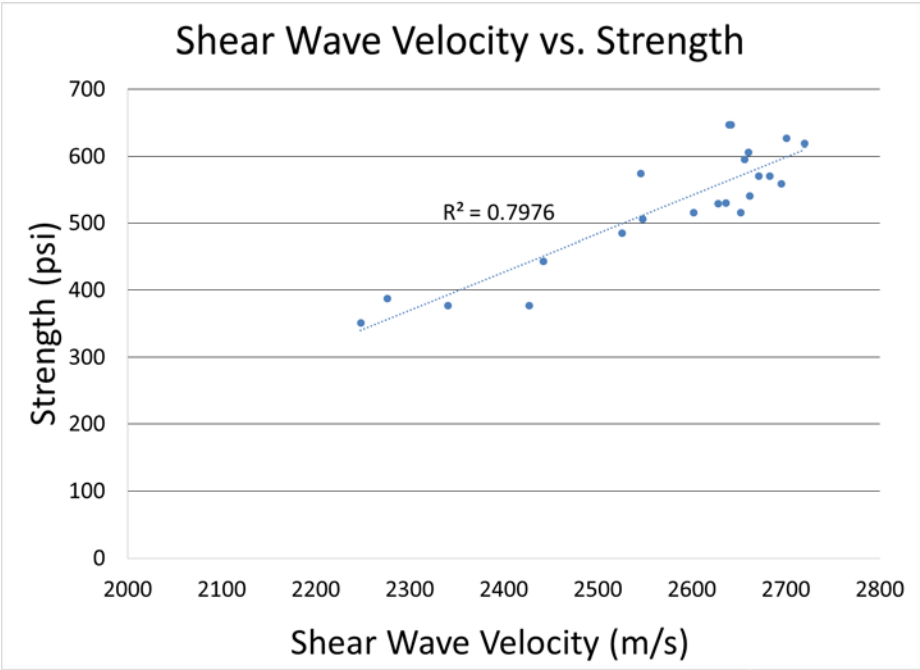

Figure 41: Shear wave velocity versus Flexural Strength.

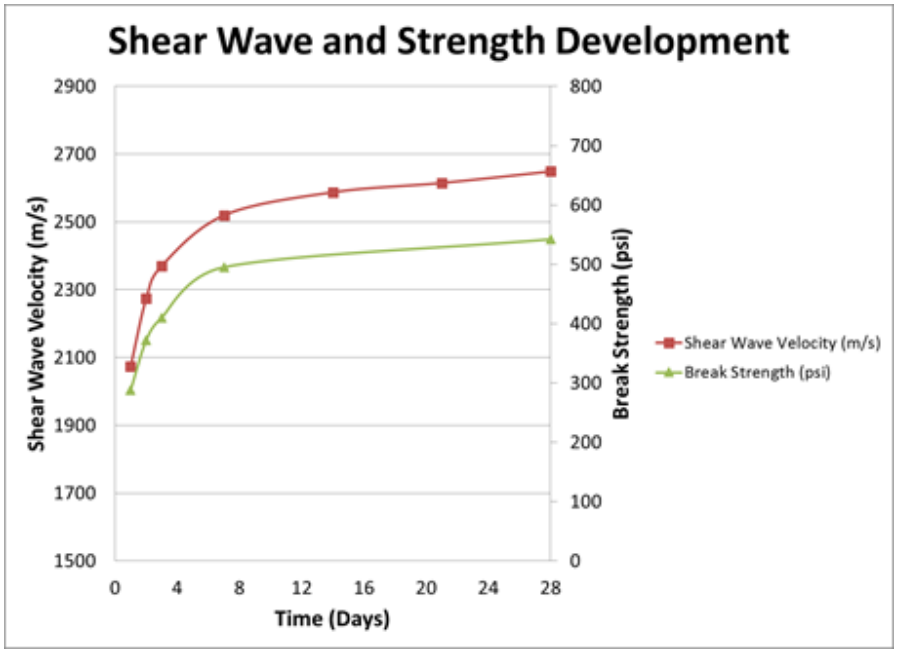

Figure 42: Shear wave velocity and flexural break strength over time.

Figure 43 shows the shear wave velocity variation for all the beams throughout the first 28 days. The same trends and characteristics for this graph from previous rounds were again seen. Shear wave velocity seems to level off after day 7, and beams with lower initial shear wave velocities continued to have lower relative shear wave velocities as time went on.

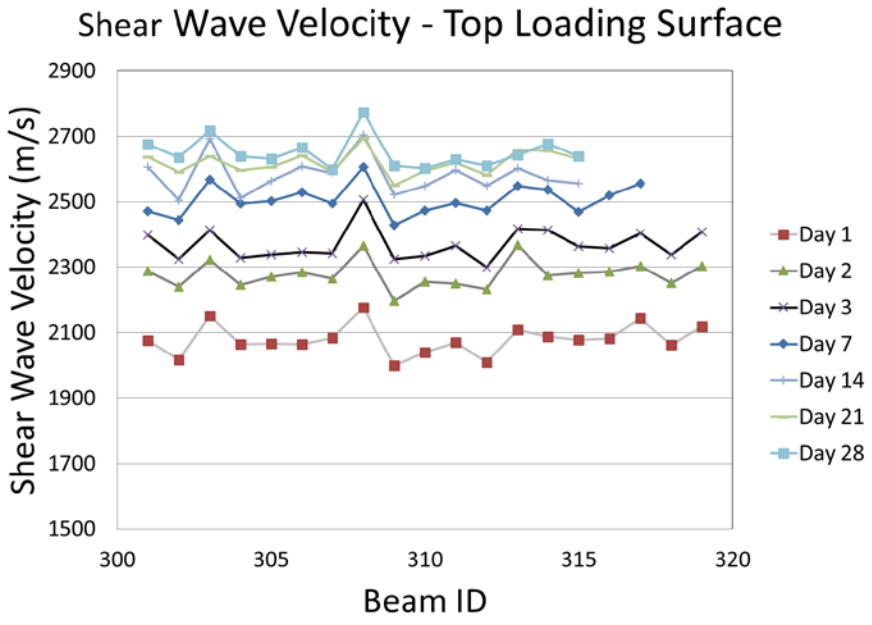

Figure 43: Velocity variation from beam to beam at various ages.

3.5 Round 4 Testing – Curing Compound Samples

3.5.1 Testing Outline

On March 2nd, 2015, 12 beams were poured beginning at noon using concrete provided by the same MSP metro area provider as utilized previously. A slump test following ASTM C143 was performed, as well as air content measurements according to ASTM C231. The cylinders and beams were both poured in accordance with ASTM standard C192. After the pour was completed, the specimens were sprayed with curing compound. At 9AM on March 3rd, the beams were all removed from their molds and the remaining sides were coated with curing compound. The beams were loaded according to the protocol outlined in Table 11. This round of testing was different from previous rounds in that a curing compound was utilized, and rather than static loading, cyclic loading was utilized. Additionally, P-wave measurements were taken whenever MIRA readings were taken in an effort to compare the results and applicability of these nondestructive technologies.

Table 11: Round 4 loading summary.

Beam	Day 1	Day 2	Day 3	Day 4	Day 7	Day 8	Day 14
401	Cylic Load 65-80% of 407						
402		Cylic Load 65-80% of 408					Break for 14 Day Strength
403			Cylic Load 65-80% of 409				
404					Cylic Load 65-80% of 410		
405				Cylic Load 65-80% of 409			
406							
407	Break						
408		Break					
409			Break				
410					Break		
411							Break
412	Cyclic Tester Beam						

3.5.2 Results

Figure 44 shows the 14 day flexure break results with respect to the day of first loading. It can be observed that the effect of loading time on break strength is not significant at the load levels applied in this round of testing.

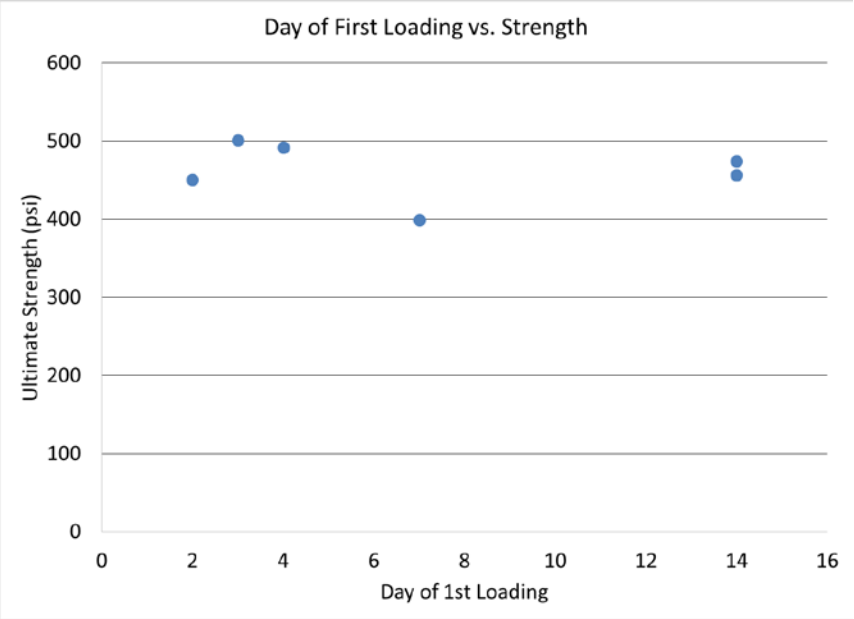

Figure 44: Flexural Strength versus day of first loading.

Figure 45 shows the shear wave velocity development of each beam over the first 14 days. These results confirm those seen in earlier rounds in that there is great change in shear wave velocity at early ages. In previous rounds, shear wave velocity was not measured on day 4. With the addition of that data set, the results seem to indicate that the shear wave velocity begins to level off prior to day 7, but after day 3.

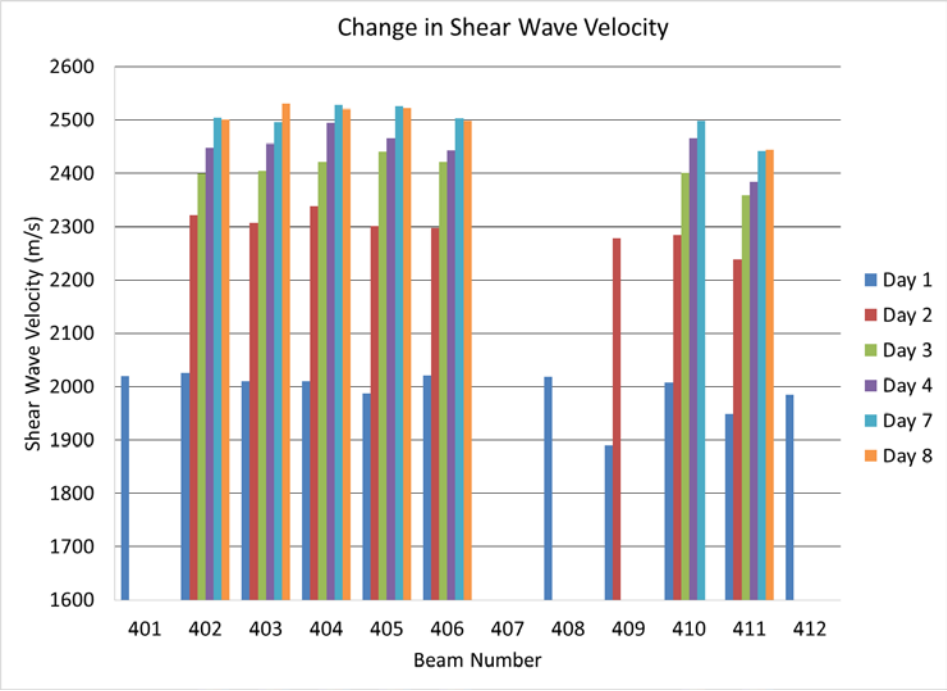

Figure 45: Velocity variation for all beams at various ages.

Figure 46 shows the shear wave velocity normalized by day 1 velocity over time for the loaded and control beams. The relative velocity agrees with the ultimate strength in that, the loading time does not affect the results at the load levels applied in this round of testing.

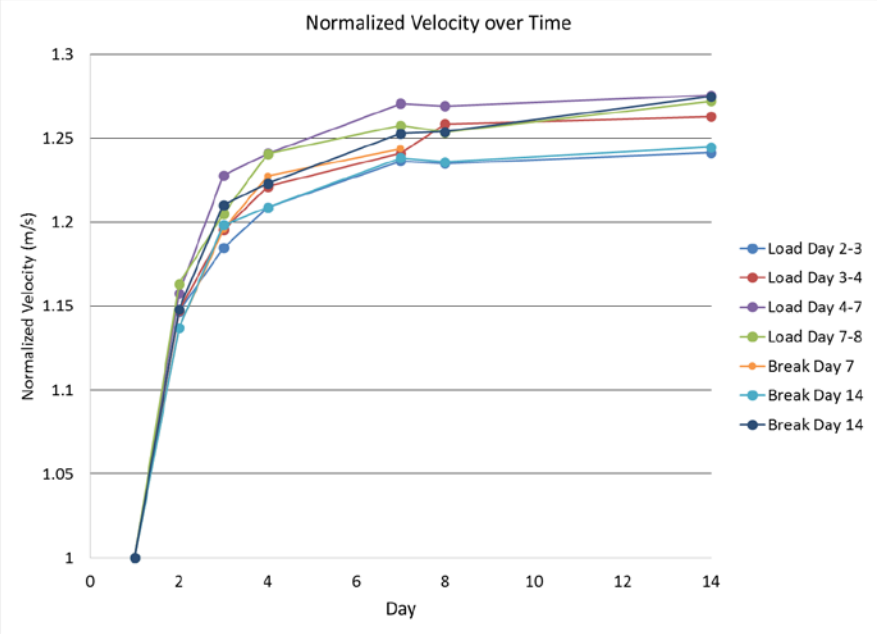

Figure 46 Normalized shear wave velocity over time for control and loaded beams.

Figure 47 shows the correlation between shear wave velocity at the day of break and the ultimate break strength on day 14. Again, a positive correlation is seen between these two values and show the possible relationship between shear wave velocity and ultimate strength.

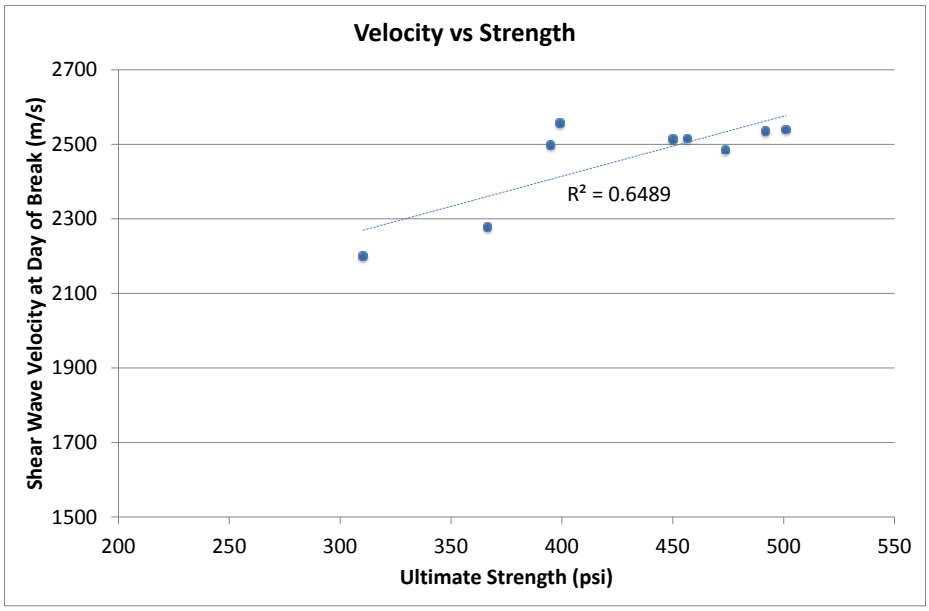

Figure 47: Shear wave velocity versus ultimate flexural strength.

Figure 48 shows the P-wave velocity measurements obtained, using the UK1401 device shown in Figure 20, for each beam at various ages. It can be seen that the results are not as conclusive as the shear wave velocity relationships. While general trends remain, there are outliers present. For example, for Beam 406 the day 14 velocity is lower than all the previous days. This shows that the P-wave velocity technique may be a cheaper alternative for applications where accuracy is not as important. For example, this device may be useful in situations where it is suspected that some locations may experience extreme levels of variation from the designed strength, where a higher variability method such as the UK1401 will be able to make an initial detection at a lower cost than the array system.

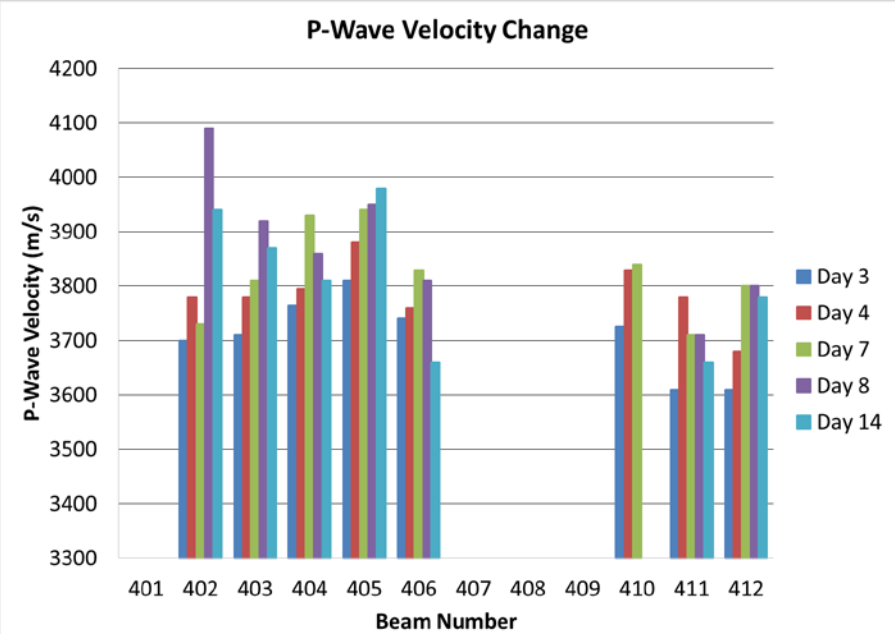

Figure 48: P-wave velocity variation for various ages.

3.6 Conclusions

By changing various aspects of the testing protocol in subsequent rounds of testing, the effects of variables such as curing and loading duration were investigated. The results of all four rounds of strength testing is shown in Figure 49. In the first round of testing, beams that were loaded at early ages had lower ultimate strengths than those that were never loaded, especially when loaded at day 1. The second round of testing followed the same loading protocols as round 1, but water curing was utilized. The results for round 2 were inconclusive. The source of this was thought to be the strength gain caused by water curing. The load levels were remaining the same, while the strength was increasing more rapidly than in the air curing case, resulting in the beams being loaded to less than the 80% goal. To remedy this issue, a third round of testing involved breaking beams throughout the loading process and subsequently adjusting the load levels to reflect 80% of the current strength. Again, the results were inconclusive. In an effort to more properly reflect the loading undergone by pavement due to traffic, cyclic loading was implemented for the final round. The results were inconclusive and showed that loading at an early age had no significant effect on ultimate strength. Regardless of curing conditions, shear wave velocity increased in a similar shape and trend as strength gain. The results from all rounds of testing show that shear wave velocity is a good indirect indicator of strength. The inherent variability of the flexure beam tests proved to make it difficult to uncover trends and detect correlations when ultimate strength results were examined. The laboratory study provided a wealth of information regarding the relationship between flexural strength, elastic parameters, and shear wave velocity, which are critical to developing a performance based mechanistic criteria. The laboratory study also does not quantify the effect of the damage on pavement performance.

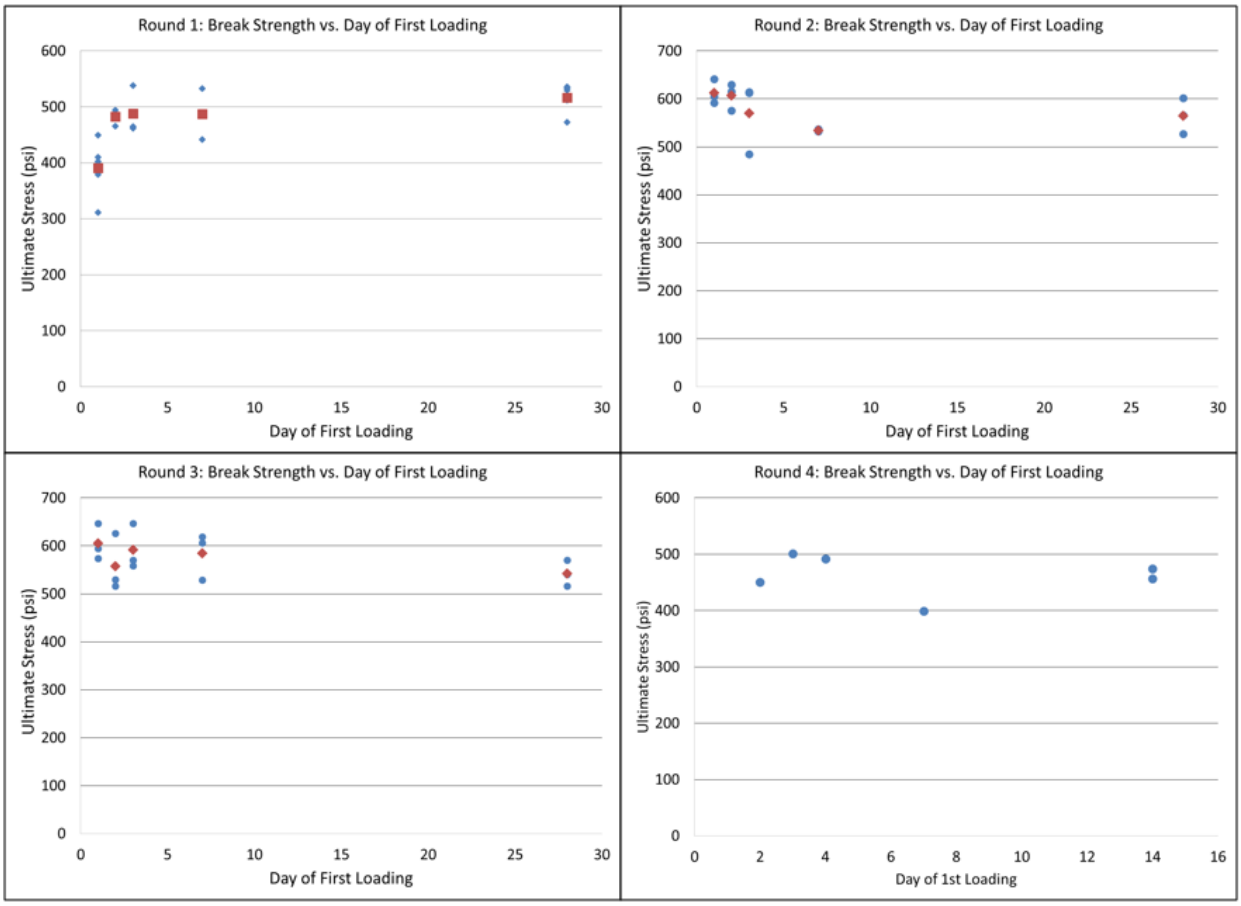

Figure 49: Ultimate strength vs. day of first loading for all four rounds of testing.

Chapter 4: Field testing

In this task, field trials were conducted to verify that the measures from the laboratory tests could be implemented in a full scale field environment. In this case, the measures calibrated in the laboratory testing rounds described in Task 2, developed through comparisons of maturity and velocity with strength development under different loading conditions, can be extrapolated to evaluate strength gain in newly constructed pavements. Since shear wave velocity was the primary measure sensitive to early strength gain in the laboratory, it was implemented on several field trials described below.

4.1 October 2013 Testing

Field tests on I-35 Northbound between County Road 2 and 70 were conducted on October 10th, and 17th, 2013 to gather initial measurements and evaluate the testing protocol for field velocity data collection on a newly constructed pavement. The mix design for this pavement is shown below in Table 12.

Table 12: October Field Testing Mix Design

Mix	Quantity
Cement (Type I)	400 lbs/cubic yard
W/CM Ratio	0.36
Fly Ash (Class C)	130 lbs/cubic yard
Water	193 lbs/cubic yard
Air	7.0%
Fine Aggregate (sand)	1359 lbs/cubic yard
Coarse Aggregate (2″-)	675 lbs/cubic yard
Coarse Aggregate (3/4″-)	1158 lbs/cubic yard

4.1.1 October 10, 2013

Pavement information was gathered for the sections of roadway to be tested using ultrasound linear array equipment (MIRA). The segment of roadway between stations 321+46 and 355+58 was poured on Tuesday, October 8, 2013 (2 days old at time of testing). Pavement stretching from 355+58 to 402+62 was poured on Wednesday, October 9, 2013 (1 day old at time of testing). Testing and calibration began at 389+00. Measurements were first taken walking towards the south at the center of the truck lane slab. Information was gathered twice at each location, with 5 slabs of spacing between consecutive tests. After every 10 measurements (unless otherwise noted), the system was calibrated. The same length of roadway was then tested on the passing lane slab, heading north. For this set of measurements, the system was calibrated roughly every 10 slab lengths and no intermediate measurements were taken.

4.1.2 October 17, 2013

Pavement information was gathered for the sections of roadway to be tested using MIRA, wave reflection equipment. The segment of roadway between stations 321+60 and 355+58 was poured on Tuesday, October 8, 2013 (9 days old at time of testing). Pavement stretching from 355+58 to 402+62 was poured on Wednesday, October 9, 2013 (8 days old at time of testing). The stretch of pavement from 402+62 to 468+00 was around 6-7 days old at time of testing. Testing and calibration began at station 321+60. Measurements were taken walking towards the north at the center of the truck lane slab. Information was gathered twice at each location, with 50 feet between consecutive tests. After every 10 measurements (unless otherwise noted), the system was calibrated. This amount of calibration hurt the productivity, so the research team developed a method to measure velocity in "scan" mode rather than "calibration" mode to reduce this need for a large amount of calibration.

Table 13 below shows the age of pavement with respect to stationing. Figures 50 and 51 show the shear wave velocity results versus stationing and days after it was paved, respectively. It can be observed from Figure 50 that there is variation in velocity depending on the location, even for the same day of paving. This similar trend was observed in the truck and passing lanes of the same stationing for days 2 and 3 shows that this variation corresponds to physical changes in the curing conditions. It can be observed from Figure 51 that the velocity increases as the concrete ages in a similar trend that was observed in the laboratory.

Table 13: Pavement Stationing and Age Information

Stationing	Pour Date	Age on October 10th	Age on October 17th
321+46 to 355+58	10/8/2013	2 days	9 days
355+58 to 402+62	10/9/2013	1 day	8 days
402+62 to 468+00	10/10-10/11/2013	N/A	6/7 days

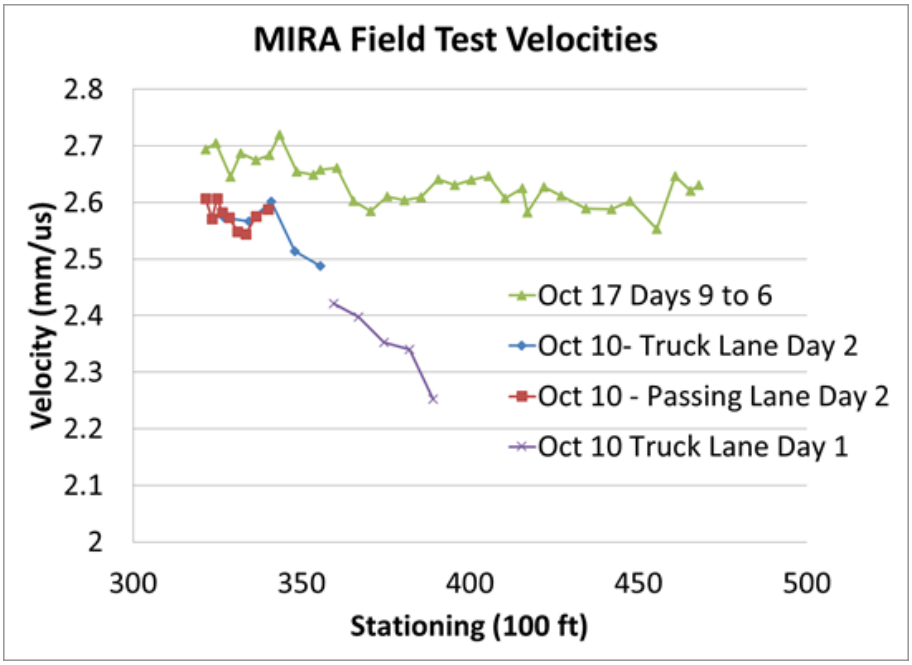

Figure 50: Shear Wave Velocity versus stationing for various days after paving and locations within the same project.

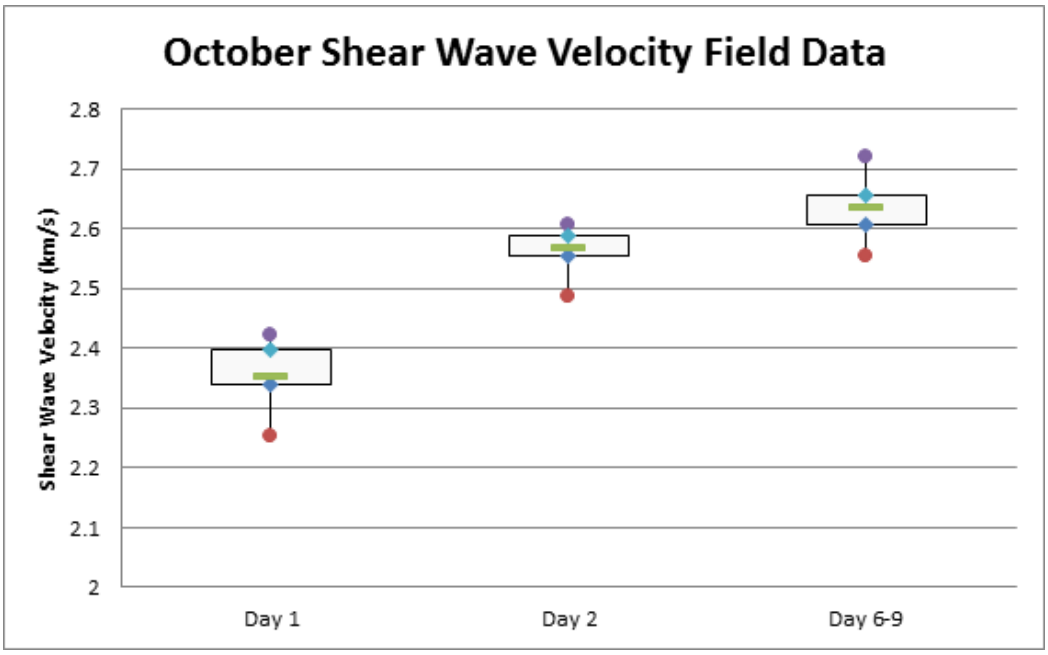

Figure 51: Velocity versus days after paving.

The results shown above were from calibration mode velocity measurements from the general purpose MIRA software. These calibration results are accurate, and as the preliminary plots show, useful for identifying trends. However, these results were time consuming, taking approximately 4 hours to collect the 100 data points shown above. To achieve a more significant coverage in a more productive manner, the research team needed to develop a method of calculating velocity in each scan. Rather than the minimum 1 minute between calibration measurements, scan measurements can be collected less than 3 seconds apart. Therefore, calculating velocity from the raw data in each scan improves the productivity and achievable coverage by over 10 times. The method used to allow for this improvement is described in Appendix A.

To test the new velocity calculation scheme it was compared to the calibration velocity from the October testing reported in Section 4.1. Figure 53 shows direct velocity calculation vs calibration velocity at the points where calibration velocity was obtained. It can be observed that there is a good agreement between the independently calculated values. This suggests that the more efficient direct velocity calculation can be applied for future projects.

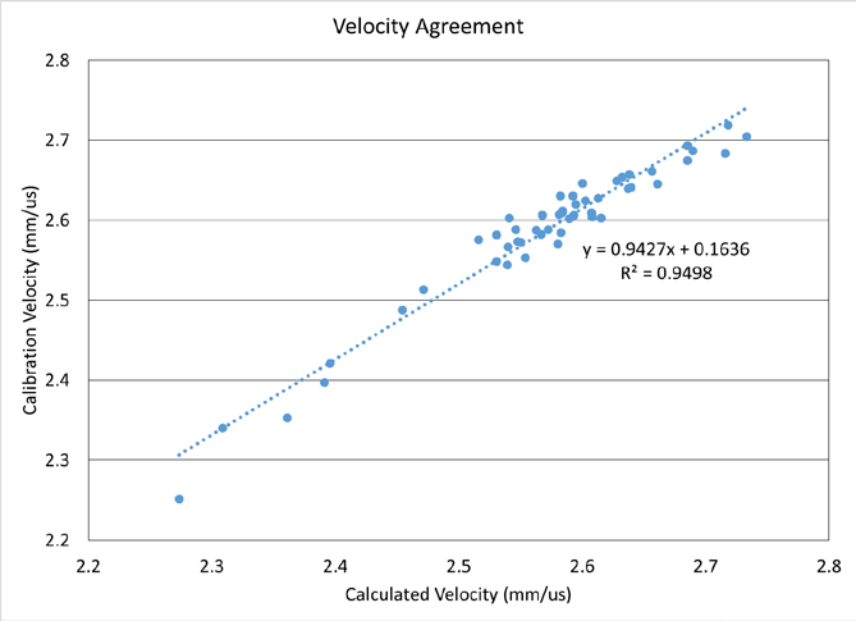

Figure 52: Direct velocity versus calibration velocity.

To illustrate the improvement with the new velocity calculation, the same plot shown in Figure 49 showing only calibration velocity is plotted in Figure 53 with all scans taken during the same time frame. It can be observed that the coverage and ability to identify trends in the data is improved with the new velocity calculation. The paver was moving in the direction of positive stationing, therefore lower stations reflect older pavement ages within the span of the day. The plots show the large changes in velocity that can occur within the time frame of a day at low ages due to the high strength development occurring.

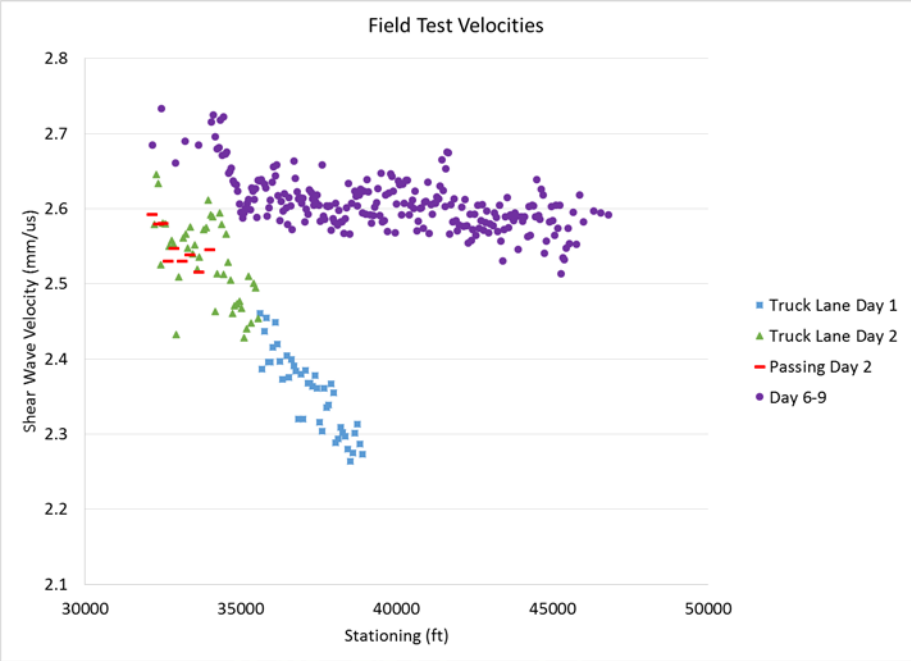

Figure 53: Velocities versus stationing using the new velocity method.

4.2 July 2014 Testing

4.2.1 July 18, 2014

Field tests were performed on the stretch of pavement that was poured using the same concrete mix design that was utilized for the Round 2 laboratory beam tests. This pavement was part of TH 65 in Minnesota and stretched from station 191+00 to 399+50. The pavement stationing and age information is shown below in Table 14. The mix design for this project is shown below in Table 15. Figure 54 shows that the same velocity gain trend observed in the lab is also observed in the field. Figure 55 shows a section of pavement containing 2 and 3 day old concrete measurements. It can be observed that some values exceed the average 6 day velocity measurements. This type of relative velocity criteria can be used to provide an input in opening to traffic decisions which are independent of the day after paving.

Table 14: July Field Testing Pavement Information

Stationing	Lane Position	Pour Date	Age on July 18th
264+50 to 315+00	Right Shoulder	7/17/2014	1 day
217+00 to 264+50	Right Shoulder	7/16/2014	2 days
191+00 to 217+00	Right Shoulder	7/15/2014	3 days
291+06 to 315+00	Both Lanes	7/14/2014	4 days
287+00 to 291+06	Both Lanes	7/12/2014	6 days

Table 15: July Field Testing Mix Design

Mix	Quantity
Cement (Type I)	400 lbs/cubic yard
W/CM Ratio	0.34
Fly Ash (Class C)	160 lbs/cubic yard
Water	190 lbs/cubic yard
Air	7.0%
Fine Aggregate (sand)	1177 lbs/cubic yard
Coarse Aggregate (Med. Buck)	477 lbs/cubic yard
Coarse Aggregate (3/4"-)	890 lbs/cubic yard
Coarse Aggregate (1 ½")	636 lbs/cubic yard

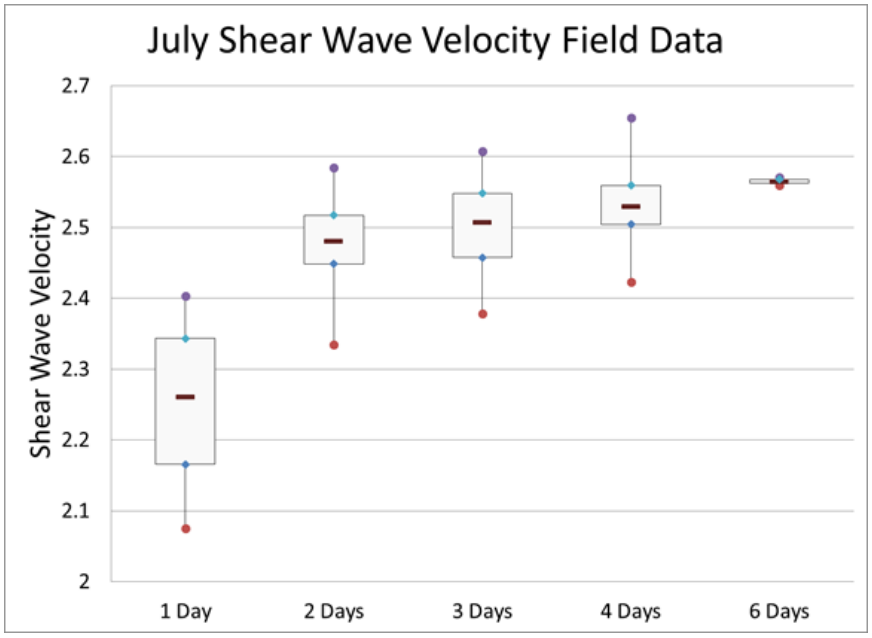

Figure 54: Velocity gain versus days after paving.

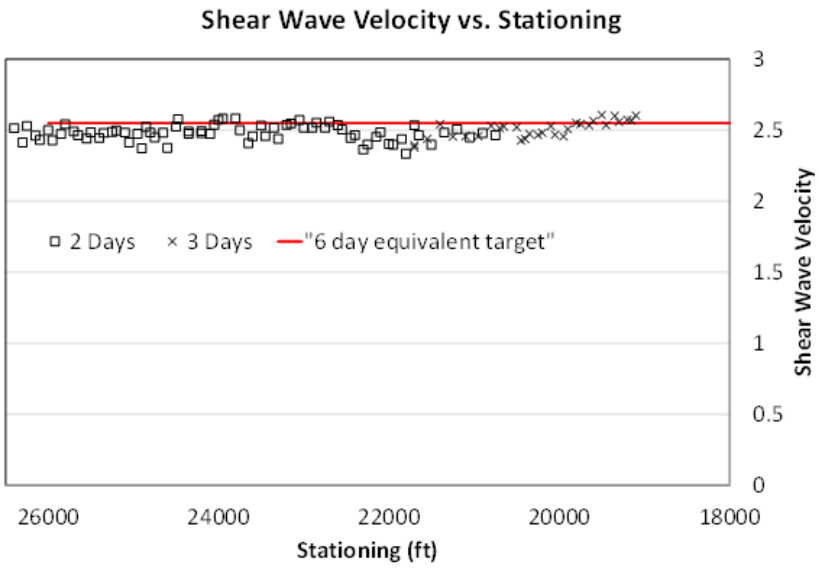

Figure 55: Example of day 2 and 3 velocities versus the day 6 average values.

4.3 Conclusions

The laboratory methods were implemented in a full scale, in-situ pavement field environment to determine applicability. Field testing showed that shear wave velocity development with hydration of the concrete matched the same curves observed in the laboratory. The development of an automated velocity calculation scheme increased the coverage to allow for improved evaluation of relative hydration throughout the project. This data can be used in the strength of opening to traffic models for performance-prediction based criteria.

Chapter 5: Recommendations for Traffic Opening

The current criteria for the time to traffic opening on new concrete pavements are based on purely empirical methods. These criteria require wait periods after concrete placement or achievement of certain levels of compressive and/or flexural strength. To achieve the objectives of this study, a mechanistic-based procedure for evaluating the effect of early traffic opening on long-term damage accumulation was developed which utilizes the results found from the laboratory and field studies.

The basis of this procedure is a modification of the MEPDG fatigue damage analysis in order to analyze traffic loading on the first 28 days of pavement life. The laboratory and field trial results were utilized in order to formulate strength development and modulus curves. These curves provide critical data for the development of a traffic opening timing analysis. The procedure will allow the user to specify age in days for potential opening to traffic and, subsequently, run initial predictions of early damage analysis for planning purposes. The tool provided to MnDOT allows for adjustments to the damage model prediction based on results of nondestructive (maturity or shear wave velocity) field testing of the as-constructed pavement. As such, the early opening decisions are based upon in-situ conditions.

5.1 Early Age Fatigue Damage Analysis Procedure

In this study, the MEPDG framework for fatigue cracking analysis has been adapted for determination of the damage. The MEPDG fatigue cracking model implies that cracking in the PCC layer is a function of the applied stress from each axle load application and thus depends on the various factors related to traffic loads and temperature gradients.

5.1.1 Overview of the MEPDG Fatigue Analysis

The overall processes for JPCP fatigue analysis include the following steps (NCHRP 2003):

1. Assemble a trial design for specific site conditions such as traffic, climate, and foundation—define PCC and other paving material properties, design and construction features.
2. Process inputs to obtain monthly values of traffic, material, and climatic inputs needed in the design evaluations for the entire design period.
3. Compute structural responses (longitudinal edge and mid-slab stresses) using finite element based rapid solution models for each axle type and load and for each damage-calculation increment throughout the design period.
4. Calculate accumulated damage at each month of the entire design period.

The MEPDG fatigue cracking model has the following form:

$$CRK = \frac{100}{1 + FD^{-1.68}} \tag{5.1}$$

$$FD = \sum \frac{n_{t,j,k,l,m,p}}{N_{t,j,k,l,m,p}} \tag{5.2}$$

$$\log(N_{t,j,k,l,m,p}) = C_1 . \left(\frac{MR}{\sigma_{t,j,k,l,m,p}} \right)^{C_2} \tag{5.3}$$

where *CRK* is the percentage of bottom-up or top-down PCC cracking; *FD* is the fatigue damage; *n* is the applied number of load applications at conditions *t, j, k, l, m,* and *p*; *N* is the allowable number of load applications at conditions *t, j, k, l, m, p; t, j, k, l, m,* and *p* are conditions relating to the age, month, axle type, load level, temperature difference, and traffic path, respectively; *MR* is the modulus of rupture of PCC; σ is the applied stress at conditions *t, j, k, l, m,* and *p*; and C_1 and C_2 are calibration constants (C_1 = 2.0; C_2 = 1.22).

Accurate computation of the stress at the critical location in the PCC layer and determination of PCC strength at the time of loading is required for the calculation of fatigue cracking. The following factors are accounted for in the MEPDG stress analysis and affect the magnitude of bending stresses in PCC slabs (NCHRP 2003):

- Slab thickness.
- PCC modulus of elasticity.
- PCC Poisson's ratio.
- PCC unit weight.
- PCC coefficient of thermal expansion.
- Base thickness.
- Base modulus of elasticity.
- Base unit weight (for bonded interface between PCC slab and base).
- Interface condition between the PCC slab and base.
- Joint spacing.
- Subgrade stiffness.
- Lane-shoulder joint LTE.
- Longitudinal joint lane-to-lane LTE (for widened slab pavement).
- Temperature distribution through the slab thickness.
- Moisture distribution through the slab thickness.
- Magnitude of effective permanent curl/warp.
- Load configuration
    - Bottom-up cracking – axle type (single, tandem, tridem, and quad axles).
    - Top-down cracking – short, medium, and long wheelbase.
- Axle weight.

- Wheel tire pressure and wheel aspect ratio (length-to-width ratio).
- Axle position (distance from the critical slab edge).

The raw design inputs have to be processed to obtain monthly values of the traffic, material, and climatic inputs needed in the design evaluations, which consist of the following:

- PCC strength and modulus at each month of the analysis period.
- Average daily number of single, tandem, tridem, and quad axles in each axle weight category for each month of the analysis period.
- Temperatures at 11 evenly spaced nodes in the PCC layer for every hour of the available climatic data to be converted into a distribution of linear temperature gradient frequency.
- Average monthly relative humidity for each calendar month.
- Monthly average moduli values of the base layer.
- Monthly average effective subgrade modulus of reaction (k-value) determined based on subgrade resilient modulus (the raw design input).

Since characterization of PCC properties, traffic, and temperature was modified for the early age damage analysis, a brief description of the MEPDG procedure for determination of these items is provided below.

PCC Properties. The MEPDG uses the following models for characterization of PCC strength and modulus of elasticity if long-term development of these properties is not known:

- PCC modulus of elasticity at 28 days, Ec, is determined directly from measurements at the age of 28 days or determined indirectly from 28-day estimates of flexural strength, MR, or compressive strength f'_c using he following relationships:

$$E_c = 33\rho^{3/2} (f'_c)^{1/2} \quad (5.4)$$

$$E_c = 3.47\rho^{3/2} MR \quad (5.5)$$

where,

Ec = PCC elastic modulus, psi.

ρ = unit weight of concrete, lb/ft^3.

f'_c= compressive strength of PCC, psi.

MR = flexural strength of PCC, psi

- MR at any age after 28 days is estimated using the following relationships:

$$STRRATIO = 1.0 + 0.12*\log_{10}(AGE/0.0767) - 0.01566*[\log_{10}(AGE/0.0767)]^2$$

where

STRRATIO = strength ratio of MR at a given age to MR at 28 days.

AGE = specimen age in years.

PCC modulus of elasticity at given time, t, is determined first from MR(t), using equation (5.5)

Traffic Characterization. The MEPDG considers the following load configuration:

- Single, tandem, tridem, and quad axles for bottom-up cracking.
- Short, medium, and long wheelbase for top-down cracking.

and requires the specification of the number of load applications for each axle types and load levels

- Single axles – 3,000 to 41,000 lb in 1,000 lb increment.
- Tandem axles – 6,000 to 82,000 lb in 2,000 lb increment.
- Tridem axles – 12,000 to 102,000 lb in 3,000 lb increment.
- Quad axles – 12,000 to 102,000 lb in 3,000 lb increment.

Temperature Characterization. Figure 5656 illustrates the thermal states considered by the MEPDG, the linear and nonlinear components being used in the critical stress and number of load calculations.

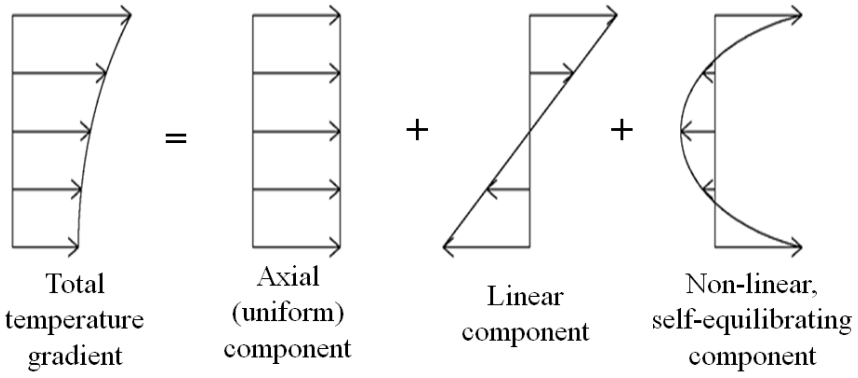

Figure 56: Components of the stress causing thermal gradient

The MEPDG linearization process eliminates the need to compute the number of loads as a function of both linear and nonlinear temperature gradients by equating stresses due to nonlinear gradients with those due to linear gradients. The first step in this process is to compute the monthly PCC stresses frequency distribution in the pavement at critical locations for linear temperature gradients, ΔTL, non-linear temperature gradients, and standard axle loading. For bottom-up damage accumulation, an 18-kip single axle load is placed at the mid-slab edge, where it will produce the maximum stress, as shown in Figure 57 on the left. For top-down damage accumulation, a 12-kip single axle load and a 34-kip tandem axle load with a medium wheel base is placed at the critical loading location, as shown in Figure 5757 on the right.

The second step in the linearization process involves finding the frequency distribution of linear temperature gradients, in increments of 2°F, which produces the PCC bending stress frequency distribution (w/o non-linear temperature stresses) the same as the stress distribution from step 1. Though the temperature frequency distribution for each month is developed only for the standard load and wheel offset conditions, it is then used in the fatigue analysis for all axle loads and offsets conditions. This process drastically reduces the amount of computing required to estimate stresses, which was a major concern at the time of the MEPDG development. However, it introduces inaccuracy which is important for early age analysis, and thus was modified as part of this study.

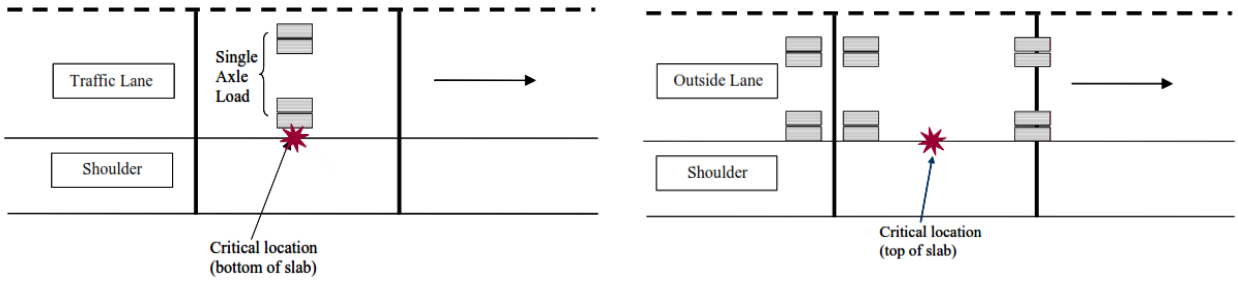

Figure 57: Critical load and stress locations for bottom-up cracking (at left) and top-down cracking (at right) (from NCHRP 2003)

5.1.2 Early PCC Age Fatigue Analysis

In this study, the MEPDG fatigue analysis was adapted for early edge damage analysis resulting in the fatigue damage formulation for the early age loading. The formulation is similar to that for the long term prediction and has the following form:

$$FD_{early} = \sum \frac{n_{t,j,k,l,m1,m2,p}}{N_{t,j,k,l,m1,m2,p}} \quad (5.6)$$

$$Log\left(N_{t,j,k,l,m1,m2,p}\right) = C_1 \left(\frac{MR_t/\beta}{\sigma_{t,j,k,l,m1,m2,p}}\right) \quad (5.7)$$

where *FD* is the fatigue damage; *n* is the applied number of load applications at conditions *t, j, k, l, m1, m2,* and *p*; *N* is the allowable number of load applications at conditions *t, j, k, l, m1, m2,* and *p* are conditions relating to the age (day), axle type, load level, temperature difference, non-linear temperature condition, and traffic path, respectively; *MR* is the modulus of rupture of PCC; σ is the applied stress at conditions *t, j, k, l, m,* and *p*; and β is a safety factor accounting for a higher risk associated with an early loading cracking.

To quantify the effect of early opening on fatigue damage consumption, the cumulative fatigue damage from the day of potential traffic opening until 28 days is normalized to the fatigue damage cumulated over the first year of pavement life:

$$RD = \frac{FD_{early}}{FD_{year1}} \quad (5.8)$$

The main differences between the early age fatigue analysis and the conventional MEPDG fatigue analysis are as follows:

Damage Increment. The early age and conventional fatigue analyses use the incremental damage approach, but the early age analysis computes fatigue damage on a daily basis while the conventional fatigue MEPDG analysis is done on a monthly basis. MEPDG inputs are still utilized during the first 28 days, except some PCC properties and traffic parameters which are modified to allow for daily incremented calculations in the first 28 days of the pavement life for early opening analysis. This means that the 28th day after pavement construction is the end of the construction month. The first day of the next month is the day of opening to a regular traffic.

PCC Characterization. The MEPDG assumes that concrete flexural strength does not vary within a month. This assumption is reasonable for concrete after 28 days from placement. However, for early ages concrete (i.e. before 28 days) concrete properties vary significantly. In this study, it is assumed that the properties vary on a daily basis.

Based on the results of the laboratory study, the following relationship between concrete elastic moduli and age was developed (see Figure 58):

$$E_c(t) / E_c(28) = (t/28)^{0.0982} \quad (5.9)$$

where t is PCC age in days.

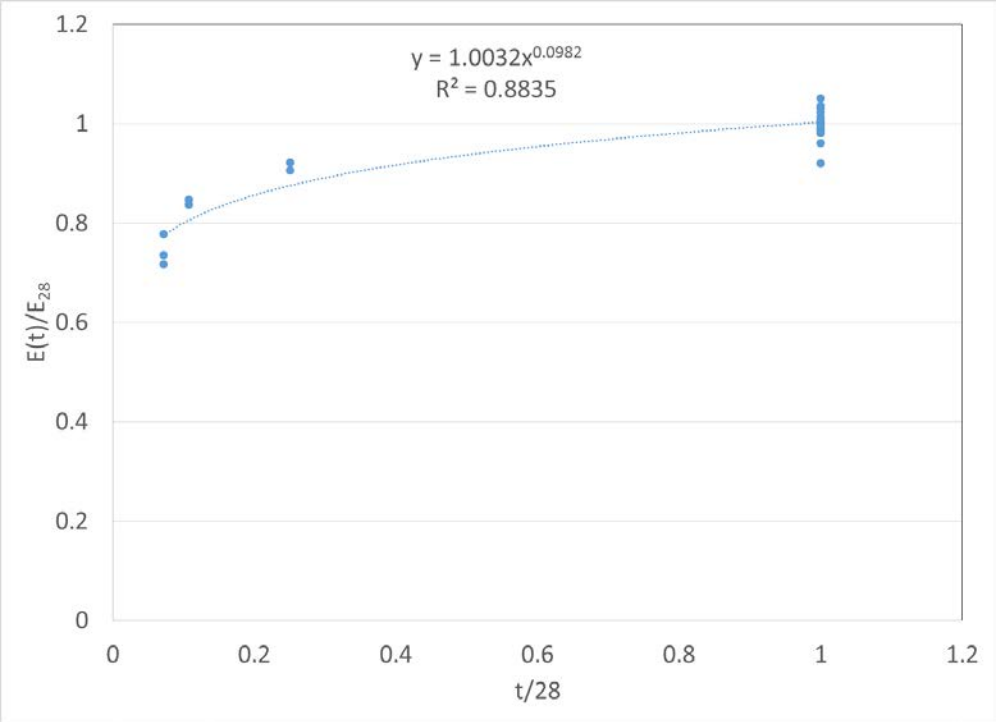

Figure 58: Normalized concrete elastic modulus at early age vs. time in days.

The following model was developed for the relationship between concrete flexural strength and age (see Figure 59):

$$STRRATIO = (t/28)^{0.0982} \quad (5.10)$$

where

STRRATIO = strength ratio of MR at a given age to MR at 28 days.

t = specimen age in days

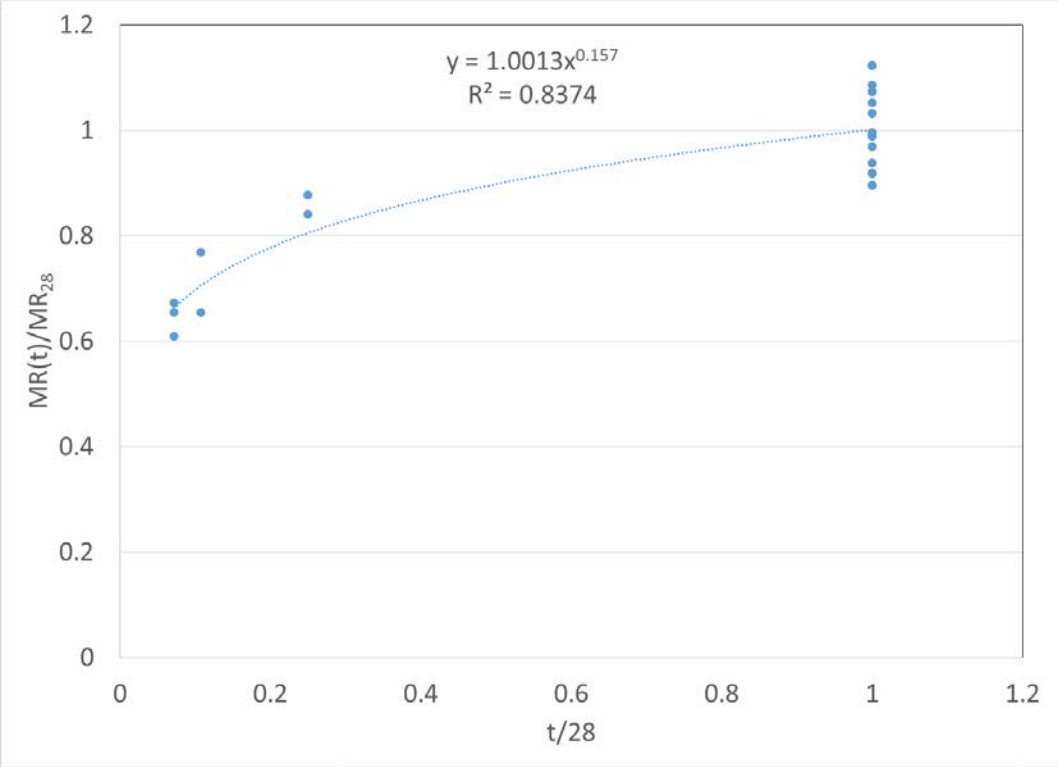

Figure 59: Normalized concrete flexural strength at early age vs. time in days.

It should be noted that these relationships should be used as the default curve only if no other information is available. It is desirable to develop a mix-specific relationship for each new PCC mix design, especially if the source of aggregates or cement have changed.

It should also be noted that time-strength and time-modulus relationships developed in the lab may require adjustment in the field due to variation in temperature conditions. One option is to account for it using a maturity concept [Izevbekhai and Rohne, 2009]. Another alternative is to determine the concrete modulus from the shear wave testing at time t_1, via 5.11, and update the PCC modulus-time relationship as shown in 5.12:

$$C_S = \sqrt{\frac{E}{2(1+\mu)\rho}} \qquad (5.11)$$

$$E_c(t_1) / E_c(28) = (t/28)^a \qquad (5.12)$$

Where

$$a = \frac{Log\left(\frac{Ec(t_1)}{Ec(28)}\right)}{Log\ (t_1/28)}$$

Similarly, if the flexural strength at time t_1 is determined using the maturity concept from a correlation with the shear wave testing results, then the strength development curve can be updated as follows:

$MR(t_1) / MR28 = (t/28)^a$ (5.13)

where

$$a = \frac{Log\left(\frac{MR(t_1)}{MR28}\right)}{Log\,(t_1/28)}$$

These options allow the user to update the effect of early opening on damage, using field measures of the field conditions.

Traffic Characterization. To be consistent with the MEPDG fatigue analysis, the same characterization of the axle spectrum is adapted for the early age analysis, but the user is allowed to specify a different traffic spectrum for the pavement age less than 28 days than that which is used for the first year of the design life.

Temperature Characterization. While the temperature linearization procedure currently used in the MPEDG drastically reduces the computational load of the AASHTO M-E JPCP procedure, it has some drawbacks. The main disadvantage to this process is that it assumes that the component of stress due to the interaction between nonlinear temperature and traffic is constant for all traffic loads. While this assumption has been overlooked until now, it is obviously a simplification that should be called into question when investigating the effect of PCC curling at early age. To address this limitation, the temperature gradients from hourly temperature predictions for each month were converted into a 2-dimentional frequency distribution.

The early age fatigue damage analysis was implemented into a Fortran program, EarlyDam, which is a modified version of the MEPDG transverse cracking model. Moreover, to eliminate a possible inaccuracy of comparing the early age (up to 28 days) damage and the MEPDG first year damages due differences in handling the non-linear temperature distribution, the analysis for the first year is also performed using the modified non-linear temperature distribution analysis.

The EarlyDam reads the same inputs as the MEPDG cracking program, but requires 4 additional input files:

1. Input file containing information on
    a. Age of traffic opening, days
    b. Month of pavement construction
    c. Design (28 days) PCC strength and elastic modulus
    d. PCC strength and elastic modulus for each day from the age at traffic opening to 28 days
2. Daily single axle loading distribution from the age at traffic opening to 28 days
3. Daily tandem axle loading distribution from the age at traffic opening to 28 days
4. Daily tridem axle loading distribution from the age at traffic opening to 28 days

5.2 Early Traffic Opening Analysis Procedure

The fatigue damage procedure presented above is an important element of the proposed early opening to traffic analysis procedure. This procedure involves the following steps:

1. Obtain PCC mix-specific strength and modulus values, including PCC strength and elastic modulus at 28 days as well development curves with respect to:
    a. Time
    b. Shear Wave Velocity
    c. Maturity

    If this information is not available, then default curves included in the program should be used.

2. Perform MEPDG simulation of the pavement fatigue damage.
3. Select the appropriate strength safety factor. This safety factor should account for variation in assumed flexural strength development versus the actual strength development as well as variation due to field conditions.

4. Generate additional input files for the early age fatigue damage analysis, EarlyDam.

5. Perform analysis on selected design and traffic for various possible opening ages.

6. Select target opening age based on acceptable damage level

7. During construction, Monitor field PCC development using either:
    a. Shear-wave velocity
    b. Maturity

8. Update predicted strength and modulus curves based upon absolute measured conditions

9. Update analysis to recalculate predefined inputs using updated in-situ curves

10. Update target opening as needed

11. Repeat steps 7-10 as field monitoring data is available and as needed based upon damage prediction results

5.3 Rudimentary Software

To facilitate an implementation of the procedure for early opening traffic analysis, rudimentary software was developed. To simplify the analysis and make it compatible with MnPAVE-Rigid (MnDOT 2015), the program utilizes the database of the MEPDG projects used for development of MnPAVE-Rigid. Once initially opening the program, the screen will appear as shown in Figure 60 below. The main screen asks the user to specify the district in which the pavement is

located, PCC thickness, joint spacing, presence of a widened lane, shoulder type, construction month, day opening to traffic, and trucks per day.

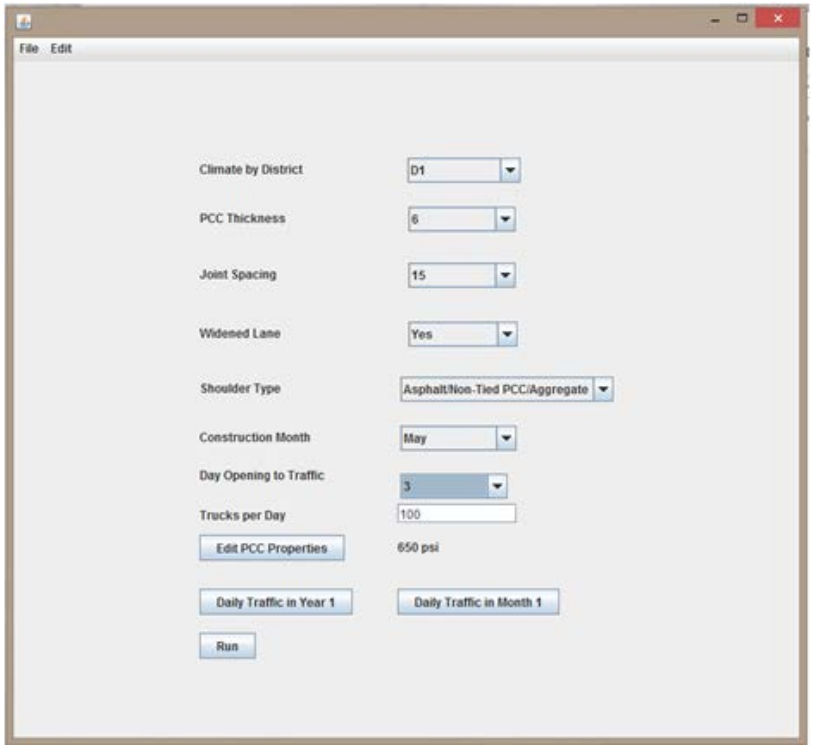

Figure 60: Opening screen of program.

Once these inputs have been provided, the user can adjust the PCC properties by clicking the "Edit PCC Properties" button. By doing so, the window shown in Figure 61 will appear. This screen allows the user to input the design 28 day flexural strength. An early strength safety factor can also be chosen, and, in pushing the "Calculate Epcc at 28 days" button, the modulus is calculated. After this value is calculated, pressing the "update with model" button will result in the table filling with tabulated values which make up the strength and modulus curves necessary for analysis. Once this portion of the procedure is complete, the "OK" button can be pressed and the program will return to the main screen.

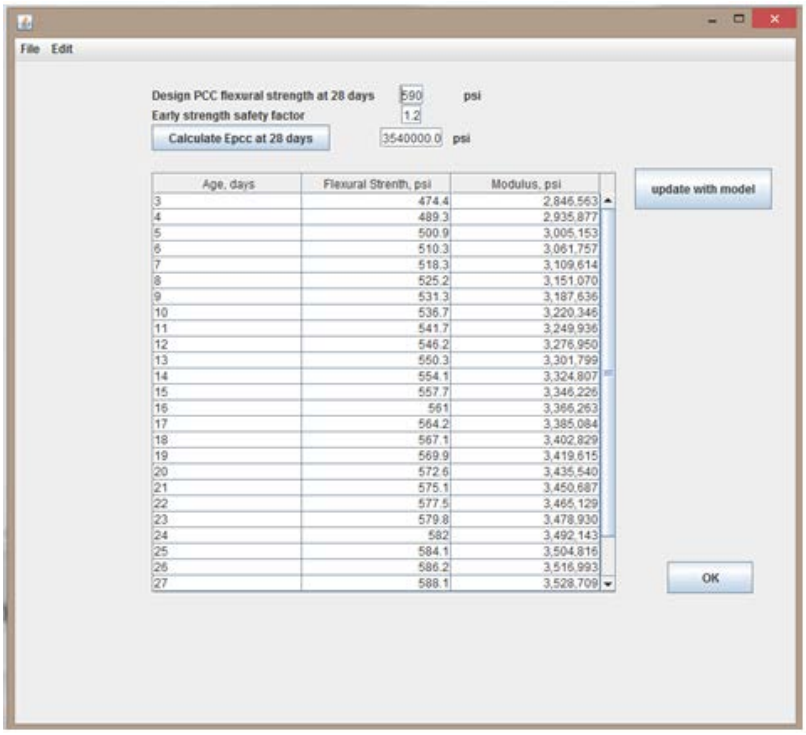

Age, days	Flexural Strenth, psi	Modulus, psi
3	474.4	2,846,563
4	489.3	2,935,877
5	500.9	3,005,153
6	510.3	3,061,757
7	518.3	3,109,614
8	525.2	3,151,070
9	531.3	3,187,636
10	536.7	3,220,346
11	541.7	3,249,936
12	546.2	3,276,950
13	550.3	3,301,799
14	554.1	3,324,807
15	557.7	3,346,226
16	561	3,366,263
17	564.2	3,385,084
18	567.1	3,402,829
19	569.9	3,419,615
20	572.6	3,435,540
21	575.1	3,450,687
22	577.5	3,465,129
23	579.8	3,478,930
24	582	3,492,143
25	584.1	3,504,816
26	586.2	3,516,993
27	588.1	3,528,709

Figure 61: Program appearance after hitting the "Edit PCC Properties" button

Once at the main screen, the daily traffic can be assigned for analysis. By pressing the "Daily Traffic in Year 1" button, the screen shown in Figure 62 will appear. This screen enables the user to input project-specific traffic information relating to the axle weight and type. This traffic information is used for analysis of the pavement for months 2-13. Once this information has been provided, the program will return to the main screen after the "OK" button is pressed. The same process is followed for the traffic during the first month by pressing the "Daily Traffic in Month 1" button. The screen shown in Figure 63 will then appear and inputs similar to those for months 2-13 can be provided. Once this is complete, the "OK" button can again be utilized to return to the main screen.

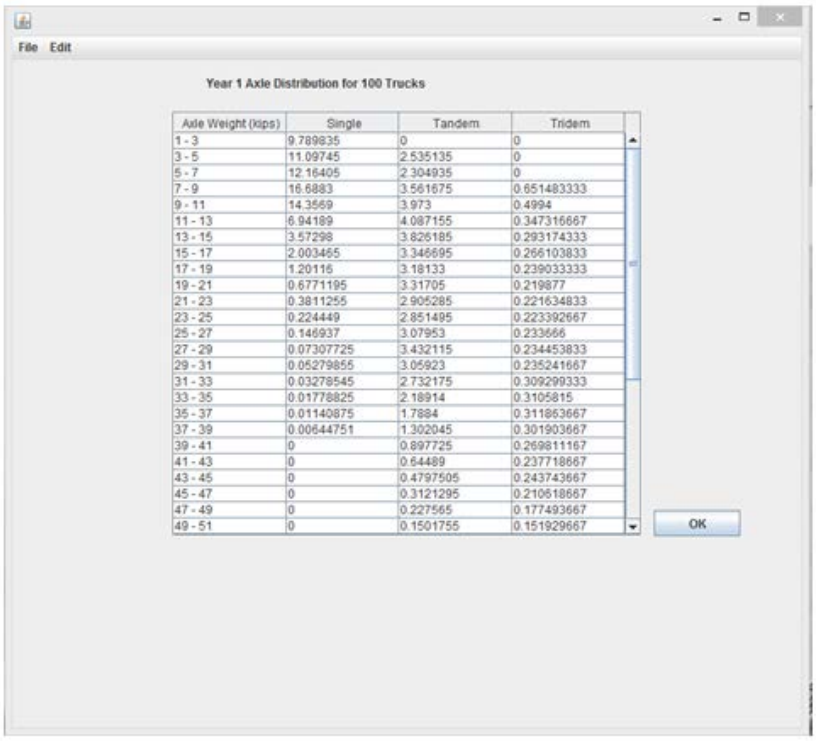

Axle Weight (kips)	Single	Tandem	Tridem
1 - 3	9.789835	0	0
3 - 5	11.09745	2.535135	0
5 - 7	12.16405	2.304935	0
7 - 9	16.6883	3.561675	0.651483333
9 - 11	14.3569	3.973	0.4994
11 - 13	6.94189	4.087155	0.347316667
13 - 15	3.57298	3.826185	0.293174333
15 - 17	2.003465	3.346695	0.266103833
17 - 19	1.20116	3.18133	0.239033333
19 - 21	0.6771195	3.31705	0.219877
21 - 23	0.3811255	2.905285	0.221634833
23 - 25	0.224449	2.851495	0.223392667
25 - 27	0.146937	3.07953	0.233666
27 - 29	0.07307725	3.432115	0.234453833
29 - 31	0.05279855	3.05923	0.235241667
31 - 33	0.03278545	2.732175	0.309299333
33 - 35	0.01778825	2.18914	0.3105815
35 - 37	0.01140875	1.7884	0.311863667
37 - 39	0.00644751	1.302045	0.301903667
39 - 41	0	0.897725	0.269811167
41 - 43	0	0.64489	0.237718667
43 - 45	0	0.4797505	0.243743667
45 - 47	0	0.3121295	0.210618667
47 - 49	0	0.227565	0.177493667
49 - 51	0	0.1501755	0.151929667

Figure 62: Program screen for daily traffic in year 1 inputs.

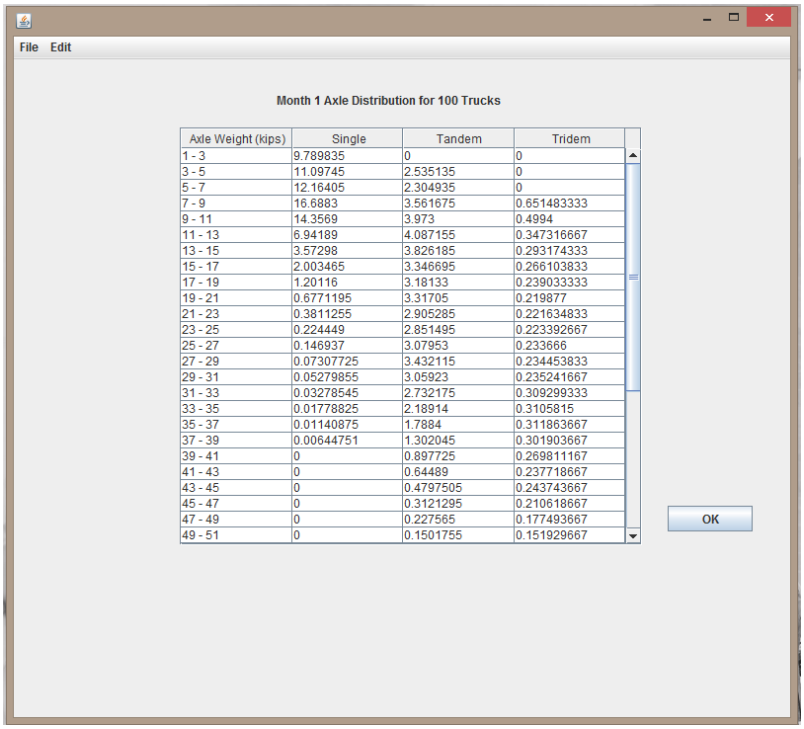

Axle Weight (kips)	Single	Tandem	Tridem
1 - 3	9.789835	0	0
3 - 5	11.09745	2.535135	0
5 - 7	12.16405	2.304935	0
7 - 9	16.6883	3.561675	0.651483333
9 - 11	14.3569	3.973	0.4994
11 - 13	6.94189	4.087155	0.347316667
13 - 15	3.57298	3.826185	0.293174333
15 - 17	2.003465	3.346695	0.266103833
17 - 19	1.20116	3.18133	0.239033333
19 - 21	0.6771195	3.31705	0.219877
21 - 23	0.3811255	2.905285	0.221634833
23 - 25	0.224449	2.851495	0.223392667
25 - 27	0.146937	3.07953	0.233666
27 - 29	0.07307725	3.432115	0.234453833
29 - 31	0.05279855	3.05923	0.235241667
31 - 33	0.03278545	2.732175	0.309299333
33 - 35	0.01778825	2.18914	0.3105815
35 - 37	0.01140875	1.7884	0.311863667
37 - 39	0.00644751	1.302045	0.301903667
39 - 41	0	0.897725	0.269811167
41 - 43	0	0.64489	0.237718667
43 - 45	0	0.4797505	0.243743667
45 - 47	0	0.3121295	0.210618667
47 - 49	0	0.227565	0.177493667
49 - 51	0	0.1501755	0.151929667

Figure 63: Program screen for daily traffic in month 1 inputs.

After all of the inputs have been provided, pressing the "Run" button will begin the analysis. After the analysis is complete, the damage ratio will appear in red as seen in Figure 64. The resulting output is in the form of a damage ratio defined as: $\frac{month\ 1\ damage}{months\ 2\ to\ 13\ damage}$. It follows that a higher damage ratio is indicative of greater early age damage. It is also worth noting that if the ratio is roughly 1/12, the damage within the first month is equivalent to that which occurs in each of the 12 months after (i.e. no effect). To show the effect of changing certain inputs, Figure 65 shows a different analysis performed using changed inputs for the widened lane and shoulder type variables. As can be observed, the use of no widened lane increased the predicted damage ratio.

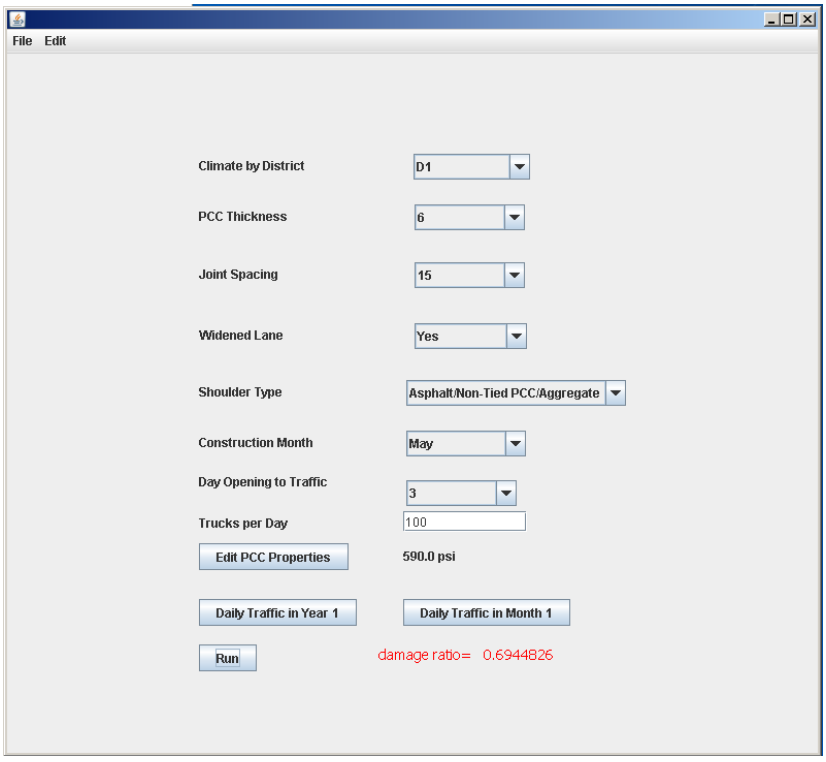

Figure 64: Program results for trial analysis.

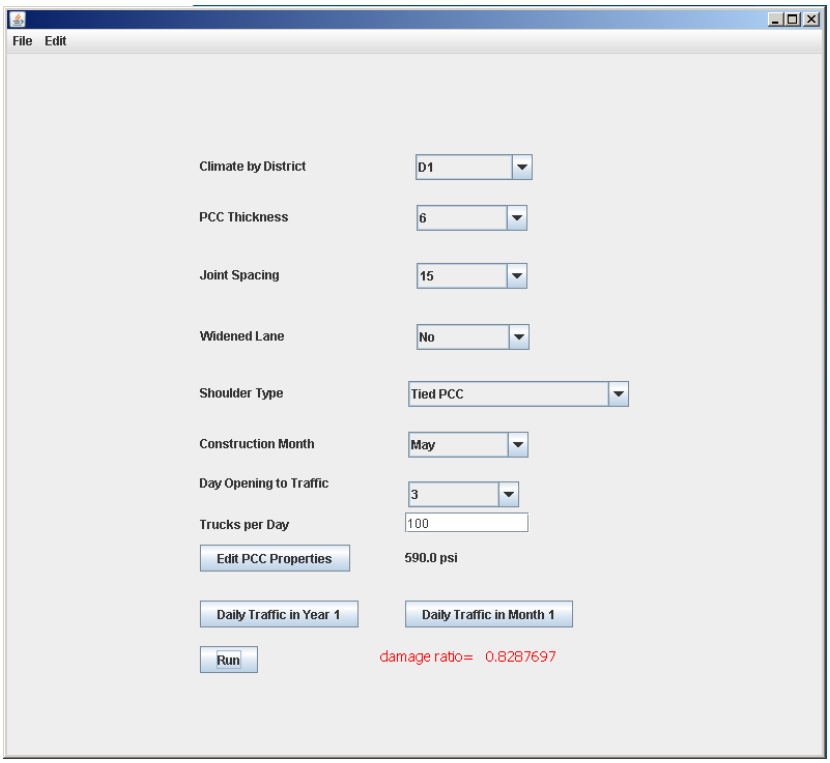

Figure 65: Program results for varied input analysis.

5.4 Summary

To achieve the objectives of this study, a mechanistic-based procedure for evaluating the effect of early traffic opening on long-term damage accumulation was developed using relationships obtained from a comprehensive laboratory study. The procedure was developed to allow for updated models based on field monitoring similar to that conducted as part of this study.

The basis of this procedure is a modification of the MEPDG fatigue damage analysis in order to analyze traffic loading on the first 28 days of pavement life. The laboratory and field trial results were utilized in order to formulate strength development and modulus curves. These curves provide critical data for the development of a traffic opening timing analysis. The procedure allows the user to specify age in days for potential opening to traffic and, subsequently, run initial predictions of early damage analysis for planning purposes. The tool provided to MnDOT will allow for adjustments to the damage model prediction based on results of nondestructive (maturity or shear wave velocity) field testing of the as-constructed pavement for early opening decisions based on in-situ conditions.

Chapter 6: Conclusions

Through extensive laboratory and field trials, a large quantity of early strength and shear wave velocity development data was collected. The first round of laboratory testing showed that loading at early ages caused decreases in 28-day ultimate strength when the beam was loaded prior to 7 days. The most significant signs of this decrease in strength occurred when beams were loaded before day 3. When wet curing was utilized for rounds 2 and 3, however, the results were inconclusive. The variability of the second round of testing was attributed to the fact that the loading was not increased with time to appropriately reflect the strength gain attributed to water curing and the subsequent hydration. Some iterations of the laboratory trials were inconclusive as to the effect of early age loading on ultimate strength, but this could be attributed to lack of accuracy inherently involved with the testing of small flexure beams.

Regardless of the variability with the flexural test results, the field trials were successful in verifying the shear wave velocity results that were seen in the lab. This is promising from an implementation standpoint due to the correlation of lab and field measurements, allowing for less reliance on in-situ testing.

The culmination of both the laboratory and field data was the formulation of a GUI program, requiring inputs that are similar to those required by MnDOT MnPAVE-Rigid. The strength and shear wave velocity development curves that resulted from the experimental trials were implemented into the program, allowing the user to input project-specific preliminary strength data, which results in the creation of unique curves. The end result of the program is a damage ratio that quantifies the damage that results from the opening inputs selected. This tool can be implemented by MnDOT and local transportation agencies for optimal timing of traffic opening.

References

Arndt, R. W., et al. 2011. "Monitoring of Reinforced Concrete Corrosion and Deterioration by Periodic Multi-Sensor Non-Destructive Evaluation." *AIP Conference Proceedings-American Institute of Physics*. Vol. 1335. No. 1. (2011).

Belli, K., Wadia-Fascetti, S., and Rappaport, C. 2008. "Model based evaluation of bridge decks using ground penetrating radar." *Computer-Aided Civil and Infrastructure Engineering* 23.1: 3-16.

Benedetto, A., G. Manacorda, A. Simi, and F. Tosti. 2012. "Novel perspectives in bridges inspection using GPR." *Nondestructive Testing and Evaluation* 27, no. 3: 239-251.

Bishko, A., Andrey A. Samokrutov, and Victor G. Shevaldykin. 2008. "Ultrasonic echo-pulse tomography of concrete using shear waves low-frequency phased antenna arrays." In *Proceedings of the 17th World Conference on Nondestructive Testing*, vol. 25, no. 28.10.

Blouin, A., Levesque, D., Neron, C., Drolet, D. and Monchalin, J.P., 1998. “Improved resolution and signal-to-noise ratio in laser-ultrasonics by SAFT processing.” *Optics Express*, *2*(13), pp.531-539.

Borwick, J., 1990. *Microphones: Technology and Technique*. Focal Press.

Buckley, J. and Loertscher, H., 1999. “Frequency considerations in air-coupled ultrasonic inspection.” *Insight*, *41*(11), pp.696-9.

Cao, Y., 2011. *Full Waveform Analysis of Ground Penetrating Radar Measurements* (Doctoral dissertation, University of Minnesota).

Yuejian, C., Guzina, B.B. and Labuz, J.F., 2008. “Pavement Evaluation Using Ground Penetrating Radar.” *Minnesota Department of Transportation.*

Cao, Y., Labuz, J. and Guzina, B. 2011. “Evaluating a Pavement System Based on GPR Full-Waveform Simulation.” *Transportation Research Board 90th Annual Meeting*.

Carino, N.J., 1993. ‘Characterization of electromagnetic covermeters.’ In *Conference Proceedings of the British Institute of Non-Destructive Testing International Conference, NDT in Civil Engineering 14-16 April 1993, Liverpool University. Volume 2.*

Carino, N.J., 2001, May. “The impact-echo method: an overview.” In *Proceedings of the 2001 Structures Congress & Exposition* (pp. 21-23).

Carino, N. J. 2004. “Chapter 5: The Maturity Method.” *Handbook on Nondestructive Testing of Concrete*, 2nd ed. CRC Press LLC, Boca Raton, FL.

Chung, C.W., 2010. *Ultrasonic wave reflection measurements on stiffening and setting of cement paste* (Doctoral dissertation, University of Illinois at Urbana-Champaign).

Crawford, G. I. 1997. “Guide to Nondestructive Testing of Concrete.” FHWA-SA-97-105. Federal Highway Administration, Washington, DC.

Crovetti, J. and Khazanovich, L. 2005. “Early Opening of Portland Cement Concrete (PCC) Pavements to Traffic,” *WHRP Project 0092-01-04 Final Report*, Milwaukee, Wisconsin, Marquette University, Department of Civil, Construction, and Environmental Engineering.

Catapano, I., Crocco, L., Morabito, A. F. & Soldovieri, F. 2012. “Tomographic imaging of holographic GPR data for non-invasive structural assessment: the Musmeci bridge investigation.” *Nondestructive Testing and Evaluation*, 27: 229-237.

Cho, Y. S. 2003. “Non-destructive testing of high strength concrete using spectral analysis of surface waves.” *NDT & E International*, 36: 229-235.

Clemena, G.G., 1991. “Short-pulse radar methods.” *CRC Handbook on Nondestructive Testing of Concrete*, pp.253-274.

Clemena, G.G., Jackson, D.R. and Crawford, G.C., 1992. “Inclusion of rebar corrosion rate measurements in condition surveys of concrete bridge decks.” *Transportation Research Record*, (1347).

Economou, N., Vafidis, A., Hamdan, H., Kritikakis, G., Andronikidis, N. & Dimitriadis, K. 2012. “Time-varying deconvolution of GPR data in civil engineering.” *Nondestructive Testing and Evaluation*, 27: 285-292.

Graveen, C. 2001. *Nondestructive Test Methods To Assess Pavement Quality For Use In A Performance-Related Specification*. (Doctoral dissertation, Purdue University).

Griffiths, D.J. and Reed College, 1999. *Introduction to electrodynamics* (Vol. 3). Upper Saddle River, NJ: prentice Hall.

Gucunski, N., Rascoe, C., Parrillo, R. and Roberts, R.L., 2009. “Complementary Condition Assessment of Bridge Decks by High-Frequency Ground-Penetrating Radar and Impact Echo.” In *Transportation Research Board 88th Annual Meeting* (No. 09-1282).

Gucunski, N., Romero, F., Kruschwitz, S., Feldmann, R., Abu-Hawash, A. & Dunn, M. 2010. “Multiple complementary nondestructive evaluation technologies for condition assessment of concrete bridge decks.” *Transportation Research Record*, 2201: 34-44.

Gucunski, N. & Woods, R. D. 1992. “Numerical simulation of the SASW test.” *Soil Dynamics and Earthquake Engineering*, 11: 213-227.

Guzina, B. B. & Bonnet, M. 2004. “Topological derivative for the inverse scattering of elastic waves.” *The Quarterly Journal of Mechanics and Applied Mathematics*, 57: 161-179.

Hoegh, K. and Khazanovich, L., 2012. “Correlation analysis of 2D tomographic images for flaw detection in pavements.” *ASTM International. Journal of Testing and Evaluation*, *40*(2): 247-255.

Hoegh, K., Khazanovich, L., Maser, K. and Tran, N., 2012a. “Evaluation of Ultrasonic Technique for Detecting Delamination in Asphalt Pavements.”*Transportation Research Record* (2306): 105-110.

Hoegh, K., Khazanovich, L. & Yu, H. T. 2011. “Ultrasonic Tomography for Evaluation of Concrete Pavements.” *Transportation Research Record*, 2232: 85-94.

Hoegh, K., Khazanovich, L. and Thomas Yu, H., 2012b. “Concrete Pavement Joint Diagnostics with Ultrasonic Tomography.” *Transportation Research Record, 2*(2305): 54-61.

Khazanovich, L., Velasquez, R. & Nesvijski, E. G. 2005. “Evaluation of top-down cracks in asphalt pavements by using a self-calibrating ultrasonic technique.” *Transportation Research Record*, 1940: 63-68.

Li, J., Zollinger, D. G. & Lytton, R. L. 2008. “Detection of Delamination in Concrete Pavements Using Ground-Coupled Ground-Penetrating Radar Technique.” *Transportation Research Record*, 2087: 68-77.

Liu, P. L. & Yeh, P. L. 2010. “Vertical spectral tomography of concrete structures based on impact echo depth spectra.” *NDT & E International*, 43: 45-53.

Liu, T., Zhou, J., Osterman, K. S., Zhang, P., Woodhouse, S. A., Schiff, P. B. & Kutcher, G. J. 2008. “Measurements of radiation-induced skin changes in breast-cancer radiation therapy using ultrasonic imaging.” *BioMedical Engineering and Informatics*, 718-722.

Lue, N., Choi, W., Popescu, G., Badizadegan, K., Dasari, R. R. & Feld, M. S. 2008. “Synthetic aperture tomographic phase microscopy for 3D imaging of live cells in translational motion.” *Optics Express*, 16: 16240-16246.

Maser, K. R. 1996. “Condition assessment of transportation infrastructure using ground-penetrating radar.” *Journal of Infrastructure Systems*, 2: 94-101.

Maser, K. R. 2000. “Pavement characterization using ground penetrating radar: State of the art and current practice.” *ASTM Special Technical Publication*, 1375: 313-326.

Maser, K. R. 2008. “Integration of Ground Penetrating Radar and Infrared Thermography for Bridge Deck Condition Evaluation.” *Proc. of Symp. NDE/NDT for Highways and Bridges*, SMT, Citeseer, 67-74.

Maser, K. R. & Roddis, W. M. K. 1990. “Principles of thermography and radar for bridge deck assessment.” *Journal of Transportation Engineering*, 116: 583-601.

Mayer, K., Langenberg, K. J., Krause, M., Milmann, B. & Mielentz, F. 2008. “Characterization of reflector types by phase-sensitive ultrasonic data processing and imaging.” *Journal of Nondestructive Evaluation*, 27: 35-45.

Minalga, E., Payne, A., Merrill, R., Todd, N., Vijayakumar, S., Kholmovski, E., Parker, D.L. and Hadley, J.R., 2013. “An 11-channel radio frequency phased array coil for magnetic

resonance guided high-intensity focused ultrasound of the breast." *Magnetic Resonance in Medicine, 69*(1): 295-302.

MnDOT. 2014. Internet. MnPAVE-Rigid: rigid (PCC) pavement design. http://www.dot.state.mn.us/materials/pvmtdesign/software.html. (Accessed Nov. 24, 2015.

Moheimani, S. O. R. 2003. "A survey of recent innovations in vibration damping and control using shunted piezoelectric transducers." *Control Systems Technology, IEEE Transactions*, 11: 482-494.

Morey, R. M. 1998. "Ground Penetrating Radar for Evaluating Subsurface Conditions for Transportation Facilities: A Synthesis of Highway Practice." *National Cooperative Highway Research Program, National Academy Press.* Volume 255, Washington, D.C.

Moropoulou, A., Avdelidis, N. P., Koui, M., Aggelopoulos, A. & Karmis, P. 2002. "Infrared thermography and ground penetrating radar for airport pavements assessment." *Nondestructive Testing and Evaluation*, 18: 37-42.

Mccullough, F., Rasmussen, R. 1999 "Fast Track Paving: Concrete Temperature Control and Traffic Opening Criteria for Bonded Concrete Overlays Volume I," *Final Report No. FHWA-RD098-167.*

Nelson, P. K. 2003. "Handbook of Nondestructive and Innovative Testing Equipment for Concrete." *Federal Highway Administration*, Washington, DC.

NRMCA. 2006. "Concrete in Practice: What, Why and How? CIP 39- Maturity Methods to Estimate Concrete Strength." *National Ready Mixed Concrete Association*. Silver Spring, MD.

Nesvijski, E. 1997. "On the Problem of Application of the Conic and Exponential Wave Guiding Extensions for Ultrasonic Transducers for Materials Testing." *Journal: NASTA Technical Bulletin*: 49-56.

Nesvijski, E. G. 2000. "Some aspects of ultrasonic testing of composites." *Composite Structures*, 48: 151-155.

Nesvijski, E. G. 2003. "Dry Point Contact Transducers: Design for New Applications." *Journal of Nondestructive Testing*, 8: 1-10.

Olek, J., M. D. Cohen, C. F. Scholer, And D. R . Mandrekar. 2003. "Use of Modulus of Rupture, Fatigue Resistance and Maturity in Determining Opening to Traffic Time for Concrete Pavements." *Publication FHWA/IN/JTRP-2000/25*. Joint Transportation Research Program, Indiana Department of Transportation and Purdue University, West Lafayette, IN.

Park, C. B., Miller, R. D. & Xia, J. 1999. "Multichannel analysis of surface waves (MASW)." *Geophysics*, 64: 800-808.

Plati, C. & Loizos, A. 2012. “Using ground-penetrating radar for assessing the structural needs of asphalt pavements.” *Nondestructive Testing and Evaluation*, 27: 273-284.

Popovics, J.S., Oh, T. and Ham, S. 2012. “Effective visualization of impact-echo data for bridge deck NDE.” *Review of Progress in Quantitative Nondestructive Evaluation: Volume 31*, 1430, No. 1: 1681-1688.

Popovics, S. and Popovics, J.S., 1997. “A critique of the ultrasonic pulse velocity method for testing concrete.” *NDT and E International*, *4*(30): 260.

Providakis, C. P., E. V. Liarakos, And E. Kampianakis, “Nondestructive Wireless Monitoring of Early-Age Concrete Strength Gain Using an Innovative Electromechanical Impedance Sensing System,” *Smart Materials Research*, 2013: 1-10.

Roesler, J., Harvey, J.H., Farver, J., Long, F. 2000. “Investigation of Design and Construction Issues for Long Life Concrete Pavement Strategies.” *No. FHWA/CA/OR-2000/04*. Pavement Research Center, Institute of Transportation Studies, University of California, Berkeley.

Rohne, R., Izevbekhai, B. 2009. “Demonstration of Concrete Maturity Test Process on the TH-694/ TH-35E Interchange - Unweave the Weave.” *Rep. no. MN/RC 2009-26*. Minnesota Department of Transportation, Maplewood, MN.

Rupitsch, S. J., Maier, F. & Zagar, B. G. 2006. “Synthetic Aperture Focusing Technique in High-Frequency Ultrasound Imaging to Locate Layer Delamination.” *Proceedings of the IEEE*, 2006: 1953-1958.

Saarenketo, T. & Scullion, T. 2000. “Road evaluation with ground penetrating radar.” *Journal of Applied Geophysics*, 43: 119-138.

Schubert, F., Koehler, B. 2001. “Three-dimensional time domain modeling of ultrasonic wave propagation in concrete in explicit consideration of aggregates and porosity.” *Journal of Computational Acoustics*, 9: 1543-1560.

Schubert, F. & Köhler, B. 2008. “Ten lectures on impact-echo.” *Journal of Nondestructive Evaluation*, 27: 5-21.

Schubert, F., Lausch, R. & Wiggenhauser, H. 2003. “Geometrical effects on impact-echo testing of finite concrete specimens.” *Proceedings of International Symposium Non-Destructive Testing in Civil Engineering (NDT-CE)*, Berlin, Germany, Sept. 16-19.

Schubert, F., Wiggenhauser, H. & Lausch, R. 2004. “On the accuracy of thickness measurements in impact-echo testing of finite concrete specimens—numerical and experimental results.” *Ultrasonics*, 42: 897-901.

Scott, M., Duke, J. C., Davidson, N., Washed, G. & Weyers, R. 2000. “Automated characterization of bridge deck distress using pattern recognition analysis of ground penetrating radar data.” *Materials evaluation*, 58: 1305-1309.

Scott, M., Rezaizadeh, A., Delahaza, A., Santos, C. G., Moore, M., Graybeal, B. & Washer, G. 2003. “A comparison of nondestructive evaluation methods for bridge deck assessment.” *NDT & E International*, 36: 245-255.

Scullion, T., Saarenketo, T. 1995. “Ground penetrating radar technique in monitoring defects in roads and highways.” In *Proc. Symp. Appl. Geophys. to Eng. and Env. Prob., SAGEEP*, Orlando, Florida: 63-72.

Shi, L. & Shao, Z. 2009. “Ultrasonic damage detection of concrete structures by using pulse-echo sensor arrays and SAFT.” Proc. of SPIE Vol, 2009. 749312-1, Weihai, China, July 8.

Shokouhi, P. & Wiggenhauser, H. 2012. “Multiprobe Ultrasonic Testing for Detection of Delamination in Concrete Bridge Decks.” Transportation Research Board 91st Annual Meeting, Washington, D.C., Jan. 22-26.

Smith, K. 2005. “Maturity Testing for Concrete Pavement Applications.” *Concrete Pavement Technology Program TechBrief.* FHWA-IF-06-004. Federal Highway Administration, Washington D.C.

Sokolov, I. V. 2003. “The split-method of ultrasonic nondestructive testing.” *Nondestructive Testing and Evaluation,* 19: 1-13.

Song, P. 2010. *Ultrasound Transient Shear Wave Elasticity Imaging for Tendon Tissue*. (Thesis dissertation, University of Nebraska).

Spies, M., Rieder, H., Orth, T. and Maack, S. 2012. “Simulation of ultrasonic arrays for industrial and civil engineering applications including validation.” In *Review of Progress in Quantitative Nondestructive Evaluation: Volume 31,* 1430: 841-848.

Stokoe, K.H., Wright, S.G., Bay, J.A. and Roesset, J.M. 1994. “Characterization of geotechnical sites by SASW method.” Woods, R. D., Ed., *Geophysical characterization of sites*: Oxford Publishers.

Van Dam, T. 2005. “Guidelines for early-opening-to-traffic Portland cement concrete for pavement rehabilitation.” *NCHRP Rep. No. 540,* Transportation Research Board, Washington, DC.

Vladišauskas, A., Mažeika, L., Sliteris, R., Raišutis, R. & Jankauskas, A. 2011. “Pulse and frequency responses of broadband low frequency ultrasonic transducers.” *Ultragarsas (Ultrasound),* 66: 32-39.

Vladišauskas, A., Raišutis, R., Šliteris, R., Seniūnas, G. & Jankauskas, A. 2010. “Investigation of the characteristics of the low frequency broadband contact transducers.” *Ultragarsas (Ultrasound),* 65: 41-44.

Vonramm, O. T. & Thurstone, F. L. 1976. “Cardiac imaging using a phased array ultrasound system.” I. System design. *Circulation,* 53: 258.

Voigt, Th., Ch. U. Grosse, Z. Sun, S. P. Shah, and H. -W. Reinhardt. 2005. "Comparison of Ultrasonic Wave Transmission and Reflection Measurements with P- and S-waves on Early Age Mortar and Concrete." *Materials and Structures*, 38.8: 729-38.

Voigt, T., Shah, P. 2003. “Nondestructive monitoring of setting and hardening of portland cement mortar with sonic methods.” *Proceedings of the Sixth International Symposium on Non-Destructive Testing in Civil Engineering (NDT-CE 2003)*, Berlin, Germany.

Voigt, T., Sun, Z., Shah, S. 2006. "Comparison of Ultrasonic Wave Reflection Method and Maturity Method in Evaluating Early-age Compressive Strength of Mortar." *Cement and Concrete Composites*, 28(4): 307-16.

Voigt, T., SUN, Z., SHAH, S. 2006. “Health Monitoring of Early Age Concrete.” Northwestern University, Illinois.

Voigt, T., Ye, G., Sun, Z., Shah, S., and Vanbreugel, K. 2005. "Early Age Microstructure of Portland Cement Mortar Investigated by Ultrasonic Shear Waves and Numerical Simulation." *Cement and Concrete Research*, 35(5): 858-66.

Voigt, T., Akkaya, Y., and Shah, S. 2003. "Determination of Early Age Mortar and Concrete Strength by Ultrasonic Wave Reflections." *Journal of Materials in Civil Engineering.* 15(3): 247.

Wilde, W. J. 2013. Development of a Concrete Maturity Test Protocol. Rep. no. MN/RC 2013-10. Minnesota Department of Transportation, St. Paul, MN.

Zhu, J. and Popovics, J. 2002. “Non-contact detection of surface waves in concrete using an air-coupled sensor.” *Quantitative Nondestructive Evaluation* 615(1): 1261-1268.

Zhu, J. & Popovics, J. S. 2007. “Imaging concrete structures using air-coupled impact-echo.” *Journal of Engineering Mechanics*, 133: 628-640.

Zhu, J., Popovics, J. S. & Schubert, F. 2004. “Leaky Rayleigh and Scholte waves at the fluid–solid interface subjected to transient point loading.” *The Journal of the Acoustical Society of America*, 116: 2101.

Appendix A

Development of Improved Velocity Calibration Technique

Figure A1 shows the results of 5 sending and receiving transducer pairs from an example measurement with MIRA on a typical concrete pavement. Although the position of each of the transducer pairs is slightly different, they are all spaced at 200 mm apart. It can be observed that although the amplitude of each signal can be variable, each pulse arrival shape and arrival time is repeatable. This illustrates the capability of using this system arrangement and direct arrivals of each transmitted shear wave near the surface to calculate the shear wave velocity.

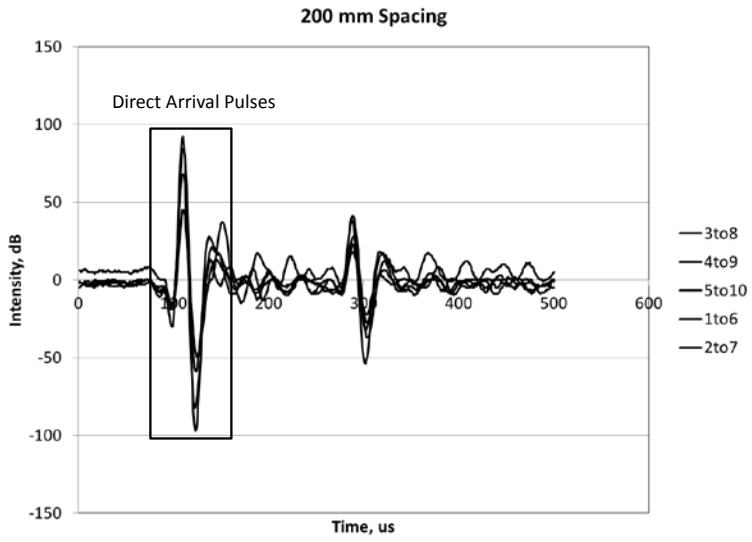

Figure A1. Example direct arrival pulses for five 200 mm spaced transducer channel pairs.

To illustrate the method used in this study to account for the system uncertainty, consider a case of 3 transducer pairs. In this method, the distance between the adjacent receiving transducer and the next receiving transducer of interest, $dx'_{n,N} = x'_N - x'_n$, is considered for the velocity calculation. The effective time of flight, $t_{e,r}^{feff}$, between transducers located at x'_N and x'_n is the difference in arrival times $dt'_{n,N} = t'_N - t'_n$. Figure A2 shows the corresponding raw data time history received by both locations from the emitted transducer location.

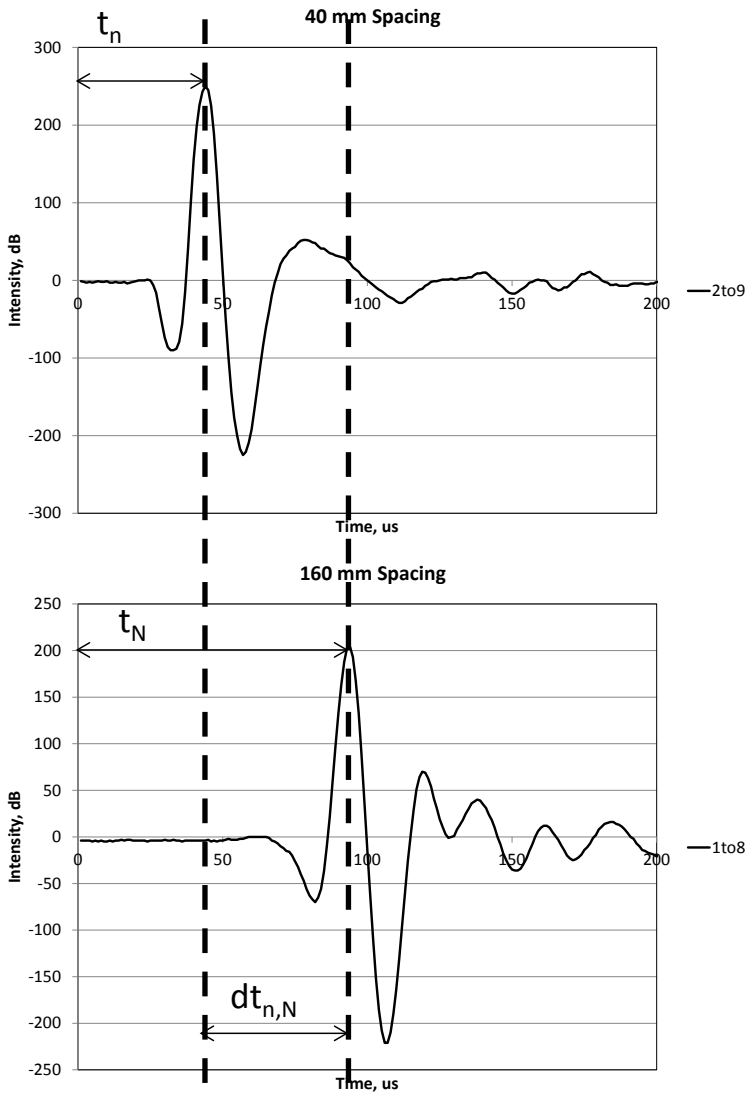

Figure A2. Plots showing effective time of flight calculation.

The velocity for the setup in this study can be calculated using equation 1 for a set of 3 transducers. Using multiple sets of 3 transducers and averaging the results increases the stability of the velocity calculations. Assuming there are a total of T transducer combinations, the calculated velocity is defined by equation 2:

$$C_S^{Avg} = \sum_{j=1}^{T} \frac{C_{S,j}^{dir}}{T} \quad [1]$$

where j is the current combination of transducers.

The impulse time history should be corrected so that high intensity impulse locations correspond to the arrival of the impulse in the time of flight analysis. Due to the same un-differentiable factors listed above dealing with velocity calculation, determination of the shift factor, t^{SHIFT}, should be accomplished by taking advantage of the redundancy of the ultrasonic linear array measurements. The shift factor is determined using known spacing and associated impulse direct arrivals using the relationship given in equation 2:

$$t^{SHIFT} = \frac{1}{ER}\sum_{e=1}^{T-SP^{min}}\sum_{r=SP^{min}}^{T} t_{e,r}^{Max} - \frac{x'_{e,r}}{C_S^{Avg}} \qquad [2]$$

where $t_{e,r}^{Max}$ is the time associated with the maximum amplitude of the direct arrival and SP^{min} is the minimum spacing between transducers that allows for accurate detection of the peak, dependent on the sampling rate of the receiving transducer. Figure A3 shows an example transducer pair impulse response from the ultrasonic linear array system showing how to obtain $t_{e,r}^{Max}$.

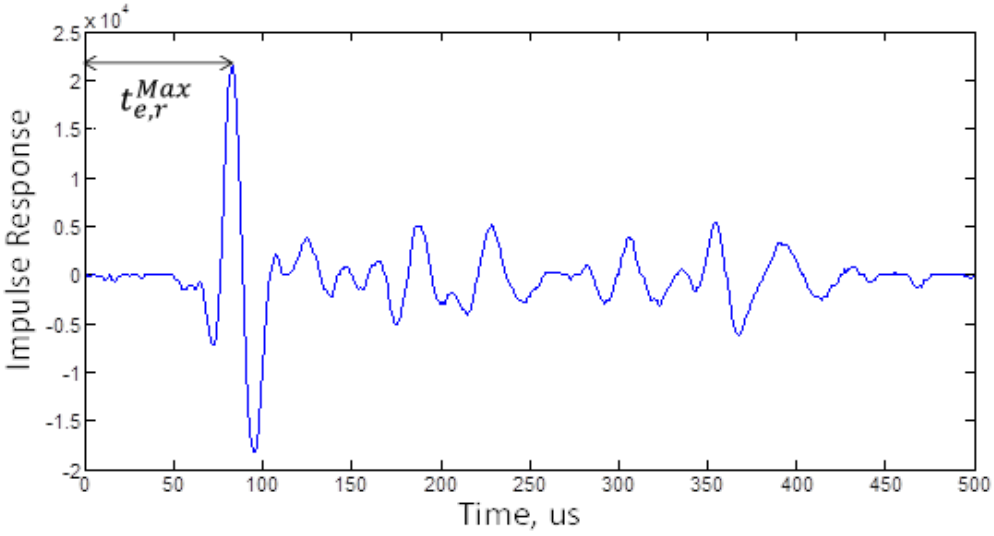

Figure A3. Determination of the time associated with the direct arrival.

For the ultrasonic linear array formulation, the impulse response time-histories are corrected by setting $t = t - t^{SHIFT}$ for each sending and receiving pair before it is applied to the reconstruction image.